UNIVERSITY OF ROCHESTER
LABORATORY FOR LASER ENERGETICS

Volume 153
October–December 2017
DOE/NA/1944-1370

LLE Review

Quarterly Report

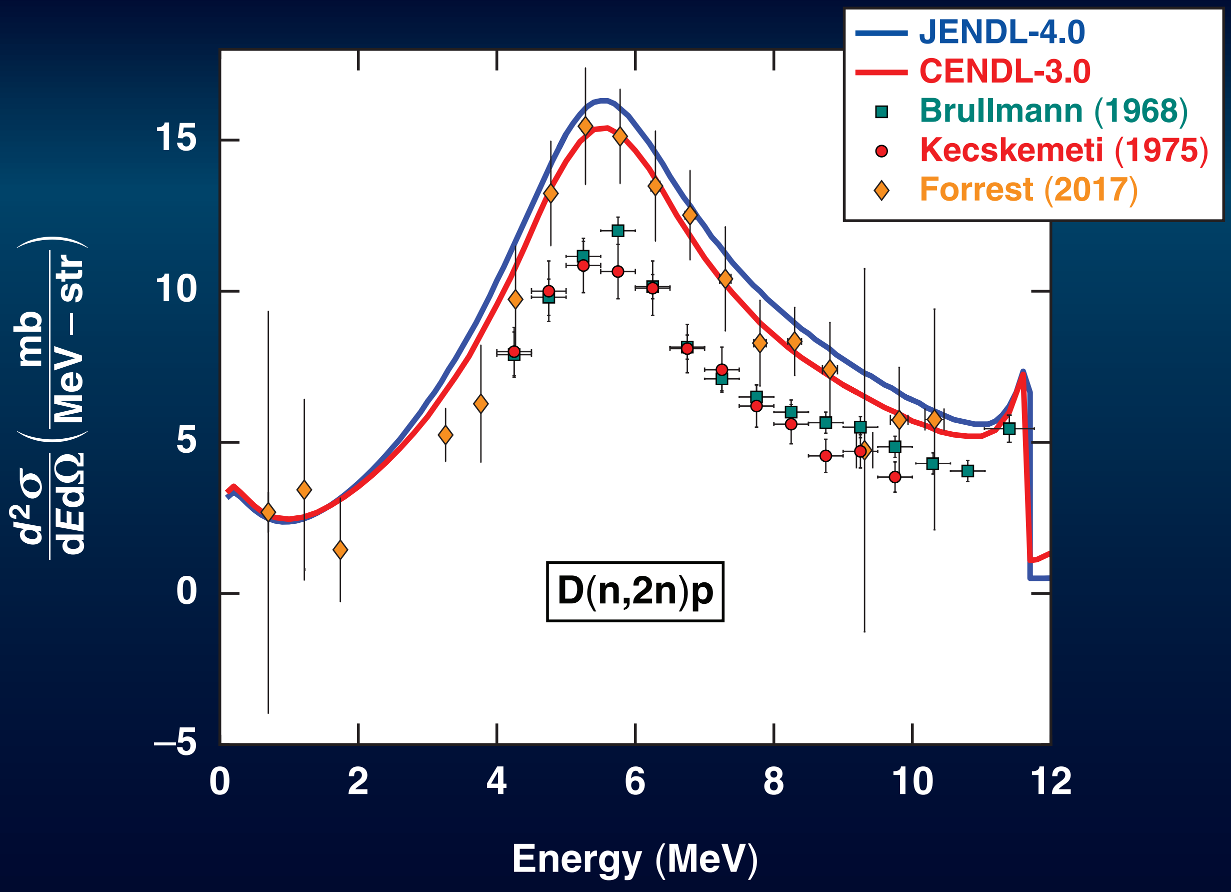

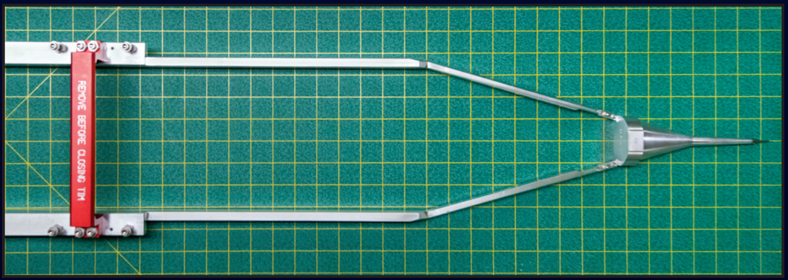

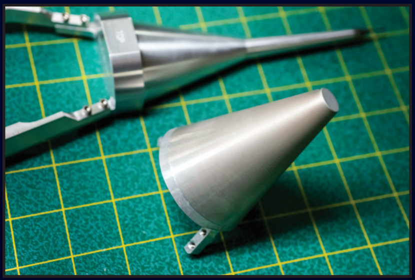

About the Cover:

The neutron-induced breakup cross sections of deuterium show two recent theoretical models (JENDL-4.0 and CENDL-3.0) and the results from past experiments. The most recent experiment used, for the first time, a laser-based facility (OMEGA) to generate a bright neutron source to induce the breakup of deuterium in nuclear reaction vessels positioned near the target chamber center. This new experimental configuration measured a larger energy spectrum—from 0.5 to 10 MeV—as compared to previous methods performed on accelerator-based platforms. The measured energy spectrum of neutrons produced from the breakup of deuterium is inconsistent with a two-nucleon-force model. The experimental data are more accurately described by the predictions of a recently developed theoretical framework that assumes the presence of a three-nucleon force used in modern theoretical models. A noticeable peak at 11.8 MeV, which has not been confirmed experimentally, represents the final-state interaction and is required to further develop an accurate description of the three-nucleon-force model. The bracket shown in the inset was designed with minimal mass in order to avoid additional neutron scattering along the detector's line of sight once it is positioned at target chamber center.

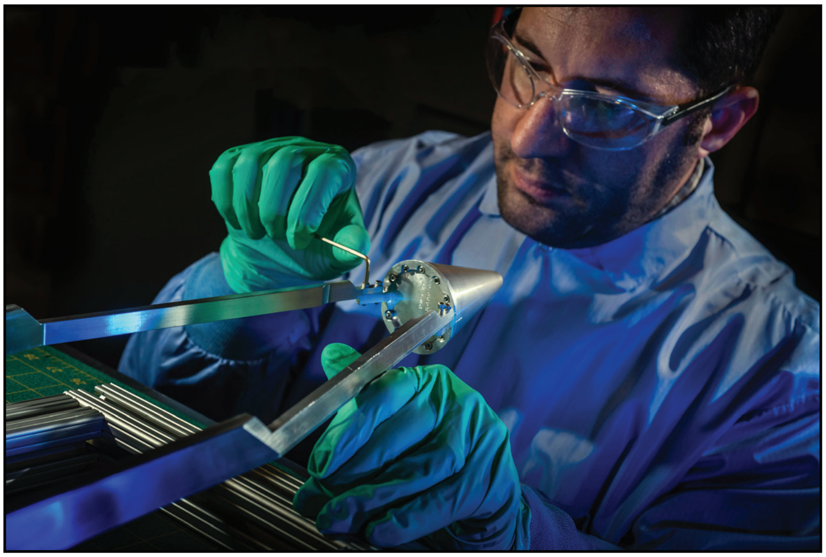

The photo on the right shows C. J. Forrest assembling a nuclear reaction vessel that is attached to a specially designed bracket mounted in one of the ten-inch manipulator diagnostic ports on the target chamber.

The work described in this volume includes current research at the Laboratory for Laser Energetics, which is supported by New York State Energy Research and Development Authority, the University of Rochester, the U.S. Department of Energy Office of Inertial Confinement Fusion under Cooperative Agreement No. DE-NA0001944, and other agencies.

For questions or comments, contact Sid Sampat, Editor, Laboratory for Laser Energetics, 250 East River Road, Rochester, NY 14623-1299, (585) 275-2596.

Worldwide-Web Home Page: http://www.lle.rochester.edu/

Printed in the United States of America
Available from
National Technical Information Services
U.S. Department of Commerce
5285 Port Royal Road
Springfield, VA 22161
www.ntis.gov

UNIVERSITY OF ROCHESTER
LABORATORY FOR LASER ENERGETICS

Volume 153
October–December 2017
DOE/NA/1944-1370

LLE Review

Quarterly Report

Contents

In Brief

This volume of the LLE Review, covering October–December 2017, features "Nuclear Science Experiments with a Bright Neutron Source from Fusion Reactions on the OMEGA Laser System," by C. J. Forrest, J. P. Knauer, V. Yu. Glebov, P. B. Radha, S. P. Regan, T. C. Sangster, M. Sickles, C. Stoeckl, and J. Szczepanski (LLE), and W. U. Schröder (Depts. of Chemistry and Physics, University of Rochester). This article (p. 1) uses yields and energy spectra of neutrons from D(n,2n)p to study the breakup reaction measured at a forward angle of $\theta_{\text{lab}} = 3.5° \pm 3.5°$ using a sensitive, high-dynamic-range neutron time-of-flight spectrometer to infer the double-differential breakup cross section $d^2\sigma/\text{d}E\text{d}\Omega$ for 14-MeV D–T fusion neutrons.

Additional research highlights presented in the issue include the following:

- I. A. Begishev, J. Bromage, and J. D. Zuegel (LLE), and S. T. Yang, P. S. Datte, and S. Patankar (LLNL) demonstrate the fifth-harmonic generation of a pulsed Nd:YLF laser in a cascade of nonlinear crystals with a record efficiency of 30% (p. 12). Cesium lithium borate is used in a Type-I configuration for sum-frequency mixing of 1053 nm and 266 nm, producing 211-nm pulses. Flattopped beam profiles and pulse shapes optimize efficiency. Energies up to 335 mJ in 2.4-ns pulses were demonstrated.

- S. T. Ivancic, P. Franke, C. Mileham, R. Boni, J. Katz, C. R. Stillman, P. M. Nilson, and D. H. Froula have designed an ultrafast x-ray streak camera for time-resolved studies of high-energy-density experiments (p. 17). The streak camera's electro-optical imaging system features a polarity-reversible quadrupole doublet, allowing two imaging modes depending on the scientific mission need. The streak camera's temporal impulse, detector efficiency, and linear dynamic range were qualified using a synchronized subpicosecond, 263-nm probe laser incident upon a gold photocathode. Dynamic testing shows a <2-ps impulse response in the fastest operating mode and a measured 400:1 dynamic range per resolution element in the high-dynamic-range mode.

- D. Turnbull, A. Colaitis, R. K. Follett, J. P. Palastro, and D. H. Froula present recent results on cross-beam energy transfer (p. 24). Wavelength tuning was used to vary the amount of energy transfer between two beams in a quasi-stationary plasma with carefully controlled conditions. The amount of transfer agreed well with calculations assuming linear ion-acoustic waves with amplitudes up to $\delta n/n \approx 0.015$. Increasing the initial probe intensity to access larger ion-acoustic wave amplitudes for otherwise fixed conditions yields evidence of saturation beyond this level. The ability to manipulate a beam's polarization, which results from the anisotropic nature of the interaction, is revisited; an example is provided to demonstrate how polarization effects in a multibeam situation can dramatically enhance the expected amount of energy transfer.

- R. K. Follett, J. G. Shaw, J. F. Myatt, J. P. Palastro, R. W. Short, and D. H. Froula show that laser frequency detuning can potentially be used to suppress the two-plasmon–decay (TPD) instability using 3-D laser–plasma interaction simulations (p. 35). For the plasma conditions and laser configuration in a direct-drive inertial confinement fusion implosion on the OMEGA laser, the simulations show that ~0.5% laser frequency detuning is sufficient to eliminate TPD-driven hot-electron generation in current experiments. This may allow for higher laser intensities in future implosion designs.

- M. D. Sharpe, C. Fagan, and W. T. Shmayda (LLE), and W. U. Schröder (Depts. of Chemistry and Physics, University of Rochester) explore the distribution of tritium between the near surface and the bulk in 316 stainless steel using two independent techniques: pulsed-plasma exposures and a zinc-chloride wash (p. 41). It was discovered that 17% to 20% of the total inventory absorbed into a stainless-steel sample after a 24-h exposure to DT gas at room temperature resides in the water layers present on the metal surface. Redistribution of tritium between the surface and the bulk of stainless steel, if it occurs, is very slow. Tritium does not appear to enter into the bulk at a rate defined by lattice diffusivity.

- J. L. Shaw and D. H. Froula (LLE); N. Lemos (UCLA and LLNL); and K. A. Marsh and C. Joshi (LLNL) present experimental data and simulation results of a study of direct laser acceleration (DLA) of electrons in a laser wakefield accelerator (LWFA) operating in the forced or quasi-blowout regimes (p. 46). When a significant overlap exists between the trapped electrons and the drive laser in a LWFA cavity, the resulting electrons can gain energy from both the LWFA and DLA mechanisms. Experimental work investigates the properties of the electron beams produced in a LWFA with ionization injection by dispersing those beams in the direction perpendicular to the laser polarization. These electron beams show certain spectral features that are characteristic of DLA. These characteristic spectral features are reproduced in particle-in-cell simulations, where particle tracking is used to elucidate the roles of LWFA and DLA to the energy gain of the electrons in this experimental regime and to demonstrate that such spectral features are definitive signatures of the presence of DLA in LWFA.

Sid Sampat
Editor

Nuclear Science Experiments with a Bright Neutron Source from Fusion Reactions on the OMEGA Laser System

Introduction

Inertial confinement fusion (ICF) experiments are designed to study the hydrodynamic nature of high-energy-density plasmas to achieve ignition and gain in laboratory experiments.[1] In direct-drive ICF experiments on LLE's OMEGA Laser System,[2] neutrons are produced using a laser to implode microballoons filled with deuterium–tritium (DT) fuel.[3] The dominant fusion reaction in these implosions is

$$\mathrm{D} + \mathrm{T} \rightarrow {}^{4}\mathrm{He}(3.52\ \mathrm{MeV}) + \mathrm{n}(14.03\ \mathrm{MeV}). \tag{1}$$

Two additional primary fusion reactions, D + D and T + T (Ref. 4), make a much smaller contribution ($\sim 10^{-2}$) compared to the overall yield and have a negligible impact on the experimental measurements presented in this article. One particular class of implosions—"exploding pushers"[5]—uses thin glass shells that can produce neutron yields in excess of 1×10^{14} with pulse durations of the order of $\approx$1 ns and energy on target of ~30 kJ (Ref. 6).

To test a modern microscopic nuclear theory, an experiment to measure the neutron-induced breakup of light nuclei has been developed. This platform could prove to be a valuable tool for nuclear physicists since experimental data are scarce and incomplete; in particular, for energy spectra of neutrons from D(n,2n)p breakup occurring in a thermonuclear ICF environment. The present quality of the measured breakup energy spectrum from deuterium does not permit a clear conclusion with respect to recent theoretical models that have been proposed.[7] For this reason, the breakup of deuterons is a good candidate to demonstrate the capability of this experimental platform.

The reaction being studied in this experiment is expressed as

$$\mathrm{n}(14\ \mathrm{MeV}) + \mathrm{D} \rightarrow 2\mathrm{n}(0 - 11.8\ \mathrm{MeV}) + \mathrm{p}(0 - 11.8\ \mathrm{MeV}). \tag{2}$$

Here the energy ranges of the reaction products are given in parentheses.[8]

An experimental setup was developed on the OMEGA Laser System to use these monoenergetic neutron sources to investigate the breakup of light nuclei. The experimental platform consists of a subnanosecond, high-yield 14-MeV neutron pulse incident on a reaction vessel filled with the target compound. A reaction vessel filled with deuterated compounds is located as close as possible to the implosion, maximizing the solid angle without interfering with the laser pulses required for illuminating the microballoon.

The spectra from primary fusion reactions and the breakup of the light nuclei are recorded with a high-dynamic-range, high-resolution neutron time-of-flight (nTOF) spectrometer. This diagnostic is located in a highly collimated line of sight and filled with a low-afterglow liquid scintillator contained inside a thin steel housing positioned in-line with the reaction vessel.[9] It was designed to have a dynamic range of up to 10^6 with the capability to measure the neutron energy spectrum over an energy range of 0.5 MeV to 15 MeV. A schematic of the experimental setup is shown in Fig. 153.1.

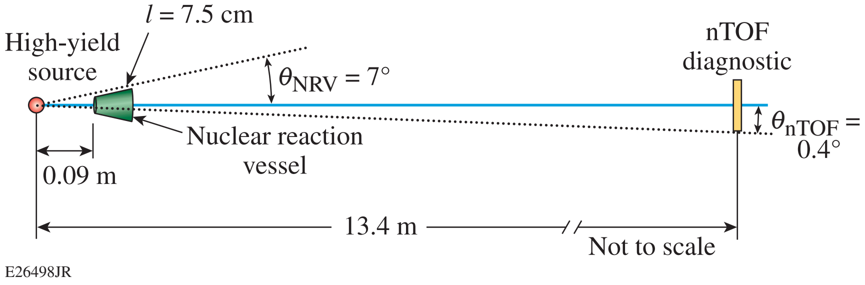

Figure 153.1
The experimental setup consists of a high-yield neutron source incident on a nuclear reaction vessel (NRV). The vessel contains either non-deuterated or deuterated compounds necessary for direct comparison with the neutron-induced breakup reaction. The neutron signal is measured using a high-dynamic-range, high-resolution time-of-flight diagnostic positioned 13.4 m from the target chamber center. Signals are sent to a diagnostic rack and digitized for analysis. nTOF: neutron time of flight.

This article presents for the first time an experimental setup for which a laser-based facility has been used to measure the neutron-induced breakup reactions of light nuclei. The following sections (1) provide details about the experimental setup and configuration to induce the breakup reactions along with the diagnostic used to measure the nTOF spectra; (2) present details on the calibration of the diagnostic, essential for calculating the neutron energy spectrum from the breakup yield; (3) discuss the experimental data along with the uncertainty in the measurements; and (4) summarize our findings and discuss future experiments.

Experimental Setup and Configuration

1. High-Yield Neutron Source

The bright neutron source (14 MeV) generated for this experiment uses an exploding-pusher design with a thin-walled (~3-μm), ~1-mm-diam SiO_2 microballoon filled with 10 atm of equimolar DT fuel.[10,11] The laser beams deliver up to 30 kJ of energy onto the target with a nominal 1-ns square pulse. The symmetric illumination with the 60 UV laser beams rapidly heats the thin shell, expands, and drives a shock wave into the fuel.[12] This shock wave compresses and heats the fuel as it converges at the center of the target. As the shock rebounds, the fuel reaches sufficient temperatures to produce thermonuclear fusion reactions, with neutron yields of up to 1×10^{14} emitted in 4π. In this implosion design, the bang time (time when peak neutron production takes place) is ~1 ns after the laser is incident on the target with a neutron-production width of ~100 ps (Ref. 13). The neutron-emitting region (hot spot) for this class of implosions is ~100 μm in diameter. An example of the laser pulse along with the neutron temporal emission history is shown in Fig. 153.2.

2. Nuclear Reaction Vessel

The nuclear reaction vessel (NRV) in constructed from thin (1-mm) aluminum to minimize additional neutron scattering. Figure 153.3(a) shows a photograph of the reaction vessel attached to the support bracket; Fig. 153.3(b) shows a close-up of the vessel. A pointer was designed to mount in place of the reaction vessel to allow one to align the system. The overall length of the truncated cone-shaped vessel is 7.5 cm with the smallest diameter being 0.9 cm and the largest diameter being 4 cm. The vessel was specially designed to be positioned 9 cm from the center of the OMEGA target chamber to ensure that the incoming laser beams have a clear path to illuminate the microballoon. The vessels are attached to a specially designed bracket mounted in one of the ten-inch manipulator (TIM) diagnostic ports on the target chamber. As with the vessel requirements, the bracket was designed with minimal mass in order to avoid additional neutron scattering along the detector's line of sight. Because of the geometry of the vessel with respect

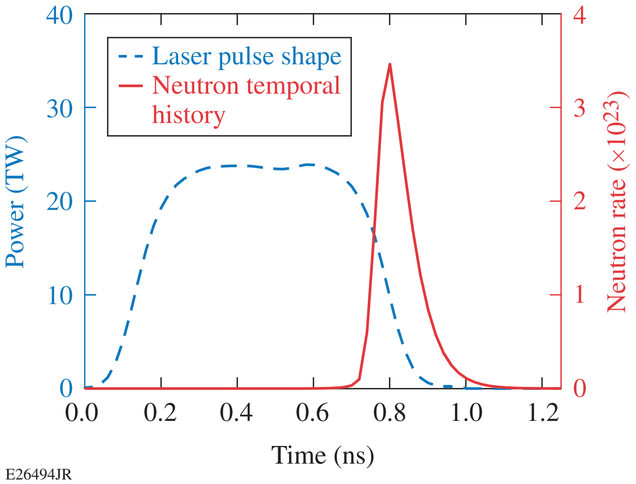

E26494JR

Figure 153.2
A plot showing the nominal 1-ns square laser pulse and neutron production rate from a typical exploding pusher on OMEGA. Peak neutron production (bang time) takes place ~800 ps from the moment light is incident on the target. The burnwidth for this class of implosions is of the order of a 100-ps full width at half maximum (FWHM).

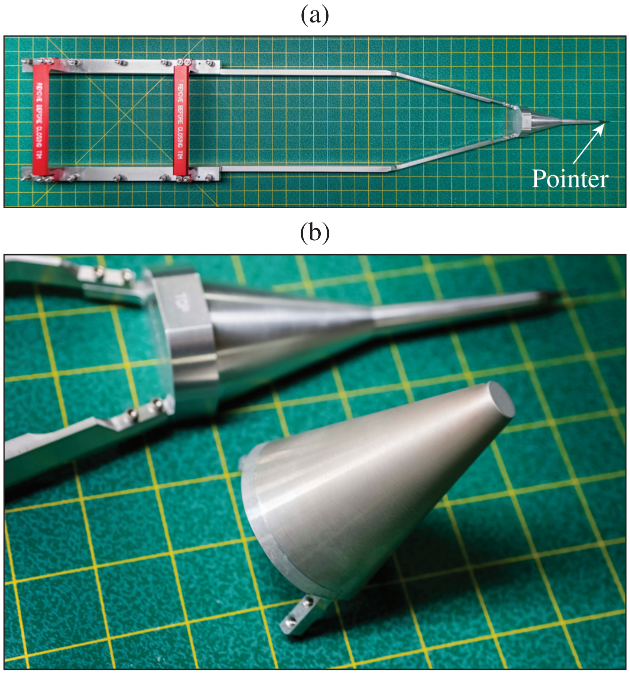

E26495JR

Figure 153.3
(a) A support frame designed to be mounted in one of the diagnostic ports on the OMEGA target chamber. (b) The nuclear reaction vessel is constructed from thin aluminum to minimize additional neutron scattering. The face of the vessel is positioned 9 cm from the high-yield neutron source.

to the diagnostic, this measurement will cover an angle normal to the vessel of $\theta_{\text{lab}} = 3.5° \pm 3.5°$.

3. Highly Collimated Line of Sight

High-yield DT implosions on OMEGA generate an unwanted background signal from neutron scattering in the target chamber walls and surrounding concrete structures inside the Target Bay, such as the OMEGA end-mirror structures. For this reason, the primary diagnostic is positioned in a shielded, highly collimated line of sight to increase the signal-to-background ratio of the measurements.[14] The detector is mounted in a low-scattering environment underneath the Target Bay floor, 13.4 m from the target chamber center (TCC). A 21-cm-diam hole in the 60-cm-thick concrete floor acts as a collimator close to the time-of-flight diagnostic. A mid-beam collimator was designed to be the defining aperture of the neutron beam to reduce the detector's field of view from the target chamber. The mid-beam collimator has a 60-cm^2 cross section and is ~70 cm in length. It is constructed from high-density polyethylene (~0.95 g/cm^3) and mounted on a semi-permanent stand located inside the OMEGA Target Bay and positioned approximately halfway between TCC and a concrete barrier as shown in Fig. 153.4.

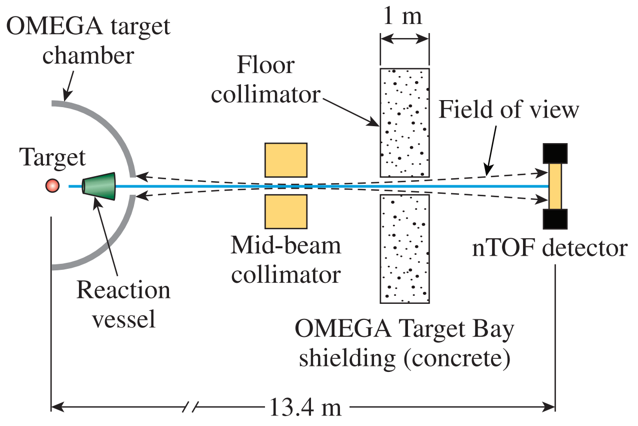

Figure 153.4
The 13.4-m nTOF is positioned in a clear line of sight through the TIM-6 diagnostic port (not shown). A thick concrete floor acts as collimator to shield the diagnostic from unwanted neutron scattering off the surrounding structure in the Target Bay. A mid-beam collimator is mounted between the target chamber and the diagnostic. TIM: ten-inch manipulator.

4. Liquid-Scintillator Detector

The diagnostic used to measure the neutron energy spectrum in this study is a four-microchannel-plate photomultiplier tube (MCP-PMT) detector design positioned 13.4 m from TCC.[15] It consists of a 20-cm-diam, 10-cm-deep stainless-steel cylindrical housing that contains the scintillation fluid. This detector uses a thin-walled (2-mm) construction to minimize neutron scattering within the scintillator housing. Thin (<0.3-cm) stainless-steel end plates are used to seal the cylindrical housing to minimize neutron attenuation. The ports for the MCP-PMT are 40-mm-diam fused-silica windows mounted on the cylindrical housing and sealed with Viton O rings. This diagnostic uses oxygenated xylene doped with *diphenyloxazole* $C_{15}H_{11}NO$ + *p*-bis-(o-methylstyryl)-benzene (PPO + bis-MSB) wavelength-shifting dyes, which generates light emission in the visible to near-ultraviolet wavelength range (i.e., from 380 μm to 420 μm). This oxygenated liquid scintillator has a fast time response with a low-light afterglow.[16] A computer-aided drawing of the nTOF diagnostic with the MCP-PMT's is shown in Fig. 153.5.

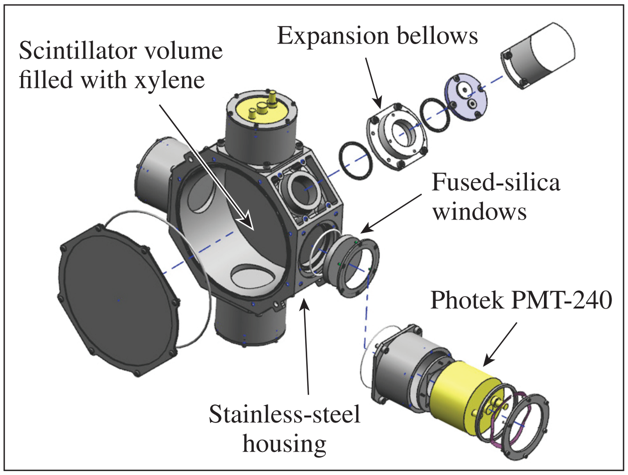

Figure 153.5
A CAD drawing of the nTOF detector shows a cavity for the scintillation fluid, the fused-silica windows, and the photomultiplier-tube (PMT) mounts. The detector is mounted in a shielded environment behind a concrete barrier to minimize unwanted neutron scattering.

5. Gated Microchannel-Plate Detectors

The light emitted by the scintillator process is viewed through fused-silica windows, where it is coupled to four Photek 40-mm-diam MCP-PMT's.[17] These PMT's are designed to operate in current mode in order to measure the significant photon flux generated from up to 1×10^7 incident neutrons interacting in the scintillation volume. Each of the four PMT's is operated at a different high voltage that corresponds to the desired gain (see Table 153.I) required for measuring the nTOF signal and to achieve a dynamic range in yield of up to 10^6. To ensure that measurements are not compromised because of charge depletion of the MCP, off-line tests were performed

Table 153.I: Nominal MCP-PMT high-voltage and gate-timing setup for the 13.4-m neutron time-of-flight diagnostic.

PMT assignment	MCP-PMT	High voltage (V)	Gain	Gate timing (ns)
A	Photek-140	3875	10	N/A
B	Photek-240	4500	10,000	1090
C	Photek-140	4150	200	730
D	Photek-240	4350	400	815

MCP: microchannel plate; PMT: photomultiplier tube.

on each of the MCP-PMT's at the specified gain to confirm that signal linearity is preserved. Fast-gating units allow the MCP-PMT unit to turn off and on with a recovery time of ~30 ns. The gate-timing windows are predetermined to record a particular region of interest in the time-of-flight spectrum, excluding the PMT-A, which remains ungated to measure the primary DT peak. The gate-timing signals are generated using an SRS DG-635 digital pulse generator[18] that is timed from the OMEGA Hardware Timing System (HTS).

6. Signal Transport and Data Acquisition

The analog signals from the MCP-PMT's are transmitted to the oscilloscope using ~5-m-long LMR-600 cables.[19] Three of the MCP-PMT's signals are sent to eight-bit, 1-GHz Tektronix DPO 7104 digital oscilloscopes, while the fourth MCP-PMT signal is sent to a 12-bit, 250-MHz LeCroy HDO6104-MS digital oscilloscope.[20,21] The signal from each PMT is spilt into separate oscilloscope channels using three-way 1-GHz splitters.[22] The fourth channel on each of the oscilloscopes is reserved for the OMEGA timing fiducial, which is used for absolute timing of the system. For consistency, these cables were checked by analyzing the frequency-dependent loss using an Agilent Microwave Analyzer to measure the attenuation as a function of the frequency and compared to the results in the manufacturer's published specifications.[23] These tests confirmed that there is negligible attenuation in the measured signal output with the use of short cables and input signals in the frequency range <1000 MHz.

7. Beamline Attenuation

The beamline attenuation as a function of neutron energy has been modeled using a neutron transport code (MCNP) to obtain the fraction of the neutrons that are incident on the detector relative to the source originating at TCC in different configurations. The baseline configuration includes the point neutron source and the neutron detector excluding air and the surrounding structure. A second simulation introduced air to illustrate the amount of attenuation of the neutrons as they travel toward the detector. The final simulation includes all the large-scale structures such as the target chamber (aluminum) and concrete shielding. Additional sources that could contribute to unwanted scattering in the specified line of sight include the TIM with a 1.9-mm stainless-steel vacuum window that separates the vacuum from the air, the mid-beam collimator, and the air gap (7.5 m) between the end of the TIM and the detector. The resulting beamline attenuation from the separate simulations in this line of sight is shown in Fig. 153.6 (Ref. 24). The neutron attenuation can be as high as 20% with energies below 2 MeV. It should be noted that neutron attenuation is included in the MCNP simulation, which modeled the energy spectrum of neutrons emitted from the physics target (see **D–D Yield Calibration**, below). Uncertainties in the beamline attenuation are governed by the accuracy of the experimentally measured cross sections for the material used in these simulations.[25] Detailed geometry of the model is also required to further reduce the uncertainty of the simulations and was referenced from computer-aided drawings for accuracy and completeness.

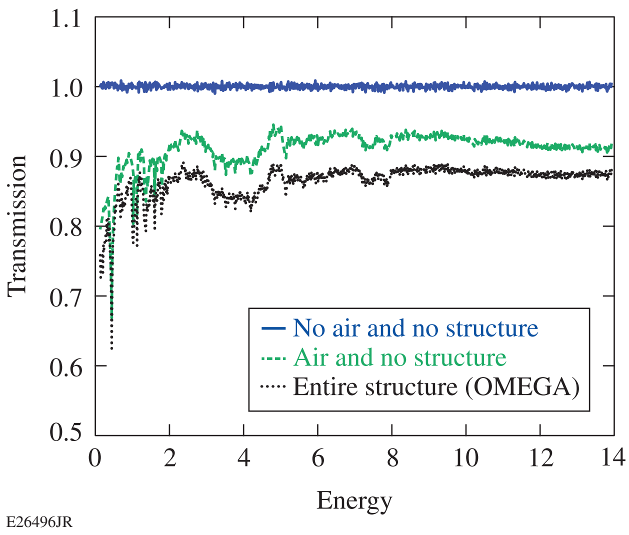

Figure 153.6
Three different simulations were performed to illustrate the attenuation in the 13.4-m beamline. The first configuration is without any air or structure in the target environment. Adding air in the line of sight emphasizes the loss of neutrons below 2 MeV in addition to the absorption regions from 2 to 4 MeV. The remaining structure in the beamline includes the stainless-steel plate that reduces the signal approximately uniformly over 1 to 14 MeV.

Detector Calibration

1. D–D Yield Calibration

The 13.4-m nTOF detector is typically calibrated using two D_2-filled target shots with different implosion parameters, producing yields that differ by a factor of ~10. The signals from the photomultiplier tubes are measured on the oscilloscope as time-dependent currents $I(t_n)$, which can be expressed in terms of $H(t_n)$ as

$$I(t_n) = \frac{dC(t_n)}{dt_n} = \frac{1}{k_1}\frac{dH(t_n)}{dt_n}, \tag{3}$$

where $H(t_n)$ is the scintillator light output measured in MeVee (electron equivalent), C is the charge in coulombs, and k_1 = MeVee/pC is a constant. The nonlinear relation between the light output for a single neutron absorbed H_n and the neutron energy E_n can be approximated by the power law

$$H_n(t_n) = k_2 * E_n^{\alpha}(t_n), \tag{4}$$

where α is the power law coefficient, k_2 is in units of MeVee/MeV$^{\alpha}$, and E_n is the energy of the neutron as a function of arrival time t_n to the diagnostic.[26] In the literature, measurements of the proton light response for xylene-based solvents scale as $\alpha \sim 0.3$ (Refs. 27–29). Total light output as a function of time for all neutrons that deposit energy in the scintillator can be expressed by the following relation:

$$\frac{dH(t_n)}{dt_n} = k_2 E^{\alpha}\chi_n(E_n)\frac{dY(t_n)}{dE_n}\frac{dE_n}{dt_n}, \tag{5}$$

where $\chi_n(E_n)$ is defined as the fraction of neutron kinetic energy deposited in the scintillator. The relation between the measured photomultiplier current $I(t_n)$ and the scintillator light output $dH(t_n)/dt_n$ is used to infer the neutron yield Y_n measured for the time-of-flight interval (t_n, $t_n + dt_n$) using Eq. (3):

$$dY_n(t_n) = \frac{k_1}{k_2}\frac{1}{\chi_n(E_n)E_n^{\alpha}} I(t_n)dt_n. \tag{6}$$

For a monoenergetic reaction, in the case of a D–D fusion product, Eq. (6) can be solved approximately as

$$dY_n(t_n) = \frac{k_1}{k_2}\left[\frac{1}{\chi_{D_2}E_{D_2}^{\alpha}}\right]\Bigg|_{E_{D_2}} I(t_n)dt_n, \tag{7}$$

where $1/\chi_{D_2}E_{D_2}^{\alpha}$ is a constant that allows for integration over the D_2 peak neutron distribution in time. The charge measured by each of the PMT's at the detector positioned at 13.4 m is cross-calibrated against the standard D–D neutron yield measurements on OMEGA to obtain a calibration constant k_1/k_2 for monoenergetic neutrons defined by

$$\frac{k_1}{k_2} = \frac{Y_{D_2}\chi_{D_2}E_{D_2}^{\alpha}}{I_{D_2}} \tag{8}$$

with units of MeV$^{\alpha}$/pC. The constant k_1/k_2 is required to infer the yield over all energies. It is important to note that two factors will change k_1/k_2: (1) scintillator degradation that changes the light output as a function of neutron energy and (2) the gain of the MCP-PMT, which is a nonlinear function of the high voltage.[30] The energy deposition $\chi_n(E_n)$ is calculated using MCNP to model the fraction of neutron kinetic energy deposited in the scintillator. The model consists of a 20-cm-diam, 10-cm-thick volume of liquid xylene (C_8H_{10}), with monoenergetic neutrons ranging from 0.5 to 14 MeV incident on the volume. The energy deposition in the scintillator is tallied in the simulation code. It is assumed that the neutrons in these simulations arrived at the detector at time (t) and with an energy $E_n(t_n)$ that depends on their time of flight. This is a good approximation since the probability of an outgoing neutron, with a given energy, undergoing multiple scattering interactions from surrounding support structures and still arriving at the detector is negligible.

2. Signal Timing

To relate the time-of-flight spectrum to an absolute energy spectrum, the oscilloscope is timed using semiannual dedicated shot time on OMEGA, producing ultrashort x rays (<20 ps) that are measured by the detector system and correlated to the fiducial for absolute timing. The fiducial is correlated to laser light incident on the target to within an uncertainty of ~10 ps and originates from the OMEGA HTS. The optical fiducial is sent to the oscilloscope using a fiber optic cable, where it is converted to an electrical signal using a photodiode located just before the input channel. The recorded fiducial pulse is fitted by a pulse train of eight Gaussian distributions spaced apart at the well-characterized period of $\Delta t_f = 548$ ps:

$$\mathrm{fidu}(t) = \sum_{i=0}^{7}\frac{a_i}{\sqrt{2\pi\sigma^2}}\left\{-\left[t-\left(t_0+i\times\Delta t_f\right)\right]^2/2\sigma^2\right\} \tag{9}$$

to the recorded signals. Here, a_i is the amplitude of each fiducial peak, t_0 is the time of the first fiducial pulse, and σ is the width of an individual pulse.

The oscilloscope is timed to within an uncertainty of 1 ns using the measured arrival time of the x-ray pulse and the well-measured distance of the diagnostic to TCC. Furthermore, the fiducial recorded during the calibration including the x-ray pulse is used to preserve the timing for each signal recorded.

Experimental Results and Error Analysis

1. Time-of-Flight Spectra

A first set of experiments used vessels that contained deuterated compounds such as D_2O and C_6D_6 to investigate the breakup of deuterium. Additional measurements were made using vessels filled with standard non-deuterated compounds (H_2O, C_6H_6) in order to identify contributions attributed to the inelastic scattering of oxygen and carbon in the NRV from the 14-MeV neutrons. For each reaction vessel, up to six implosions with yields of $\sim 7 \times 10^{13}$ were performed for both the non-deuterated and deuterated samples. First, the primary D–T yield signal from a separate (monitor) standard diagnostic, which has an uncertainty of 5%, was used to normalize each measured breakup neutron signal to the primary yield.[31] Second, the signals that used one specific vessel were averaged to increase the signal-to-noise ratio. A comparison between the vessels filled with the deuterated and non-deuterated compounds, where the time-of-flight spectra were averaged, clearly shows the contribution from the neutron-induced breakup between the primary DT and D_2 as presented in Fig. 153.7. In both cases, there was the possibility for additional absorption and scattering effects of the neutrons generated in the breakup reaction. A brief discussion on the effects of multiple scattering within the vessel is given in **Multiple Scattering Effects** (p. 9). The measured time-of-flight signal spans up to six orders in magnitude. As previously discussed, these nTOF measurements are achieved by setting each of the four MCP-PMT's to a specific gain. The contributions for each phototube are represented by the different shaded regions. A single excited state (7.0 MeV)

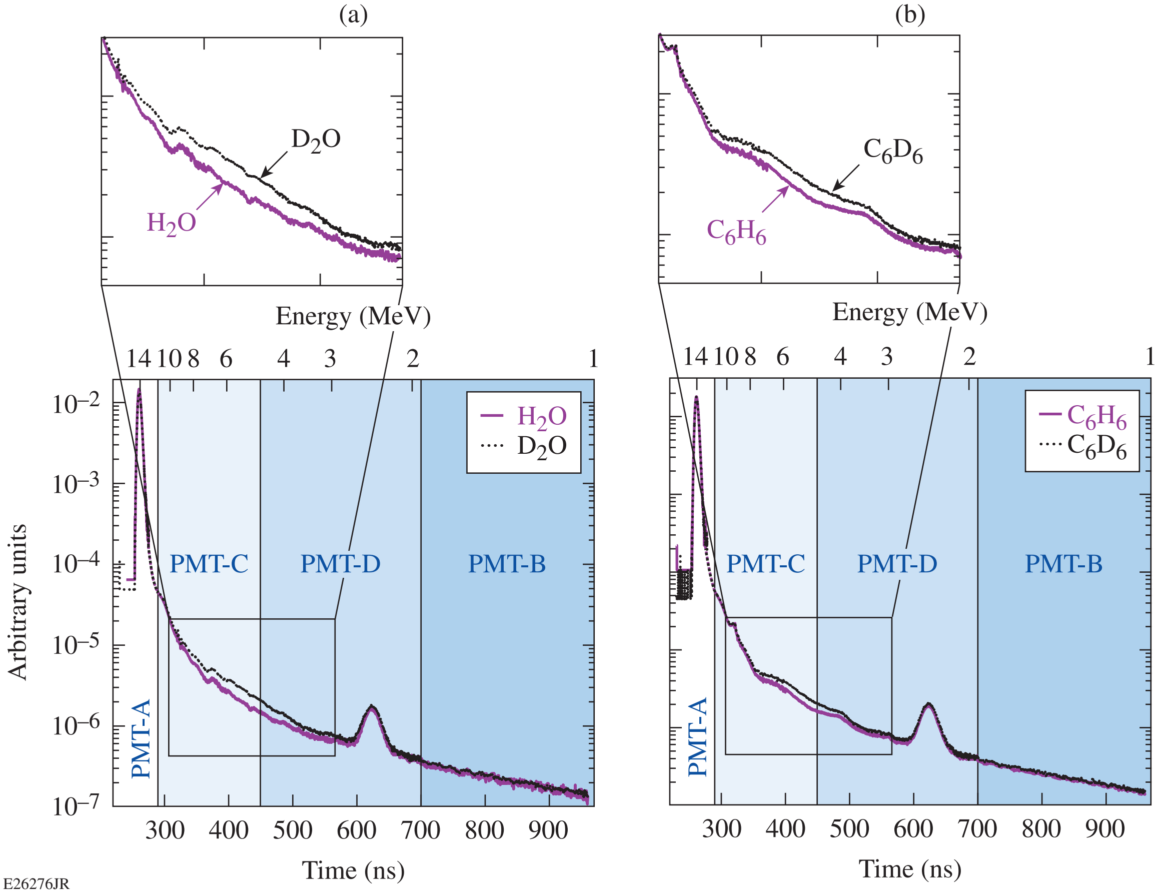

Figure 153.7
A bright neutron source was used to induce a breakup reaction in the reaction vessel filled with deuterated compounds. A comparison of the measured time-of-flight signals clearly indicates the increase in the spectra (1 to 10 MeV) from the breakup of deuterium in the reaction vessel. The excited states of (a) oxygen (7.0 MeV) and (b) carbon (4.44, 7.65, 9.64 MeV) are observed in the time-of-flight spectra.

is seen in spectra from the H_2O and D_2O vessels in addition to several excited states (4.44, 7.65, 9.64 MeV) observed in the spectra from the C_6H_6 and C_6D_6 vessels. An additional test included a vessel filled with a 50/50 mixture of H_2O and D_2O to verify the expected decrease in the neutron signal (see Fig. 153.8) from the breakup caused by the reduction of the deuterium concentration in the compound mixture.

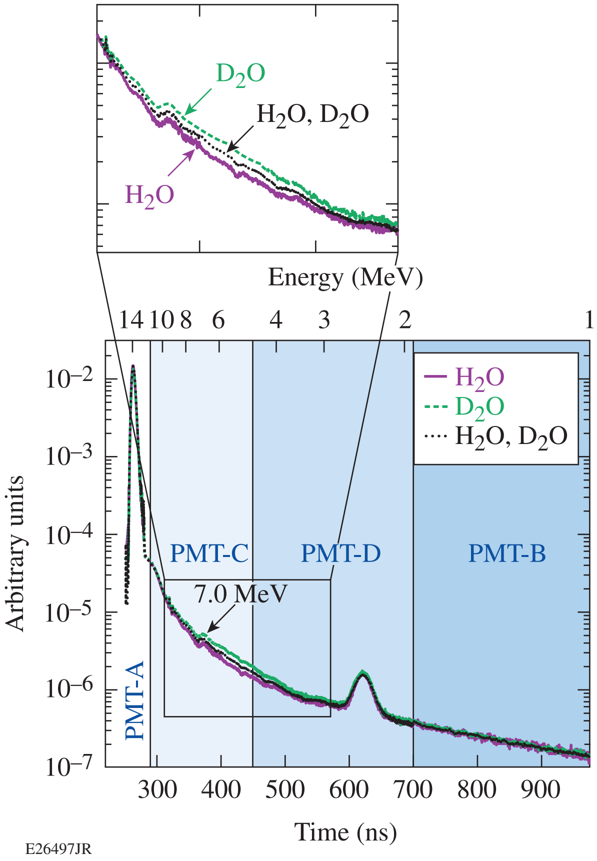

Figure 153.8
Three different vessels filled with water (H_2O), heavy water (D_2O), and an equimolar mixture of water and heavy water were used to measure the nTOF spectrum. A change in the neutron-induced breakup is evident from the vessel filled with the equimolar concentration of H_2O and D_2O.

To extract the deuteron breakup contribution, the signal from the vessel containing the non-deuterated compounds was subtracted from the signal generated from the vessels that retained the deuterated compounds. This approach is advantageous since it removes the contributions from the inelastic scattering of both carbon and oxygen along with any additional scattering and nonlinear scintillator effects that arise from the experimental configuration.

2. Yield Calculation

The residual signal from the subtraction is assumed to be entirely a result of the neutron-induced breakup reaction. To calculate the breakup neutron yield from the measured signal, the experimental neutron yield as a function of energy spectrum is inferred using Eq. (6) as

$$\mathrm{d}Y_{\mathrm{n,2n}}\left(t_{\mathrm{n}}\right)=\frac{k_1}{k_2}\,\frac{1}{\chi_{\mathrm{n}}\left(E_{\mathrm{n}}\right)E_{\mathrm{n}}^{\alpha}}\,I\left(t_{\mathrm{n}}\right)\mathrm{d}t_{\mathrm{n}},\tag{10}$$

where k_1/k_2 is the constant determined from the calibration with D_2 neutrons. The yields for the campaign with the deuterated water and benzene are weighted according to the number of shots on each vessel as measured by the diagnostic for the two separate campaigns. Both campaigns have been restricted to measuring the neutron contribution at or below 10.5 MeV. The neutron spectrum above this energy is dominated by the intense primary D–T yield, obscuring the breakup neutron component. In this experimental setup, the region from 2 MeV to 3 MeV is excluded since the D_2 peak contribution can vary because of the thermal broadening from the fusing plasma.[32]

3. Error Analysis

The error within the $Y_{\mathrm{n,2n}}$ yield measurement can be separated into three categories: statistical error, systematic error, and other uncertainties. The number of neutrons measured in the 13.4-m spectrometer is in the range between 10^4 and 10^5, which leads to a statistical uncertainty of ~1%. Systematic uncertainties are associated with a number of steps involved when calibrating the detector. A significant contribution to uncertainty in the yield measurement arises from the Y_{D_2} yield reference used to calibrate the nTOF spectrometer. A direct *in-situ* calibration method using CR-39 range filter proton detectors has been successfully employed by measuring D–D neutron and proton yields from a series of exploding-pusher implosions on OMEGA.[33] The present D–D yield uncertainty used to cross-calibrate the diagnostic to calculate the cross section is 9%. Upcoming experiments will be performed to further reduce this uncertainty. Another very sensitive detector effect originates from the nonlinear light output of the scintillator required to infer the neutron yield over a broad energy range. For most organic scintillators, the light output is nonlinear for proton recoil energies below 5 MeV, while becoming approximately linear at higher energies. Calculating the yield using the different measured light sensitivities discussed in the literature for the scintillating compound used in this experiment gives a 2% uncertainty.

Inaccuracies in the detection method include signal distortion from the photomultiplier tube, transmission cable, and the recording device. A systematic uncertainty must be taken into consideration when the signals are subtracted from one another. This includes the signal-to-background and the standard deviation in the digitized signal after performing the subtraction. To investigate and qualify the systematic effects from the PMT and cable, offline testing was used to fully characterize the detection system and determine the optimal operating range to ensure signal linearity to within 1%. To quantify the additional scattering contributed from the vessel, two different implosions were performed: one with an empty vessel and one with the vessel and support hardware completely removed from the line of sight. The results show that the introduction of the reaction vessel produced an insignificant amount (<1%) of additional scattering. The inferred yield from the breakup of deuterium with the aforementioned errors added in quadrature as a function of energy is given in Table 153.II.

Table 153.II: The number of breakup neutrons as a function of energy from C_6D_6 and D_2O.

Energy (MeV)	$Y_{\mathrm{n,2n}}$ (C_6D_6) $Y_{\mathrm{DT}} = 7.20 \times 10^{13}$	$Y_{\mathrm{n,2n}}$ (D_2O) $Y_{\mathrm{DT}} = 5.79 \times 10^{13}$
0.5 to 1.0	$2.94 \times 10^4 \pm 7.29 \times 10^4$	N/A
1.0 to 1.5	$3.75 \times 10^4 \pm 3.29 \times 10^4$	$1.32 \times 10^4 \pm 4.87 \times 10^4$
1.5 to 2.0	$1.58 \times 10^4 \pm 1.89 \times 10^4$	$1.98 \times 10^4 \pm 2.75 \times 10^4$
3.0 to 3.5	$5.73 \times 10^4 \pm 9.64 \times 10^3$	$6.74 \times 10^4 \pm 2.09 \times 10^4$
3.5 to 4.0	$6.86 \times 10^4 \pm 2.13 \times 10^4$	$8.07 \times 10^4 \pm 2.61 \times 10^4$
4.0 to 4.5	$1.06 \times 10^5 \pm 1.93 \times 10^4$	$1.29 \times 10^5 \pm 2.50 \times 10^4$
4.5 to 5.0	$1.45 \times 10^5 \pm 1.89 \times 10^4$	$1.66 \times 10^5 \pm 2.79 \times 10^4$
5.0 to 5.5	$1.69 \times 10^5 \pm 2.11 \times 10^4$	$1.98 \times 10^5 \pm 2.65 \times 10^4$
5.5 to 6.0	$1.65 \times 10^5 \pm 1.71 \times 10^4$	$2.00 \times 10^5 \pm 2.59 \times 10^4$
6.0 to 6.5	$1.47 \times 10^5 \pm 1.99 \times 10^4$	$1.81 \times 10^5 \pm 2.48 \times 10^4$
6.5 to 7.0	$1.37 \times 10^5 \pm 1.61 \times 10^4$	$1.83 \times 10^5 \pm 2.74 \times 10^4$
7.0 to 7.5	$1.14 \times 10^5 \pm 1.88 \times 10^4$	$1.53 \times 10^5 \pm 2.04 \times 10^4$
7.5 to 8.0	$9.06 \times 10^4 \pm 1.55 \times 10^4$	$1.47 \times 10^5 \pm 1.80 \times 10^4$
8.0 to 8.5	$9.12 \times 10^4 \pm 1.23 \times 10^4$	$1.42 \times 10^5 \pm 1.50 \times 10^4$
8.5 to 9.0	$8.10 \times 10^4 \pm 1.71 \times 10^4$	$1.20 \times 10^5 \pm 1.60 \times 10^4$
9.0 to 9.5	$5.18 \times 10^4 \pm 6.57 \times 10^4$	$1.06 \times 10^5 \pm 3.71 \times 10^4$
9.5 to 10.0	$6.28 \times 10^4 \pm 1.90 \times 10^4$	$1.14 \times 10^5 \pm 1.42 \times 10^4$
10.0 to 10.5	$6.29 \times 10^4 \pm 3.99 \times 10^4$	$9.46 \times 10^4 \pm 4.77 \times 10^4$
10.5 to 11.0	N/A	$6.41 \times 10^4 \pm 1.20 \times 10^4$

The energy resolution is obtained from the arrival time of the neutrons, which has been absolutely calibrated from the hardware timing fiducial. Lower-energy neutrons span a larger time window with a larger number of digitized bins on the oscilloscope, resulting in a lower uncertainty in the energy resolution (~2 keV). Higher-energy neutrons have an increasingly smaller arrival time window, which reduces the number of bins and leads to a larger uncertainty (~150 keV) in the energy resolution.

4. Angle-Averaged Double-Differential Cross Section

With the yields from the neutron-induced breakup reaction, the double-differential cross section as a function of energy is calculated using the following relation:

$$Y_{\mathrm{n,2n}} = m_{\mathrm{n}} \eta_{\mathrm{D}} \int_0^{l_{\mathrm{NRV}}} \int_0^{\Omega_{\mathrm{dia}}(x_{\mathrm{NRV}})} Y_{\mathrm{inc}}(x_{\mathrm{NRV}}) \times \int_0^{E_{\max}} [\cos(\theta)] \frac{d^2\sigma_{\mathrm{n,2n}}}{\mathrm{d}\Omega \mathrm{d}E} \tau_{\mathrm{NRV}}(E, x_{\mathrm{NRV}}) \times \varepsilon_{\mathrm{dia}}(E) \mathrm{d}E \mathrm{d}\Omega \mathrm{d}x_{\mathrm{NRV}},$$

where

- $Y_{\mathrm{n,2n}}$ = the number of detected neutrons from the neutron-induced breakup reaction,
- m_{n} = the multiplicity for the number of generated neutrons from the breakup ($m_{\mathrm{n}} = 2$),
- η_{D} = the number density of deuterium in the reaction vessel,
- l_{NRV} = the length of the reaction vessel,
- Ω_{dia} (x_{NRV}) = the solid angle of the detector at x_{NRV},
- Y_{inc} (x_{NRV}) = the number of incident 14.03-MeV neutrons at x_{NRV},
- $E_{\max}$ [cos (θ)] = the maximum neutron energy versus laboratory angle θ,
- $d^2\sigma_{\mathrm{n,2n}} / \mathrm{d}\Omega \mathrm{d}E$ = the double-differential cross section for the neutron-induced breakup reaction,
- $\tau_{\mathrm{NRV}}(E, x_{\mathrm{NRV}})$ = the transmission of neutron with energy E through the reaction vessel at x_{NRV}, and

- $\varepsilon_\mathrm{dia}(E)$ = the fraction of neutrons at energy E interacting inside detector.

In the geometry of the experimental setup (see Fig. 153.1), the accepted angle of the breakup neutrons from the reaction vessel to the diagnostic is in the range of 3.5°±3.5°. The angle-averaged $\left\langle d^2\sigma / \mathrm{d}E_\mathrm{n}\mathrm{d}\Omega_\mathrm{n} \right\rangle_\mathrm{NRV}$ double-differential cross section inferred from the time-of-flight measurements using the D_2O and C_6D_6 vessel is shown in Fig. 153.9. The inferred double-differential cross section has been compared with the available experimental data, and recent theoretical calculations are shown in Fig. 153.10. A complete list of the experimental parameters is given in Table 153.III.

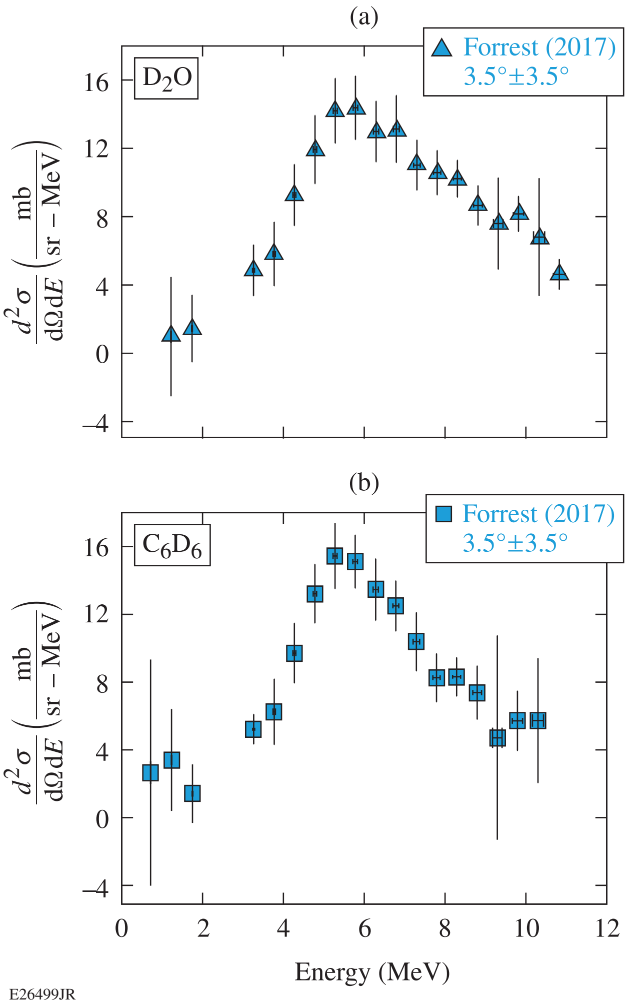

Figure 153.9
(a) The angle-averaged double-differential cross section (triangles) is calculated from the measured neutron yield as a function of energy using the heavy water (D_2O) NRV as the source for the breakup reaction. (b) The angle-averaged (in the range of 3.5°±3.5°) double-differential cross section (squares) is compared to earlier measurements obtained at an angle of 10° (Ref. 34).

5. Multiple Scattering Effects

Scattering of the neutrons generated from the breakup reaction in the vessel could affect the inferred cross section calculated from the neutron yield measured by the diagnostic. The neutron transport code MCNP was used to model the

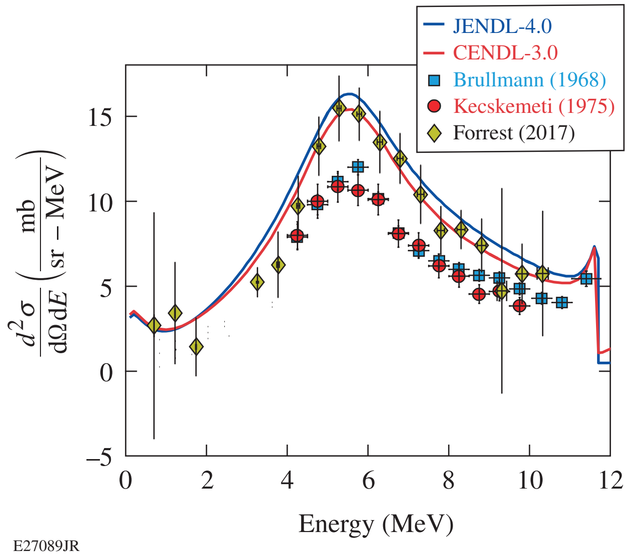

Figure 153.10
Neutron spectra $d^2\sigma/(\mathrm{d}\Omega\mathrm{d}E)$ of the reaction $2H(\mathrm{n},2\mathrm{n})\mathrm{p}$ at a primary neutron energy of 14 MeV. The inferred double-differential cross section from OMEGA has been compared with available experimental data and recent theoretical calculations.

Table 153.III: The geometric parameters for the experimental setup.

Equipment	Parameter	in cm
Nuclear reaction vessel (NRV)	$d_\mathrm{face\ NRV}$	8.80
	x_NRV	$x_\mathrm{NRV} = 0 < x_\mathrm{NRV} < l_\mathrm{NRV}$
	l_NRV	7.501
	$r_\mathrm{face\ NRV}$	0.483
	$r_\mathrm{rearA\ NRV}$	2.169
	$r_\mathrm{rearB\ NRV}$	1.676
	$l_\mathrm{cone\ NRV}$	5.885
	$l_\mathrm{rearA\ NRV}$	7.145
Mid-beam collimator (MBC)	d_face	737.2
	r_MBC	5.588
	l_MBC	71.12
13.4-m neutron time of flight (nTOF)	d_face	1340
	x_dia	$0 < x_\mathrm{dia} < l_\mathrm{dia}$
	l_dia	10.16
	r_dia	10.16

experimental setup.[24] The simulations included a high-yield neutron source incident on a nuclear reaction vessel and an infinitely thin plane (surface of the diagnostic) positioned 13.4 m away. A special tally program was written that extracted only the neutrons that were born from the neutron-induced breakup and crossed the surface of the detector plane. This tally recorded the location of the last scatter event in the vessel, the number of scatter events in the vessel, the type of scatter event it underwent (i.e., elastic, inelastic, etc.), and which element had an event. This information was used to interpret the addition of multiple scattering of the neutrons as they exited the vessel and crossed the surface of the diagnostic. These simulations show that the energy spectrum is affected only at energies below 1 MeV (<3%).

Summary and Discussion

In summary, high-quality data have been recorded using an ICF platform to induce the breakup reaction of deuterium and infer the angle-averaged double-differential cross section. The experiment measured the energy spectrum of the deuterium breakup reaction from 0.5 MeV to 10.5 MeV averaged over an angular region from $\theta_{\text{lab}} = 3.5^\circ \pm 3.5^\circ$. A statistical uncertainty of ~1% is inferred with a systematic uncertainty of ~10% for the measured neutron yield used to calculate the cross section for the induced breakup of deuterium. This cross section has been compared to earlier experimental measurements for an accelerator-based platform. This experiment highlights that the OMEGA Laser System provides a unique platform on which to study neutron-induced reactions with a high signal-to-background ratio in a single campaign.

Future experiments will focus on upgrading our diagnostics to resolve the final-state interaction peak at 11.8 MeV. These improvements include higher-bit analog-to-digital converter oscilloscopes and faster gate units with less than 2-ns recovery times.

Additional reaction vessels have been constructed that contain other light-Z elements such as ^{7}Li and ^{9}Be to measure the (n,2n) reactions. There is sparse data for ^{7}Li with large differences in the published measurements. Recent experiments on OMEGA have measured the inelastic scattering of 14-MeV neutrons from ^{7}Li. Initial measurements indicate a measurable neutron energy spectrum. Detailed analysis is underway to infer the neutron-induced breakup reaction from the experimental data. A larger measurement database exists for ^{9}Be, and it would be useful to compare data from an implosion neutron source with an accelerator neutron source.

ACKNOWLEDGMENT

This material is based upon work supported by the Department of Energy National Nuclear Security Administration under Award Number DE-NA0001944, the University of Rochester, and the New York State Energy Research and Development Authority.

REFERENCES

1. C. D. Zhou and R. Betti, Phys. Plasmas **15**, 102707 (2008); **16**, 079905(E) (2009).
2. T. R. Boehly, D. L. Brown, R. S. Craxton, R. L. Keck, J. P. Knauer, J. H. Kelly, T. J. Kessler, S. A. Kumpan, S. J. Loucks, S. A. Letzring, F. J. Marshall, R. L. McCrory, S. F. B. Morse, W. Seka, J. M. Soures, and C. P. Verdon, Opt. Commun. **133**, 495 (1997).
3. J. Nuckolls *et al*., Nature **239**, 139 (1972).
4. S. Atzeni and J. Meyer-ter-Vehn, *The Physics of Inertial Fusion: Beam Plasma Interaction, Hydrodynamics, Hot Dense Matter*, 1st ed., International Series of Monographs on Physics, Vol. 125 (Oxford University Press, Oxford, 2004).
5. G. S. Fraley and R. J. Mason, Phys. Rev. Lett. **35**, 520 (1975).
6. J. M. Soures, R. L. McCrory, C. P. Verdon, A. Babushkin, R. E. Bahr, T. R. Boehly, R. Boni, D. K. Bradley, D. L. Brown, R. S. Craxton, J. A. Delettrez, W. R. Donaldson, R. Epstein, P. A. Jaanimagi, S. D. Jacobs, K. Kearney, R. L. Keck, J. H. Kelly, T. J. Kessler, R. L. Kremens, J. P. Knauer, S. A. Kumpan, S. A. Letzring, D. J. Lonobile, S. J. Loucks, L D. Lund, F. J. Marshall, P. W. McKenty, D. D. Meyerhofer, S. F. B. Morse, A. Okishev, S. Papernov, G. Pien, W. Seka, R. Short, M. J. Shoup III, M. Skeldon, S. Skupsky, A. W. Schmid, D. J. Smith, S. Swales, M. Wittman, and B. Yaakobi, Phys. Plasmas **3**, 2108 (1996).
7. J.-M. Laborie *et al*., Eur. Phys. J. A **48**, 87 (2012).
8. J. S. C. McKee, Rep. Prog. Phys. **33**, 691 (1970).
9. C. J. Forrest, V. Yu. Glebov, V. N. Goncharov, J. P. Knauer, P. B. Radha, S. P. Regan, M. H. Romanofsky, T. C. Sangster, M. J. Shoup, and C. Stoeckl, Rev. Sci. Instrum. **87**, 11D814 (2016).
10. J. H. Nuckolls, Lawrence Livermore National Laboratory, Livermore, CA, Report UCRL-ID-131075 (1988).
11. E. B. Goldman, J. A. Delettrez, and E. I. Thorsos, Nucl. Fusion **19**, 555 (1979).
12. J. Nuckolls, J. Emmett, and L. Wood, Phys. Today **26**, 46 (1973).
13. C. Stoeckl, R. Boni, F. Ehrne, C. J. Forrest, V. Yu. Glebov, J. Katz, D. J. Lonobile, J. Magoon, S. P. Regan, M. J. Shoup III, A. Sorce, C. Sorce, T. C. Sangster, and D. Weiner, Rev. Sci. Instrum. **87**, 053501 (2016).
14. C. J. Forrest, P. B. Radha, V. Yu. Glebov, V. N. Goncharov, J. P. Knauer, A. Pruyne, M. Romanofsky, T. C. Sangster, M. J. Shoup III, C. Stoeckl, D. T. Casey, M. Gatu-Johnson, and S. Gardner, Rev. Sci. Instrum. **83**, 10D919 (2012).
15. C. Stoeckl, M. Cruz, V. Yu. Glebov, J. P. Knauer, R. Lauck, K. Marshall, C. Mileham, T. C. Sangster, and W. Theobald, Rev. Sci. Instrum. **81**, 10D302 (2010).

16. R. Lauck *et al*., IEEE Trans. Nucl. Sci. **56**, 989 (2009).
17. Photek Ltd., St. Leonards on Sea, East Sussex, TN38 9NS, United Kingdom.
18. DG645 Digital Delay Generator, Stanford Research Systems Inc., Sunnyvale, CA 94089-2279.
19. Pasternack, Irvine, CA, 92614-6002.
20. Tektronix Inc., Beaverton, OR 97077.
21. Teledyne Isco, Lincoln, NE 68504-1328.
22. BroadWave Technologies, Greenwood, IN, 46143-1443.
23. Keysight Technologies Inc., Santa Rosa, CA 95403-1738.
24. X-5 Monte Carlo Team, Los Alamos National Laboratory, Los Alamos, NM, Report LA-UR-03-1987 (2008).
25. M. B. Chadwick *et al*., Nucl. Data Sheets **107**, 2931 (2006).
26. G. F. Knoll, *Radiation Detection and Measurement*, 3rd ed. (Wiley, New York, 2000).
27. B. von Krosigk *et al*., Eur. Phys. J. C **73**, 2390 (2013).
28. R. L. Craun and D. L. Smith, Nucl. Instrum. Methods **80**, 239 (1970).
29. V. V. Verbinski *et al*., Nucl. Instrum. Methods **65**, 8 (1968).
30. V. Yu. Glebov, T. C. Sangster, C. Stoeckl, J. P. Knauer, W. Theobald, K. L. Marshall, M. J. Shoup III, T. Buczek, M. Cruz, T. Duffy, M. Romanofsky, M. Fox, A. Pruyne, M. J. Moran, R. A. Lerche, J. McNaney, J. D. Kilkenny, M. J. Eckart, D. Schneider, D. Munro, W. Stoeffl, R. Zacharias, J. J. Haslam, T. Clancy, M. Yeoman, D. Warwas, C. J. Horsfield, J.-L. Bourgade, O. Landoas, L. Disdier, G. A. Chandler, and R. J. Leeper, Rev. Sci. Instrum. **81**, 10D325 (2010).
31. O. Landoas, V. Yu. Glebov, B. Rossé, M. Briat, L. Disdier, T. C. Sangster, T. Duffy, J. G. Marmouget, C. Varignon, X. Ledoux, T. Caillaud, I. Thfoin, and J.-L. Bourgade, Rev. Sci. Instrum. **82**, 073501 (2011).
32. H. Brysk, Plasma Phys. **15**, 611 (1973).
33. C. J. Waugh, M. J. Rosenberg, A. B. Zylstra, J. A. Frenje, F. H. Séguin, R. D. Petrasso, V. Yu. Glebov, T. C. Sangster, and C. Stoeckl, Rev. Sci. Instrum. **86**, 053506 (2015).
34. M. Brullmann *et al*., Nucl. Phys. A **117**, 419 (1968)

Record Fifth-Harmonic–Generation Efficiency Producing 211-nm, Joule-Level Pulses Using Cesium Lithium Borate

Introduction

High-energy ultraviolet (UV) sources are now required to probe hot dense plasmas, where deep UV probes provide a better penetration of the plasma.[1] For fusion experiments, measuring Thomson scattering of 5ω pulses as a diagnostic technique is promising because there is less self-generated background from the plasma in the spectral region from 180 to 230 nm (Refs. 2 and 3). More generally, all-solid-state UV lasers can address applications traditionally supported by excimer gas lasers.[4]

Fifth-harmonic generation (5HG) of neodymium lasers was first demonstrated in 1969 (Ref. 5) using a KDP (potassium dihydrogen phosphate) crystal to mix the fourth harmonic with the residual beam at the fundamental frequency: $4\omega + \omega = 5\omega$. ADP (ammonium dihydrogen phosphate) crystals were later used in a similar configuration.[6–8] Both KDP and ADP crystals must be cooled to cryogenic temperatures in order for this process to be phase matched. Fifth-harmonic generation was achieved at room temperature using crystals of potassium pentaborate tetrahydrate (KB5),[9,10] urea,[11] β-barium borate (BBO),[12] and cesium lithium borate (CLBO).[13] All of these experiments used small-aperture beams and had relatively low efficiency. As a result, real applications of 5HG have been rare.[14]

Although common crystals such as BBO have been used to generate the fifth harmonic,[15] joule-level applications require crystals that can be grown to sizes suitable for large-aperture beams (~25 mm or greater). KDP and ADP crystals can be grown in meter-scale sizes; the 20%-efficient 5HG of wide-aperture neodymium glass was first reported in an ADP crystal.[16] However, maintaining a cryogenic temperature with sub-degree-Kelvin uniformity throughout the ADP crystal, as required for phase matching, adds significant complexity for large-aperture applications.[17] Another candidate is CLBO, which can also be grown in large sizes.[13] In this article we demonstrate 30%-efficient, joule-class fifth-harmonic conversion of 1053-nm pulses using a 30-mm-diam CLBO crystal.

Experiment

Figure 153.11 shows the experimental setup with the cascade of three nonlinear crystals. The final crystal, made of CLBO, was located at the image plane of a Nd:YLF laser[18] that was optimized to produce a flattopped, square-beam profile with a square pulse (1053 nm, 12 × 12 mm, from 1 ns to 2.8 ns, ≤1.5 J, 5 Hz or 0.1 Hz). The first frequency doubler was a deuterated potassium dihydrogen phosphate (DKDP) crystal, which was chosen instead of KDP to decrease linear absorption at the fundamental frequency. It was cut in a Type-II configuration (30 × 30 × 27 mm) to convert $1\omega \longrightarrow 2\omega$. A second frequency doubler, a Type-I KDP crystal (30 × 30 × 15.5 mm), was used to convert $2\omega \longrightarrow 4\omega$.

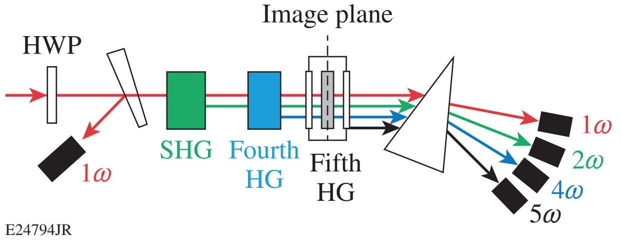

Figure 153.11
Experimental setup showing the input laser beam, conversion crystals, and energy diagnostics for each frequency: second-harmonic generation (SHG) in deuterated potassium dihydrogen phosphate (DKDP), Type II; fourth-harmonic generation (4HG) in KDP, Type I; and fifth-harmonic generation (5HG) in cesium lithium borate (CLBO), Type I. HWP: half-wave plate.

A CLBO crystal from Coherent (30-mm diam × 4 mm), which was cut for Type-I phase-matching conversion, mixed the residual 1ω with the 4ω to produce 5ω pulses. Because of its hygroscopic properties, it was housed in an oven and heated to 120°C. The crystal orientations relative to the input beam polarization are shown in Fig. 153.12. The angle α between input-beam polarization and the horizontal plane was tuned using the half-wave plate (HWP) before the first crystal to change the balance of energy between the ordinary and extraordinary axes in the first Type-II doubler and to preserve some fraction of the fundamental frequency beam through

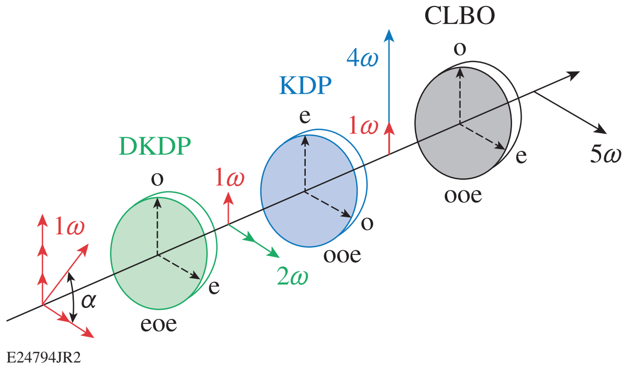

Figure 153.12
Schematic showing the orientation of the crystal axes and polarizations. The angle (α) of the 1ω polarization was set using a HWP for optimal conversion. e: extraordinary; o: ordinary.

the first two crystals for the interaction in the last crystal. The input and output beam energies were measured using identical pyroelectric energy meters that were cross calibrated. All beam profiles were recorded.

Results

Frequency conversion efficiencies from 1$\omega \longrightarrow$ 2ω and 2$\omega \longrightarrow$ 4ω are shown in Fig. 153.13 and demonstrate a good agreement with plane-wave conversion calculations. For the doubling calculation, we assumed an effective nonlinearity of 0.31 pm/V for the DKDP Type-II doubler, an angular detuning of 200 μrad (internal angle) from phase matching, and an equal split of 1ω input into the two polarization axes of the doubler crystal. For the quadrupling calculation, a Type-I KDP quadrupling crystal is assumed to have an effective nonlinearity of 0.45 pm/V with an angular detuning of 50 μrad.

To maximize the 5ω output energy, the efficiency of the second-harmonic–generation (SHG) process was lowered to preserve some portion of energy at fundamental frequency for the (1ω + 4ω) process. The maximum of 5ω energy reached with a 2.4-ns pulse was 335 mJ.

The fifth-harmonic efficiency $\eta(5\omega)$, shown in Fig. 153.14, is defined as the ratio of 5ω output energy after the CLBO oven to the 1ω energy at the input of the first (DKDP) crystal. The maximum $\eta(5\omega)$ conversion efficiency of 30.5% was reached with a 2.4-ns pulse and an input intensity of 0.3 GW/cm^2. This definition of efficiency describes the portion of the input 1ω energy that has been transformed into the fifth harmonic and is available at the output of the cascade of crystals for use in any application. However, this definition depends on technical factors not directly related to the performance of the CLBO crystal, such as the quality of antireflection coatings on all of the crystals and oven windows, absorption in the first two doubling crystals, etc.; therefore, this efficiency metric does not provide an accurate description of the physics of the mixing (1ω + 4ω) process. Other publications have proposed alternate methods to calculate 5HG efficiency such as the fraction ratio (FR) of 5ω energy after the last crystal to the total energy output at all wavelengths,[16] or as a ratio of 5ω energy after the last crystal to the 1ω energy at the input of the last crystal.[15] A quantum efficiency (QE) for the process can be defined as the ratio of the number of photons after all the crystals, 5ω to (4ω + 5ω),

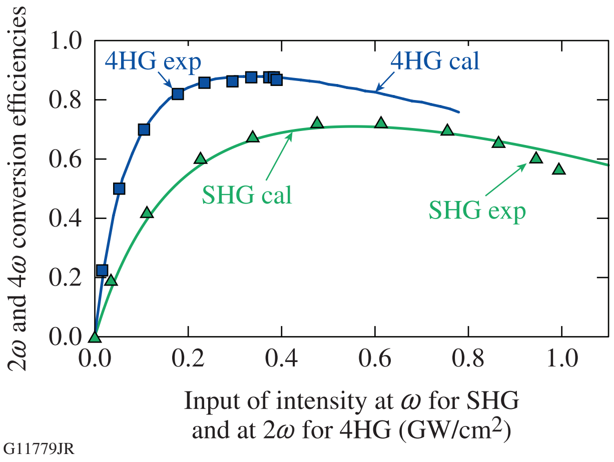

Figure 153.13
SHG and 4HG efficiencies measured as a function of input-pulse intensity.

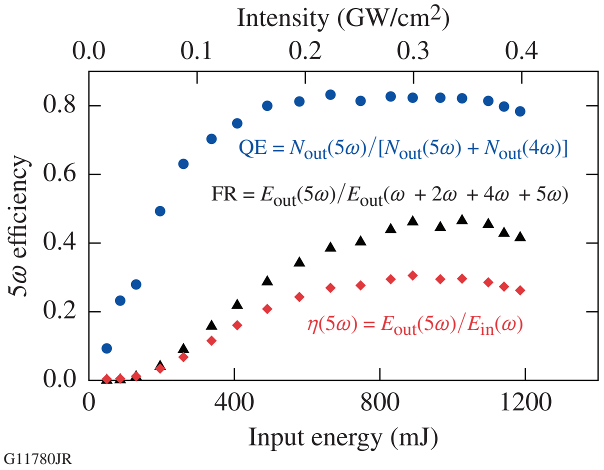

Figure 153.14
Measurement of 5HG efficiencies according to three definitions.

which has an ideal value of 100% when all 4ω photons are converted into 5ω photons. The best QE that was observed in this experiment exceeded 80%; i.e., despite the complexity of the interaction, four of the five photons of 4ω were converted.

The temperature acceptance of 5HG in CLBO at three different crystal position angles was measured (see Fig. 153.15). Angular acceptance of 5HG at a given temperature of the CLBO crystal was also measured (Fig. 153.16). The measured acceptances agree well with the simulations.

The 5HG energy was optimized by adjusting the angle α to set 1ω intensity at the CLBO for a 1-ns pulse (see Fig. 153.17). The optimal angle depends on input-beam intensity, so fine tuning should be done close to the range of the best 5ω generation.

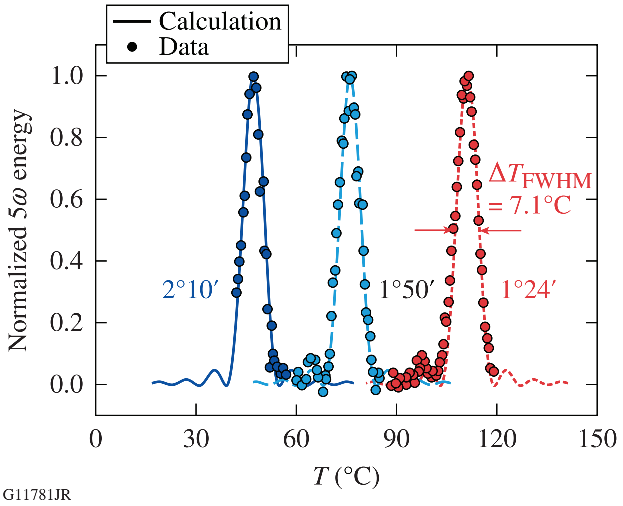

Figure 153.15
Fifth-harmonic energy temperature (T) acceptance at three different position angles of the CLBO crystal. FWHM: full width at half maximum.

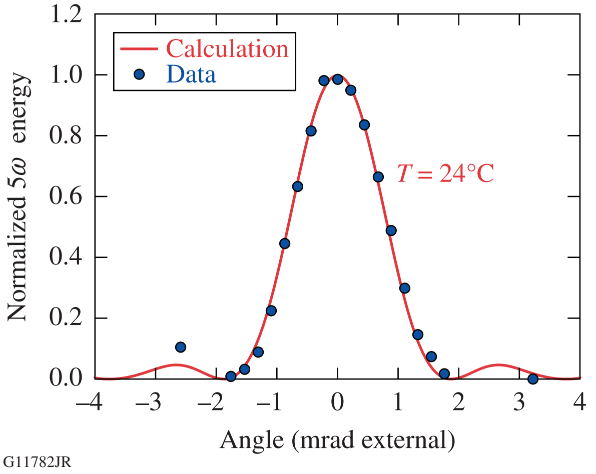

Figure 153.16
Fifth-harmonic energy angular acceptance of the CLBO crystal.

Figure 153.18 shows quantities derived from energy measurements plotted as a function of input energy and intensity with a 1-ns pulse. In addition to the fifth-harmonic efficiency $\eta(5\omega)$, which is defined above, the figure shows the energy balance B, which is the ratio of the total energy of all beams

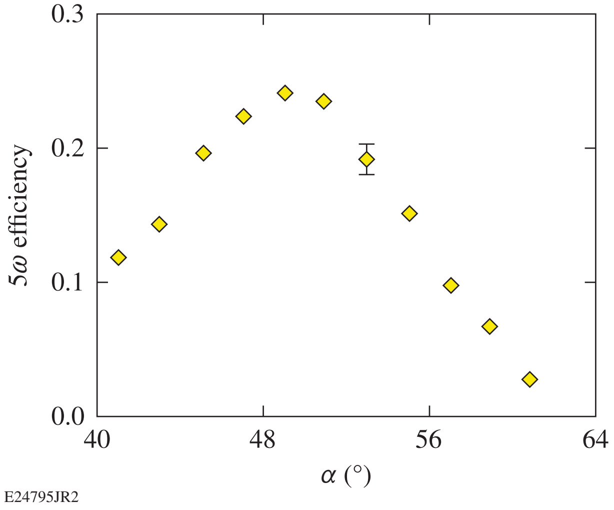

Figure 153.17
Fifth-harmonic efficiency as a function of input polarization direction.

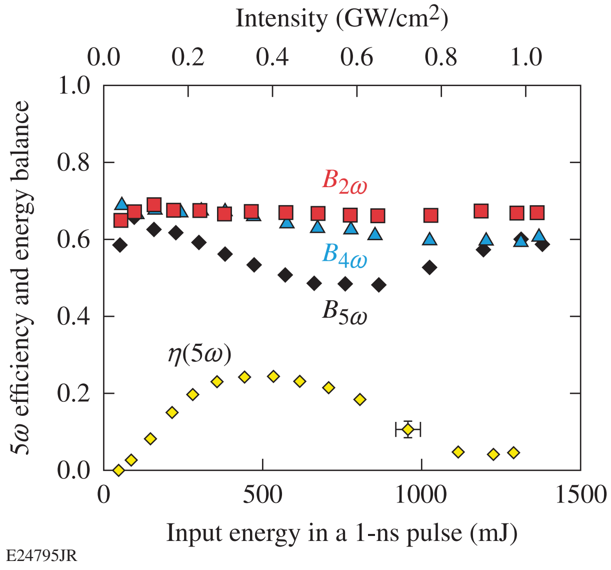

Figure 153.18
Fifth-harmonic efficiency and energy balance measured as a function of input-pulse energy and intensity. $B_{2\omega}$, $B_{4\omega}$, and $B_{5\omega}$ are the energy balances measured by phase matching the crystals for a maximum frequency of 2ω, 4ω, and 5ω, respectively.

after the oven to the 1ω energy at the input; B, therefore, represents the fraction of energy transmitted from input to output. The subscript denotes the maximum harmonic frequency present, which was set by detuning crystals to suppress 5ω or 4ω generation.

A 5ω conversion efficiency of 25% was reached with a 1-ns pulse and an input intensity of 0.4 GW/cm^2. Strong back-conversion occurred at higher intensities, reducing the overall efficiency. The energy balance B at low intensities was only 70%, primarily caused by losses from uncoated surfaces of the CLBO and the output oven window, and 1ω reflections from the KDP crystal surfaces. It is expected that the overall 5ω efficiency could be significantly improved by reducing these losses.

The variation in energy balance at higher intensities shows that nonlinear loss mechanisms are also present. While the 4ω and 5ω photon energies are below the band gap of CLBO, any combination of the two [$(4\omega + 4\omega)$, $(4\omega + 5\omega)$, and $(5\omega + 5\omega)$] exceeds the band gap and initiates two-photon absorption (TPA) in CLBO. This nonlinear process dominates at a high intensity and becomes the most-limiting factor for efficient 5HG. By detuning the crystals to suppress 5ω or 4ω generation, the relative significance of two-photon absorption of 4ω and 5ω light was determined. With all crystals optimized ($B_{5\omega}$), any combination of TPA can occur, but with the CLBO crystal detuned ($B_{4\omega}$), only $(4\omega + 4\omega)$ is relevant. The difference between the three energy balance curves shows that TPA from $(4\omega + 5\omega)$ and $(5\omega + 5\omega)$ is the main nonlinear loss mechanism, whereas the $(4\omega + 4\omega)$ process is relatively weak. TPA coefficients β at 5ω measured in the CLBO crystal, in a UV-grade fused-silica window, and in air are 1.2 cm/GW, 0.5 cm/GW, and 0.0008 cm/GW, respectively.

Another factor that limits 5HG is the temperature nonuniformity across the CLBO crystal. Figure 153.19 shows beam profiles of the input beam before the first crystals and fifth-harmonic beam after the oven. Compared to the relatively uniform 1ω beam, the 5ω beam varied spatially and was significantly smaller. By temperature tuning, the optimal zone of 5ω generation could be moved vertically across the CLBO crystal, demonstrating that the nonuniformity of the 5ω beam was caused by phase mismatch inside the CLBO crystal. Independent temperature measurements also demonstrated a similar thermal gradient of the CLBO crystal inside the oven. Therefore, improving an oven to produce a more-uniform temperature across the CLBO crystal would increase the 5ω generation efficiency beyond 30%.

ACKNOWLEDGMENT

This material is based upon work supported by the Department of Energy National Nuclear Security Administration under Award Number DE-NA0001944, the University of Rochester, and the New York State Energy Research and Development Authority.

REFERENCES

1. V. V. Ivanov, A. A. Anderson, and I. A. Begishev, Appl. Opt. **55**, 498 (2016).
2. J. S. Ross, S. H. Glenzer, J. P. Palastro, B. B. Pollock, D. Price, G. R. Tynan, and D. H. Froula, Rev. Sci. Instrum. **81**, 10D523 (2010).
3. P. Datte, J. S. Ross, D. Froula, J. Galbraith, S. Glenzer, B. Hatch, J. Kilkenny, O. Landen, A. M. Manuel, W. Molander, D. Montgomery, J. Moody, G. Swadling, J. Weaver, G. Vergel de Dios, and M. Vitalich, J. Phys.: Conf. Ser. **717**, 012089 (2016).
4. *Excimer Laser Technology*, edited by D. Basting and G. Marowsky (Springer-Verlag, Berlin, 2005).

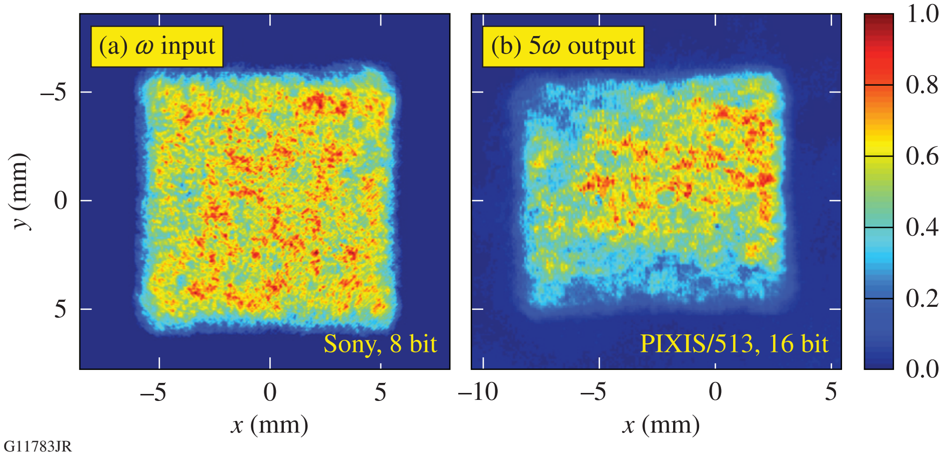

G11783JR

Figure 153.19
(a) Input beam at the fundamental frequency on the front of the cascade of crystals and (b) fifth-harmonic output beam after the oven.

5. A. G. Akmanov *et al*., J. Exp. Theor. Phys. Lett. **10**, 154 (1969).

6. G. A. Massey, Appl. Phys. **24**, 371 (1974).

7. G. Massey, M. Jones, and J. Johnson, IEEE J. Quantum Electron. **14**, 527 (1978).

8. M. Jones and G. Massey, IEEE J. Quantum Electron. **15**, 204 (1979).

9. K. Kato, Opt. Commun. **19**, 332 (1976).

10. A. G. Arutyunyan *et al*., Sov. Tech. Phys. Lett. **6**, 120 (1980).

11. K. Kato, IEEE J. Quantum Electron. **QE-16**, 810 (1980).

12. C. Chen *et al*., Proc. SPIE **681**, 12 (1986).

13. Y. K. Yap *et al*., Opt. Lett. **21**, 1348 (1996).

14. A. Lago *et al*., Opt. Lett. **13**, 221 (1988).

15. A. Dubietis *et al*., J. Opt. Soc. Am. B **17**, 48 (2000).

16. I. A. Begishev, R. A. Ganeev, A. A. Gulamov, E. A. Erofeev, Sh. R. Kamalov, T. Usmanov, and A. D. Khadzhaev, Sov. J. Quantum Electron. **18**, 224 (1988).

17. I. A. Begishev, R. A. Ganeev, V. V. Gorbushin, A. A. Gulamov, Sh. R. Kamalov, and T. Usmanov, J. Appl. Spectrosc. **51**, 1218 (1989).

18. V. Bagnoud, M. J. Guardalben, J. Puth, J. D. Zuegel, T. Mooney, and P. Dumas, Appl. Opt. **44**, 282 (2005).

An Ultrafast X-Ray Streak Camera for Time-Resolved High-Energy-Density Applications

Introduction

The x-ray streak camera is an instrument that is frequently called upon to measure the temporal variation of x-ray signals in ultrafast (~10^{-12} s) experiments. The x-ray streak camera finds use in the fields of spectroscopy[1–3] and imaging[4–7] of high-energy-density (HED) physics experiments, where the temporal duration of the HED material to be examined is set by the inertial confinement time; in the case of highly compressed solid-density plasma, this can be as brief as tens of picoseconds. Characterization of the emitted x rays yields information about the ionization state,[8] electron density,[9] and temperature[10] of the material at a high energy density. This necessitates a streak camera with high temporal resolution (~a few picoseconds) and spatial resolution since the system evolves rapidly and experimental measurements require detailed, finely resolved measurements of the x-ray radiation.

Using the x-ray streak camera, one can measure the short-duration x-ray signals through a series of conversions to electrons and visible photons, each with an associated gain and additive noise that serves to increase uncertainty in the measured signal. An x-ray pulse incident on the photocathode of the x-ray streak camera yields a number of photoelectrons with an energy spread of a few electron volts.[11] The electron pulse is accelerated in a high gradient field to kilo-electron-volt energies and then imaged with an electro-optical system onto a phosphorescent screen coupled to a low-noise charge-coupled–device (CCD) array for recording. The intrinsic capability of the x-ray streak camera sets fundamental constraints on the fidelity of experimental studies and therefore requires careful consideration. The comparison of streak image data to models requires a fundamental understanding of the camera's sensitivity, so that enough photons can be measured to adequately constrain the measurement.

In the series of measurements detailed in this article, the performance of the streak camera has been assessed through dynamic tests with a pulsed laser source in addition to static imaging and sensitivity tests with a soft x-ray source. The streak camera is used in a variety of spectroscopic applications[12–14] at LLE. The following sections (1) describe the essential features of the streak camera's imaging system and the experimental setup for characterizing the camera; (2) describe the calibration of the time base in the camera; (3) discuss the best focusing of the tube and the spatial- and temporal-resolution elements of the camera; (4) discuss the intrinsic gain of the camera in terms of recorded CCD electrons per photoelectron associated with this camera configuration; (5) discuss the effect of space-charge broadening and the linear dynamic range of the camera relative to the number of photoelectrons per resolution element; and (6) present a brief discussion of the implications of these measurements.

Camera System Layout

Figure 153.20 shows a layout of the streak camera and the testing apparatus setup. The streak camera described here is the third generation of an x-ray streak system built on the PJX streak tube[15] and Rochester Optical Streak System (ROSS) electronics.[16] The ultrafast sweep pulser was built by Kentech Instruments.[17] The camera consists of a removable photocathode plate, a streak tube that opens directly into the vacuum chamber, a phosphorescent window at the output of the tube, and an image recording system to digitize the phosphor image at the output vacuum window. The photocathode plate holder is interchangeable and the photocathode may be changed based on the experimental application. The photoelectrons generated from the photocathode are accelerated through a 3-kV/mm gradient field via a 5-mm gap and are imaged by a quadrupole-doublet electron focusing geometry. The nature of the doublet allows for two magnification modes to be controlled by the polarity of the quadrupole voltages. The standard polarity mode images a 60-mm × 0.4-mm^2 region of the photocathode with 0.4× magnification. Inverting the polarity of the two quadrupoles reverses the magnifications, which images the central 6 × 0.1 mm^2 of the photocathode. The electrons passing through the slot appear to come from a virtual photocathode[18] focusing electrons from a virtual point source behind the physical photocathode with a spot size ultimately limited by the transverse electron energy distribution.

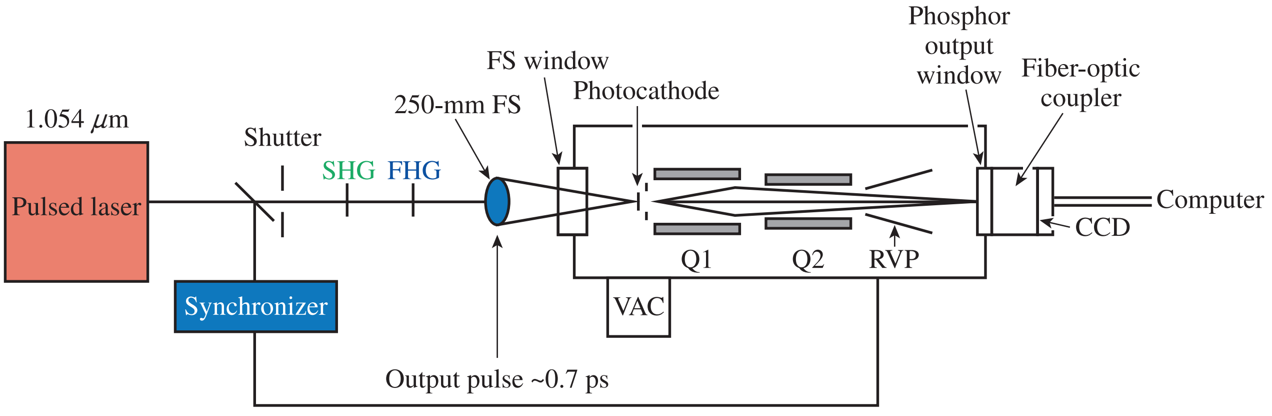

Figure 153.20
The experimental configuration for testing the third-generation x-ray streak camera. A subpicosecond 263-nm laser is pulsed onto the photocathode focused by a 250-mm-focal-length fused-silica double convex lens. The signal is converted to photoelectrons at the photocathode where they are accelerated through a 3-kV/mm gradient field and focused by a quadrupole doublet (QP1 and QP2) and streaked by a high-voltage transient applied to the ramping voltage plates (RVP's) and synchronized to the laser pulse. Photons generated at the phosphor output window are fiber optically coupled to a scientific charge-coupled device (CCD) and readout by computer. FS: fused silica; SHG: second-harmonic generation; FHG: fourth-harmonic generation; VAC: vacuum.

The output screen is recorded by a Spectral Instruments Series 1000 scientific CCD camera with a back-illuminated E2V 42-40 chip with 13.5-μm pixel pitch and free of cosmetic defects. The image from the output screen is relayed to the CCD through an Incom fiber-optic coupler. The CCD is operated at a temperature of –30°C, and the digitization noise from the CCD array is 4.2 photoelectrons; the gain is 0.7 electrons/ADU (analog-to-digital unit) as measured by the photon transfer method of Janesick *et al.*[19] The streak camera has two sweeping rates, accessed through separate high-voltage pulser circuits, with a window of nominally 1 ns and 5 ns, which were measured in this study.

The final digital output from the camera is a 2048 × 2048 16-bit array. The first dimension of the array corresponds to a spatial view along the length of the slit, where one pixel corresponds to 3 μm in inverse mode and 30 μm in standard mode. The second dimension is an image of the slit that is swept in time across the image.

Experimental Technique

1. Time-Base Calibration

The time base—the relationship between the sweep and on-screen location in the image—was characterized for stability and reproducibility. The streak camera operates by applying fast voltage transients to a pair of deflection plates; a series of such transients were recorded using the camera. The repeatable operation of the stack of the avalanche voltage pulser is necessary to obtain a reliable performance of the sweeping circuit. A subpicosecond (0.7-ps) Nd:glass (1.054-μm) laser pulse[20,21] is frequency quadrupled to provide a UV pulse suitable for generating photoelectrons on a gold photocathode (200 Å) supported on a 1-μm parylene substrate. Half of the UV pulse is retarded by a quartz plate that provides a calculated fixed delay of 11.2 ps to the pulse with respect to the undelayed beam. The timing between the laser pulse and the streak camera triggering is varied to advance the two pulses across the swept region in the streaked image. This procedure is repeated a number of times across the sweep window. The distance in pixels between the two peaks is recorded along with the location of the two pulses in the streak image. The dwell time per pixel of the signal is calculated by dividing the distance in pixels between the two peaks against the known delay of the quartz plate. A representative image from the camera and the fitted data are shown in Figs. 153.21(a) and 153.21(b), respectively.

The double pulse was time delayed with respect to the ramping voltage trigger to trace out the shape of the deflected beam on the CCD. The results of the sweep rate measurement and a fit are plotted in Fig. 153.22(a). The data show a dwell time that is, at a minimum, close to the center of the sweeping window. A fourth-order polynomial fit is calculated to parameterize the sweep speed as a function of the on-chip location. The uncertainty in the time base originates from the fact that the ramp voltage applied to the deflection plates for each sweep is slightly different on each triggering. In the data set in Fig. 153.22(a), each point on the plot represents an independent sweep and therefore a sample of the distribution of possible sweep rates at that location. An envelope of possible sweep rates [shown by the ±2σ curves on either side of the fitted data in Fig. 153.22(a)] gives a bound on the possible sweep rates for an independent sweep. This is converted to the time base uncertainty by calculating the cumulative sum of the bounds to the fits. This is shown in Fig. 153.22(b), with the fitted time base and possible other time bases. Over the entire swept window, this cumulative sum adds to 40 ps over the 900-ps record length, which yields a systematic uncertainty in the measurement of two points in time of <5%. The results are listed in Table 153.IV. With the time base measured, the impulse response of the camera is also characterized by measuring the apparent temporal width of the subpicosecond pulse.

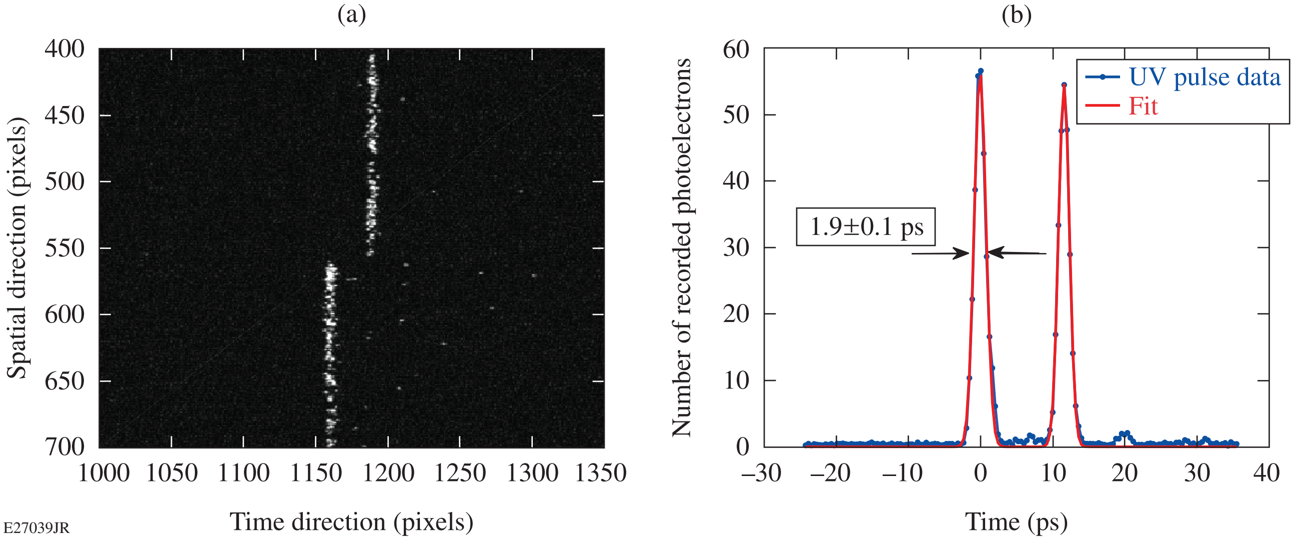

Figure 153.21
(a) Swept image of the split UV pulse on the streak-camera CCD obtained with a subpicosecond pulse split by an etalon of fused silica yielding an 11.2-ps delay between the two pulses; (b) lineout image of (a) and Gaussian fits of the two pulses.

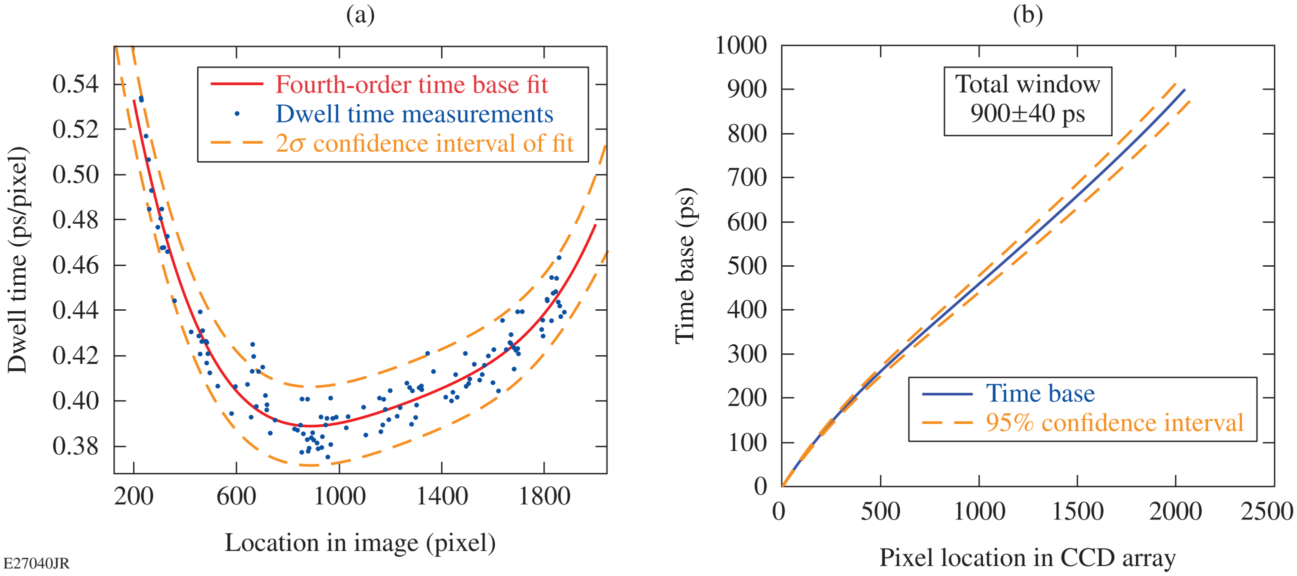

Figure 153.22
(a) The dwell time per pixel as a function of pixel location on the sweep window for the camera using the fast pulser; (b) the camera time base as a function of position on the CCD array.

Table 153.IV: Sweep window measurements.

	Sweep window	Impulse response
Voltage pulser 1	900±40 ps	1.9±0.1 ps
Voltage pulser 2	4.6±0.2 ns	0.01±0.005 ns

Note: Absolute timing is ultimately limited by the jitter in the ramp trigger circuit, which was measured to be <20 ps.

Table 153.IV gives the fitting parameters for the streak-camera sweep rate. The average sweep rates for the two speeds are 0.43 and 2.2 ps/pixel for each sweeping rate, respectively. The fastest portion of the fast sweep has a peak sweep rate of 0.39 ps/pixel. The impulse response of the camera is ~2 ps in this region, measured by fitting the detected subpicosecond pulse. The corresponding full temporal windows were found to be 900 ps and 4.6 ns for the two sweeping speeds.

Focus Optimization

The streak camera's electro-optical imaging system consists of two quadrupole electromagnets that can be adjusted with an internal electronic control. The best focusing of the streak camera was found by varying the voltage on each quadrupole element and measuring the width of the image on the camera for each voltage configuration. The streak camera was equipped with an x-ray–sensitive photocathode of 3000-Å potassium bromide on a 12.5-μm beryllium substrate and illuminated with a large-area, uniform soft x-ray source. The soft x-ray source is a gold bombardment target on a 12.5-μm Be substrate operated in transmission that generates x rays in the 1- to 6-keV range, limited by the transmission of the Be in the low-energy range and the 6-kV electron source at high energy. In the resulting static image, the width of the image of the slit in the swept direction and the contrast of a spatial fiducial bar and space mask in the spatial direction were measured. Figures 153.23(a) and 153.23(b) show contours of each of the fitted parameters as a function of the voltage applied to each electron optic. In the spatial resolution direction, the width is assessed using the following formula:

$$M = \frac{4}{\pi} e^{-2(\pi\sigma\nu)^2},$$

where M is the contrast of a square wave mask with spatial frequency ν and σ is the 1/e width of a gaussian line spread function.[22] In the temporal direction, the width is assessed by finding the full width at half maximum (FWHM) of the line focus. The best-focus voltages are determined through a simultaneous minimization of a merit function that considers equally the temporal and spatial impulse responses. The minimum resolution elements in the spatial and temporal axes are reported in Table 153.V.

Table 153.V: Summary of streak-camera calibration measurements.

	Standard mode	Inverse mode
Temporal resolution (fast sweep)	9 ps	2.1 ps
Magnification (designed)	(0.4×)	(4×)
Spatial resolution at photocathode plane	70 μm	18 μm
Number of spatial resolution elements	>800	>300
Number of temporal resolution elements	~100	400
Dynamic range per resolution element (fast sweep)	225:1	30:1

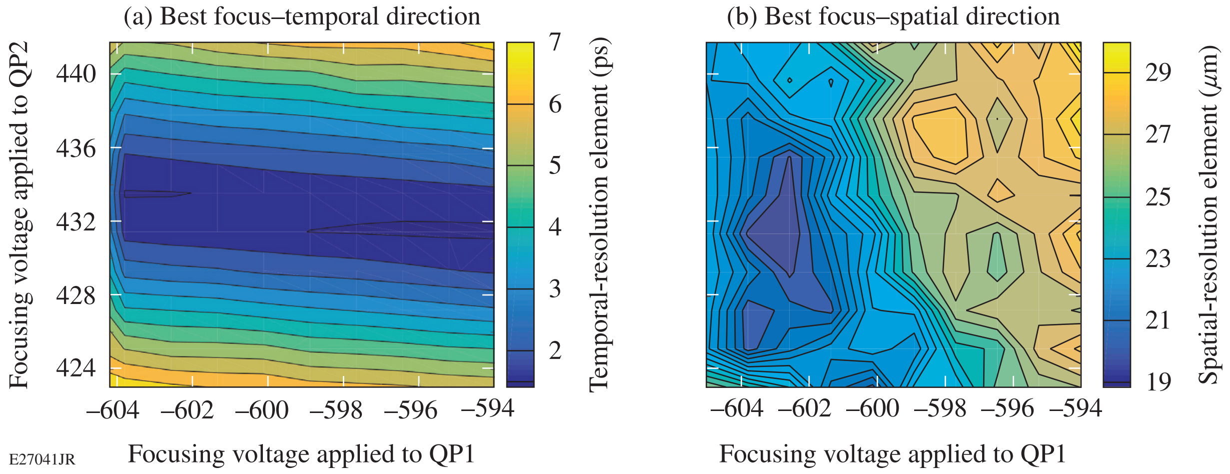

Figure 153.23
(a) The measured width of the detected pulse and (b) spatial resolution element as functions of focusing voltages on each quadrupole.

The focusing voltages with which to best focus the camera are compared against a static particle-tracking code SIMION model of the designed geometry and are found to agree to design predictions by 5%. This discrepancy between the model and experimental results is attributed to the stackup of manufacturing tolerances within the electron optical system.

Gain and Secondary Electron Production

The streak-camera gain and noise figure was also characterized. The streak-camera gain is the enhancement in the number of electrons from the photocathode to the streak camera for a given extraction voltage, phosphor, and image relay system to the detector, typically measured in CCD electrons per accelerated photoelectron. It is essential to accurately measure the system's gain since the photoelectron current is the limiting factor in streak-camera measurements. The noise factor is a multiplicative factor that characterizes the relative increase in variance of the output signal relative to a theoretical noise-free amplification. The raw signal from the streak camera must ultimately be converted to detected photoelectrons, which requires a knowledge of the gain. The statistical variance of the output signal σ_{out}, in CCD electrons, follows from the variance theorem that uncorrelated variances add in quadrature,

$$\frac{\sigma_{\text{out}}^2}{S_{\text{out}}^2} = \frac{\sigma_G^2}{G^2} + \frac{\sigma_{\text{in}}^2}{S_{\text{in}}^2},$$

where S_{out} is the output signal in CCD electrons, G is the signal gain, σ_G is the variance arising from the gain process, S_{in} is the input signal in photoelectrons, and σ_{in} is the input variance. The input signal (arrival of photoelectrons) is naturally Poisson distributed (i.e., $\sigma_{\text{in}}^2 = S_{\text{in}}$) and the mean output signal S_{out} is the input signal times the gain G.

By rearranging, it is apparent that the output variance is increased by a factor F^2 compared to a perfect application of gain (i.e., $\sigma_{\text{out}}^2 = S_{\text{out}}G$):

$$\sigma_{\text{out}}^2 = S_{\text{in}}G^2\left(\frac{S_{\text{in}}\sigma_G^2}{G^2} + 1\right) = S_{\text{out}}GF^2.$$

The method for determining the gain of the streak camera and the secondary electron spectrum of the x-ray photocathode has been laid out in Ref. 23. Here we follow a similar scheme in order to isolate the intrinsic gain of the camera and the number of secondary electrons from the photocathode.

The single photoelectron gain is measured by illuminating a gold-coated parylene-N photocathode with 263-nm laser light. The illumination is kept low so that single-photon–electron events dominate the signal, and the arrival of two photons at the same location at the same time is unlikely. UV illumination on a gold photocathode produces one photoelectron per absorbed photon. The pulse-height distribution of the signal is shown in Fig. 153.24.

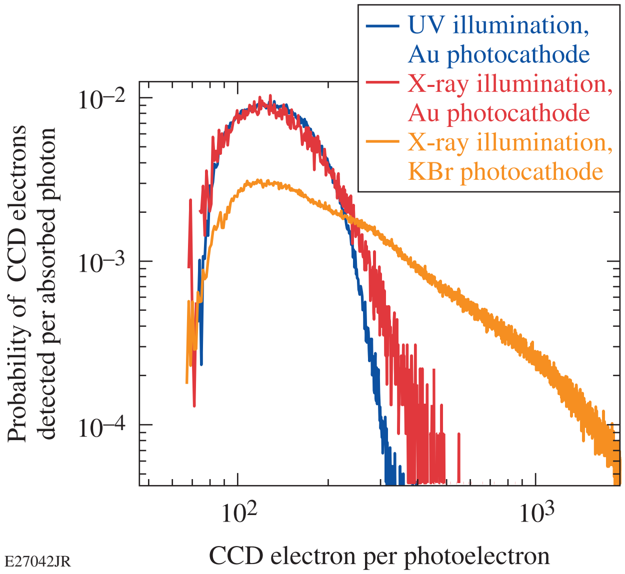

Figure 153.24
Histograms of pulse-height values from illumination with UV and soft x-ray radiation. Generation of multiple electrons per absorbed photon tends to broaden the distribution, leading to a higher gain at the expense of greater noise in the detected signal. The mean values and variance of each of the distributions are given in Table 153.VI.

Table 153.VI: Streak-camera gain.

Material	Gain	σ_G	F^2	Electrons per absorbed photon
263-nm illumination, Au photocathode	131	57	1.19	1.00
X-ray illumination, Au photocathode	167	83	1.25	1.27
X-ray illumination, KBr photocathode	403	380	1.80	2.83

A pulse-height distribution of the sparse photo events is created by binning over a super pixel centered on each event. The super pixel size was determined by collecting and averaging 20,000 single-photon events and characterizing the average size in pixels of the single-photon event. The 1/*e* width of the average single-photon event was found to be 0.56 pixels, indicating that 99.8% of CCD counts are located within a 3 × 3 super pixel of the peak for a single-photon event. The number of ADU's inside the super pixel is counted and recorded in a histogram. The CCD ADU-to-electron conversion was applied to convert the units to electrons.

The pulse-height distribution is constructed in the following manner: The images are corrected for bias and dark current generation with a 200 frame average of dark frames acquired prior to each run. This creates a high signal-to-noise (SNR) dark frame from which to subtract the sparse illuminated image. Individual spurious events arising from the transit of high-energy particles, commonly referred to as cosmic rays in CCD literature, are eliminated from the dark frame through a five-frame median filter of the dark-frame stack. The number of pixels removed as a result of such spurious events is counted; this number is typically 2 to 5 ppm, corresponding to <21 events over the 2048 × 2048 chip in the image.

In a typical x-ray photocathode interaction with an insulator such as potassium bromide, one x-ray photon can generate a multitude of secondary photoelectrons.[11] An x-ray photon has significantly higher energy than the photoelectric work function of the photocathode, so the primary photoelectron emerges with significant kinetic energy. The mean-free path of an electron inside the photocathode is small compared to the thickness of the layer, and the primary electron undergoes a number of collisions before emerging out the other side of the photocathode. By dividing the number of CCD electrons recorded for KBr by the intrinsic gain measured for UV on gold illumination, we find that the KBr photocathode yields 2.8× the number of photoelectrons to the phosphor per absorbed x ray. It is important to note that this measurement was made *in situ* and includes losses in the electro-optical imaging system and the current condition of the photocathode layer.

Space-Charge Broadening

The effect of space-charge broadening is measured by observing the increase in the apparent width of the photoelectron signal from a fixed pulse width as a function of the extracted number of photoelectrons per picosecond. In this evaluation, the streak-camera ramp circuit is synchronized to the laser pulse and the UV laser spot is focused onto the photocathode to provide a locally intense signal. The laser spot was measured to be 100 μm in diameter, which is well suited to the photocathode width in inverse mode (~90 μm). The laser pulse is filtered to the minimum detectable signal (~1 photoelectron per pulse) and progressively increased in intensity while measuring the pulse width from the streak camera.

The measured signal width is plotted against the number of extracted photoelectrons per resolution element in Fig. 153.25. In the inverse mode, the effects of space-charge broadening become apparent near 30 detected photoelectrons per resolution element in the inverse mode, which signals the upper limit to the dynamic range of the camera. The limit imposed is a 20% broadening of the camera's impulse response in each operating mode—the total dynamic range for this event. The camera is capable of detecting single photoelectron events (~130 CCD electrons per event for UV/Au) above the noise floor (13.2 CCD electrons per resolution element) of the CCD's recording system, providing a lower limit of one photoelectron per resolution element in both operating modes.

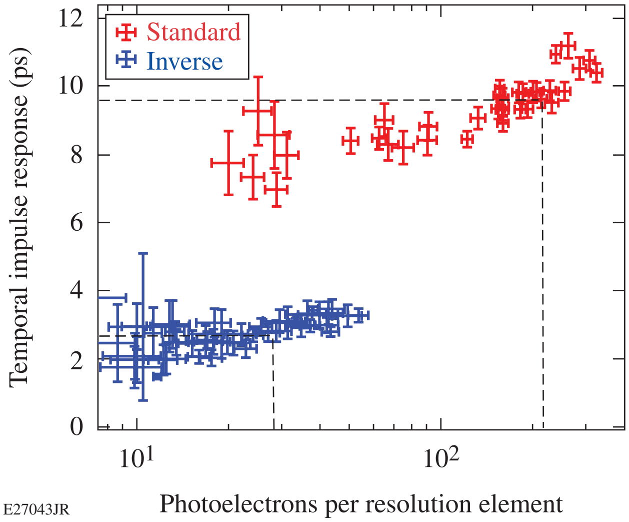

Figure 153.25
Measured FWHM broadening trends for inverse and standard modes as a function of photoelectron number per resolution element. Dashed lines show 20% temporal broadening in the horizontal direction and the recorded signal per resolution element in the vertical direction.

The predominant limiting factor in the streak camera's dynamic range is space-charge broadening. For this camera, the effect is most pronounced at the photocathode, where the electrons have yet to be accelerated and photoelectron current density is the highest. The lower magnification of the standard mode allows a lower current density per resolution element at the photocathode and ultimately a higher dynamic range. When selecting a photocathode material, consideration of space-charge limits depends on the number of photoelectrons per absorbed photon since the space-charge limit is imposed on the amount of accelerated charge, not the number of absorbed photons. In this case, the dynamic range is reduced by the number of secondary electrons emitted by the photocathode.

Conclusion and Operation Recommendations

The PJX-3 x-ray streak camera has been evaluated for experiments in the future. The time base and associated uncertainty were quantified to 5% with a variable-delay subpicosecond laser pulse that was scanned through the sweep window. The intrinsic gain of the camera was measured and used to determine the average value and spread of CCD ADU's per single photoelectron created at the photocathode. The effect of space-charge broadening was characterized and seen to limit the total dynamic range per resolution element. Accurate measurements of time base and photometric gain and added noise are essential to quantifying measurements and associated uncertainty made with the streak camera. A summary of the performance is listed in Table 153.V.

Following from the analysis in this article, it is advised to disperse the signal as much as possible over the streak-camera slit to maximize the useful dynamic range of the system; locally bright features will cause space-charge broadening and distortions, rendering data difficult to reduce from the streak-camera image. In the case of a very large dynamic range in the source (e.g., x-ray satellite lines near a resonance line), it may be advisable to use different photocathode materials for different parts of the spectra to avoid saturating the main peak while maintaining a sufficient signal in the weaker feature.

ACKNOWLEDGEMENT

This material is based upon work supported by the Department of Energy National Nuclear Security Administration under Award Number DE-NA0001944, the University of Rochester, and the New York State Energy Research and Development Authority.

REFERENCES

1. S. P. Regan, J. A. Delettrez, R. Epstein, P. A. Jaanimagi, B. Yaakobi, V. A. Smalyuk, F. J. Marshall, D. D. Meyerhofer, W. Seka, D. A. Haynes, Jr., I. E. Golovkin, and C. F. Hooper, Jr., Phys. Plasmas **9**, 1357 (2002).
2. R. Shepherd *et al*., Rev. Sci. Instrum. **75**, 3765 (2004).
3. E. V. Marley *et al*., Rev. Sci. Instrum. **83**, 10E106 (2012).
4. Y. P. Opachich *et al*., Rev. Sci. Instrum. **83**, 125105 (2012).
5. D. G. Hicks, B. K. Spears, D. G. Braun, R. E. Olson, C. M. Sorce, P. M. Celliers, G. W. Collins, and O. L. Landen, Phys. Plasmas **17**, 102703 (2010).
6. D. G. Hicks, B. K. Spears, D. G. Braun, R. E. Olson, C. M. Sorce, P. M. Celliers, G. W. Collins, and O. L. Landen, Rev. Sci. Instrum. **81**, 10E304 (2010).
7. K. Shigemori *et al*., Rev. Sci Instrum. **83**, 10E529 (2012).
8. O. Ciricosta *et al*., Phys. Rev. Lett. **109**, 065002 (2012).
9. J. Ashkenazy, R. Kipper, and M. Caner, Phys. Rev. A **43**, 5568 (1991).
10. R. S. Marjoribanks, M. C. Richardson, P. A. Jaanimagi, and R. Epstein, Phys. Rev. A **46**, R1747 (1992).
11. B. L. Henke, J. Liesegang, and S. D. Smith, Phys. Rev. B **19**, 3004 (1979).
12. S. T. Ivancic, C. R. Stillman, D. Nelson, I. A. Begishev, C. Mileham, P. M. Nilson, and D. H. Froula, Rev. Sci. Instrum. **87**, 11E538 (2016).
13. C. R. Stillman, P. M. Nilson, S. T. Ivancic, C. Mileham, I. A. Begishev, R. K. Junquist, D. J. Nelson, and D. H. Froula, Rev. Sci. Instrum. **87**, 11E312 (2016).
14. P. M. Nilson, F. Ehrne, C. Mileham, D. Mastrosimone, R. K. Jungquist, C. Taylor, C. R. Stillman, S. T. Ivancic, R. Boni, J. Hassett, D. J. Lonobile, R. W. Kidder, M. J. Shoup, A. A. Solodov, C. Stoeckl, W. Theobald, D. H. Froula, K. W. Hill, L. Gao, M. Bitter, P. Efthimion, and D. D. Meyerhofer, Rev. Sci. Instrum. **87**, 11D504 (2016).
15. O. V. Gotchev, P. A. Jaanimagi, J. P. Knauer, F. J. Marshall, and D. D. Meyerhofer, Rev. Sci. Instrum. **75**, 4063 (2004).
16. P. A. Jaanimagi, R. Boni, D. Butler, S. Ghosh, W. R. Donaldson, and R. L. Keck, Proc. SPIE **5580**, 408 (2005).
17. Kentech Instruments Ltd., Wallingford, Oxfordshire, OX10 8BA, UK.
18. P. A. Jaanimagi, A. Mens, and J.-C. Rebuffie, Proc. SPIE **2549**, 62 (1995).
19. J. R. Janesick, K. P. Klaasen, and T. Elliott, Opt. Eng. **26**, 261072 (1987).
20. V. Bagnoud, J. Puth, I. Begishev, M. Guardalben, J. D. Zuegel, N. Forget, and C. Le Blanc, in *Conference on Lasers and Electro-Optics/Quantum Electronics and Laser Science and Photonic Applications, Systems and Technologies*, Technical Digest (CD) (Optical Society of America, Washington, DC, 2005), Paper JFA1.
21. V. Bagnoud, J. D. Zuegel, N. Forget, and C. Le Blanc, Opt. Express **15**, 5504 (2007).
22. C. Kunz, R. Haensel, and B. Sonntag, J. Opt. Soc. A **58**, 1415 (1968).
23. S. Ghosh, R. Boni, and P. A. Jaanimagi, Rev. Sci. Instrum. **75**, 3956 (2004).

Cross-Beam Energy Transfer: Polarization Effects and Evidence of Saturation

Introduction

Stimulated Brillouin scattering (SBS), one of the most common three-wave laser–plasma instabilities, occurs when an electromagnetic wave "pump" decays into a second frequency-downshifted electromagnetic wave "probe" and an ion-acoustic wave (IAW). The decay is resonant when the following holds:

$$\omega_0 - \omega_1 = \left(\mathbf{k}_0 - \mathbf{k}_1\right) \cdot \mathbf{V} + \left|\mathbf{k}_0 - \mathbf{k}_1\right| c_s, \tag{1}$$

where ω is the frequency; k is the wave number; the subscripts 0 and 1 refer to the pump and probe, respectively; V is the plasma-flow velocity; and c_s is the sound speed. The use of a stationary plasma ($|\mathbf{V}| = 0$) makes clear that the formula satisfies conservation of both energy [$\hbar\omega_0 = \hbar(\omega_1 + \omega_\mathrm{IAW})$, where $\omega_\mathrm{IAW} = k_\mathrm{IAW} c_\mathrm{s}$ is the IAW frequency] and momentum [$\hbar k_0 = \hbar(k_1 + k_\mathrm{IAW})$]. In the absence of a plasma-flow velocity, a frequency difference between the two electromagnetic waves is required such that the resulting beat frequency matches the finite ion-acoustic wave frequency. Another straightforward limit occurs when the plasma-flow velocity projected along the direction of the beat wave is equal to the sound speed; in this moving frame, the electromagnetic wave frequencies are Doppler shifted such that their beat frequency resonantly drives the finite-frequency IAW in the same manner. A combination of flow velocity and frequency-shifted electromagnetic waves can satisfy this formula in a similar manner.

When the instability grows from the thermal density modulations present in any finite-temperature plasma (i.e., noise), it is typically referred to as SBS, and direct backscatter tends to dominate the overall scattered light because the ponderomotive force driving the IAW density modulation is strongest for oppositely directed electromagnetic waves. When the instability is seeded by an electromagnetic wave with an amplitude much larger than that of the thermal noise, as first described by Randall *et al.*,[1] it has come to be referred to as cross-beam energy transfer (CBET). CBET can result in scattered light at a wider range of angles, dictated by the direction of the electromagnetic seed.

In direct-drive inertial confinement fusion (ICF),[2] targets are typically driven symmetrically with frequency-degenerate laser beams. CBET occurs when rays from the outer edge of a given beam refract through the corona and bypass the target without being absorbed. When these rays overlap other incident beams in a location where the target's exhaust velocity renders frequency-degenerate interactions resonant (close to the Mach-1 surface), energy is transferred from the incoming to the outgoing rays, introducing drive asymmetries as well as reducing the laser ablation pressure and capsule drive [Fig. 153.26(a)]. This has been observed on the basis of scattered-light and implosion-velocity measurements.[3–7]

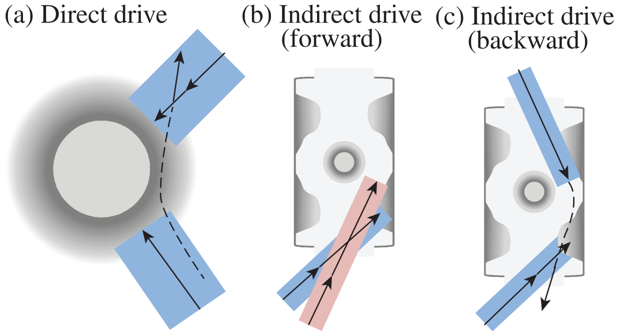

Figure 153.26
Illustrations of ways that cross-beam energy transfer (CBET) can occur in ICF targets, showing just two beams. (a) In direct drive, edge rays from each beam can bypass the target and be amplified by other incident beams in the expanding corona surrounding the capsule. (b) In indirect drive, CBET occurs between incident beams in the laser entrance hole region and is primarily controlled by frequency detuning the lasers. (c) A different type of CBET was recently observed in indirect-drive hohlraums, where it was found that specular reflections could seed CBET in the plasma expanding from the hohlraum wall.

In indirect-drive ICF[8] at the National Ignition Facility (NIF), CBET usually refers to the transfer of energy between the 96 full-energy beams overlapping in each laser entrance hole of a hohlraum target.[9–13] Since the flows in the entrance region are typically much less than the sound speed, CBET is usually controlled by introducing a frequency difference between different cones of incident beams in order to tailor the distribution of laser intensity within the hohlraum interior [Fig. 153.26(b)]. Recently, however, an additional form of CBET was observed in hohlraums: specular reflections and/or backscatter from one cone of beams was shown to be reamplified by a different set of beams [Fig. 153.26(c)], which complicated the understanding and diagnosis of scattered light from such targets.[14] This latter process resembles the direct-drive version of CBET.

In all cases, a proper accounting of CBET is vital for predictive modeling of ICF implosions. In this article, we will first review the model that is used to calculate CBET in indirect-drive experiments on the NIF along with a recent experiment showing excellent agreement with the theory. We will then present additional data in which the incident probe-beam energy was increased in order to access larger IAW amplitudes, which resulted in deviation from linear theory and evidence of IAW saturation. The data indicate that IAW's are saturated at the $\delta n/n \approx 0.015$ level for the laser and plasma parameters of the experiment. Next, we will review the ability to manipulate a probe beam's polarization using CBET, along with an example showing the complexity that arises from such polarization effects in a multibeam configuration such as those typical in ICF research. Finally, we will present our conclusions.

CBET Linear Theory

In this section, the essential features of the model presented by Michel *et al.* (Ref. 15 and references therein) are summarized. The pump and probe are described by normalized laser vector potentials $\mathbf{a} = e\mathbf{A}\big/\left(m_\mathrm{e}c^2\right) \approx 8.55 \times 10^{-10}\left(I\lambda_{\mu\mathrm{m}}^2\right)^{1/2}$, where I is the laser intensity (W/cm^2) and $\lambda_{\mu\mathrm{m}}$ is the laser wavelength in microns. The effect of an electromagnetic pump beam on a probe beam in a plasma can be described by a refractive-index perturbation $\delta\eta$. Interacting with the pump over some length L, a component (specified later) of the probe laser is modified by the operator $\exp(ik_1\delta\eta L/\eta_0)$, where $\eta_0 = \sqrt{1 - n_\mathrm{e}\big/n_\mathrm{c}}$ is the unperturbed plasma's refractive index, given electron density n_e and critical density n_c. Using a kinetic model, the refractive-index perturbation is given by

$$\delta\eta = (1/2)K^*\left|\pi_0\right|^2 \sin\left(\psi/2\right)\tan\left(\psi/2\right),$$

where $K = \chi_\mathrm{e}\left(1+\chi_\mathrm{i}\right)\big/\left(1+\chi_\mathrm{e}+\chi_\mathrm{i}\right)$; the electron and ion ($\alpha$ = e,i) susceptibilities in thermodynamic equilibrium are $\chi_\alpha = -(1/2)\left(k_\mathrm{b}\lambda_{\mathrm{D}_\alpha}\right)^{-2} Z'\left[v_\mathrm{b}\big/\left(\sqrt{2}\,v_{T_\alpha}\right)\right]$; $\mathbf{k}_\mathrm{b} = \mathbf{k}_0 - \mathbf{k}_1$ is the beat wave's wave number; $\lambda_{\mathrm{D}_\alpha} = v_{T_\alpha}\big/\omega_{P_\alpha}$ is the Debye length; $v_{T_\alpha} = \left(T_\alpha/m_\alpha\right)^{1/2}$ is each particle's thermal velocity with T_α and m_α its temperature and mass; $\omega_{P_\alpha} = \left(4\pi n_\alpha q_\alpha^2\big/m_\alpha\right)^{1/2}$ gives the electron and ion plasma frequencies; Z is the plasma dispersion function; $v_\mathrm{b} = \omega_\mathrm{b}\big/k_\mathrm{b}$ is the beat wave's phase velocity; $\omega_\mathrm{b} = \omega_0 - \omega_1$ is the beat wave's frequency; and $\left|\boldsymbol{\pi}_0\right|^2 = \left|\mathbf{a}_{0_p}\right|^2\cos^2\psi + \left|\mathbf{a}_{0_s}\right|^2$ is the pump amplitude projected into the plane of the probe's polarization, where the p component is in the plane defined by the pump and probe **k** vectors and the s component is orthogonal to that plane, and ψ is the crossing angle between the two beams.

The model assumes the following: The interaction has reached steady state, which occurs on ion-acoustic time scales; the spatial variations of the ion-acoustic wave are assumed small compared to the beat wave's wavelength; and the variations of the pump and probe envelopes along the interaction bisector are small compared to the laser wavelength.

It is crucial to note two key features of the model in order to understand polarization effects in CBET as well as the experimental results that will be presented: The first key point is that, for arbitrary polarizations, the interaction is generally anisotropic—only the component of the probe's polarization that is parallel to π_0 is affected by the pump–plasma system (i.e., modified by the operator given above); any orthogonal probe polarization component is unaffected by the system [Fig. 153.27(a)].

The second key point is that $\delta\eta$ is complex. The imaginary component is typically assumed to govern CBET because it modifies the amplitude of the probe beam and peaks at the ion-acoustic resonance, as expected. The fact that there is an associated real component—directly related to the imaginary component by the Kramers–Kronig relations—is true of many systems with frequency-dependent optical resonances (e.g., electric susceptibility, magnetic susceptibility, electrical conductivity, and thermal conductivity) and widely applicable in all areas of physics. A modification of the plasma's real refractive index (only in the direction of the pump polarization) implies that the probe encounters birefringence. Since the real component describes the out-of-phase response of the system, it can be nonzero even for cases in which the imaginary component disappears and CBET may be assumed to be negligible. An example will be provided later to show how this real component could dramatically alter CBET in a multibeam interaction. The solid curves shown in Fig. 153.27(b) are an example of the real and imaginary components calculated with this model for the parameters of an experiment to be discussed in the next section.

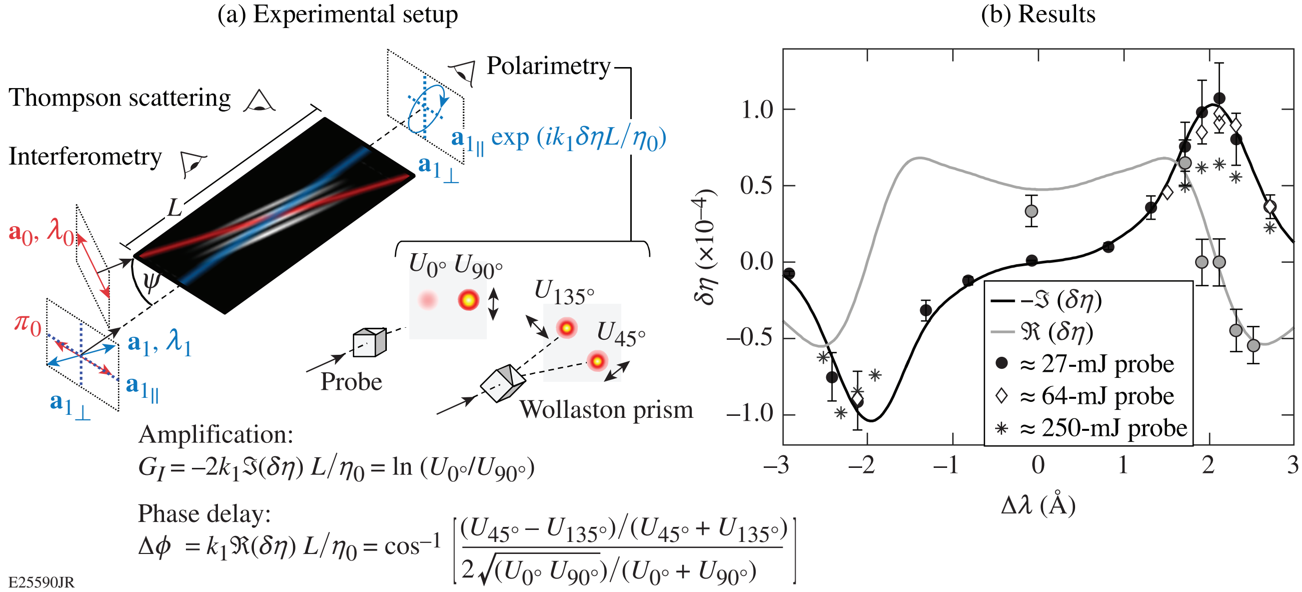

Figure 153.27
Refractive index of a pump–plasma system. (a) An experiment was conducted in which a weak probe beam, with polarization oriented at 45°, interacted with a horizontally polarized pump. Only the probe's horizontal component sees the refractive-index perturbation induced by the pump–plasma system. The probe polarization subsequent to the interaction is used to infer the magnitude of the refractive-index perturbation. (b) Linear theory calculations are plotted with three sets of data points for parameters listed in Table 153.VII. There is good agreement for the weaker injected probe beams, but clear deviation at the highest probe energy, indicating nonlinearity.

Experimental Results

1. Setup

Several experiments were conducted recently at Lawrence Livermore National Laboratory's Jupiter Laser Facility using the Janus laser. Many of the results have been presented in prior publications.[16,17] A long (≈3-ns square), high-intensity pump pulse was focused onto a gas jet equipped with a 3-mm-diam outlet emitting methane gas. A phase plate was used to give the pump beam a flattop but speckled 600-μm-diam focal spot. The pump energy for the shots shown in Fig. 153.27(b) was 292±8 J, giving an expected average intensity of $I = (3.6\pm0.2)\times10^{13}$ W/cm^2 at the time of the interaction. The peak of an ≈250-ps Gaussian probe beam was timed to arrive ≈1.3 ns after the rising edge of the pump. It was focused using a 200-μm-diam phase plate and crossed the pump at an angle of 27° away from co-propagation.

To measure the refractive index perturbation induced by the pump–plasma system, the pump polarization was horizontal (*p* polarized), whereas the probe polarization was oriented at 45° using a polarizer. This meant there were nearly equal probe polarization components interacting and not interacting with the pump. Separating the probe polarization into constituent components along the *s*- and *p*-polarization directions relative to the two-beam interaction, as well as 45° relative to those axes, provides a measurement of both the probe amplification (i.e., energy transfer) and any phase delay induced by the real refractive-index component. The polarimetry diagnostic and the formulas for extracting these values from the data are shown in Fig. 153.27(a). For a gain measurement only, it is sufficient to make a single measurement of the *s*- and *p*-polarization components. Conversely, for pure phase delays and no energy transfer (in the case of frequency-degenerate beams), it is sufficient to make a single measurement along the axes rotated 45°.

Both beams used the first harmonic of an Nd:YLF laser source ($\lambda \approx 1053$ nm), but independent front ends allowed us to measure CBET as a function of wavelength detuning between the two beams (here, a range of $-3 \le \Delta\lambda \le 3$ Å was used).

Plasma density and electron temperature were measured with Thomson scattering and interferometry. The Thomson-scattering diagnostic collected scattered light from the pump beam in a 90° (vertical) geometry relative to the pump propagation. The blue-shifted electron plasma wave feature was recorded on a streak camera with an S1 photocathode, set to a 5-ns sweep speed. An example of the data is shown in Fig. 153.28(a). Since a high-density, low-Mach-number nozzle was used in conjunction with the large-diameter pump beam, the diagnostic collected light from a volume spanning 600 μm in the vertical direction, encompassing a wide range of densities. It was necessary to include a range of electron densities spanning ≈(1 to 1.4) × 10^{19} cm^{-3} to fit the Thomson data at the time of interaction [shown as the dashed line in Fig. 153.28(a) relative to the Thomson data as well as the pump pulse shape as recorded on a fast diode and oscilloscope] on each shot.

The interferometry data, which used an ultrashort Ti:sapphire beam incident on the channel perpendicular to the pump beam and imaged onto a charge-coupled–device camera using a Nomarski configuration, further constrained the density throughout the interaction. An example of the chord-integrated density–length product is shown in Fig. 153.28(b). It showed that the highest densities in the Thomson volume were actually below the center of the two-beam interaction (≈1.5 mm above the nozzle, which is visible at $y = 0$ mm in the image). Furthermore, the density decreased on either side along the ≈1.2-mm interaction length such that the path-integrated density was ≈88% of the peak density measured by Thomson scattering. These considerations were factored into the parameters listed in the Table 153.VII.

Table 153.VII: Plasma parameters.

Parameter	Theory input	Measured value	*HYDRA* simulation
n_e/n_c	0.0104	0.11±0.001	0.009
T_e (eV)	220	224±4	≈231
T_i/T_e	0.115	–	≈0.09
V_{flow} (m/s)	1.4 × 10^4	–	≈1.4 × 10^4
I_0 (W/cm^2)	≈3.2 × 10^{13}	≈(3.6±0.2) × 10^{13}	≈3.6 × 10^{13}
$\overline{Z}$	2.5	–	2.0

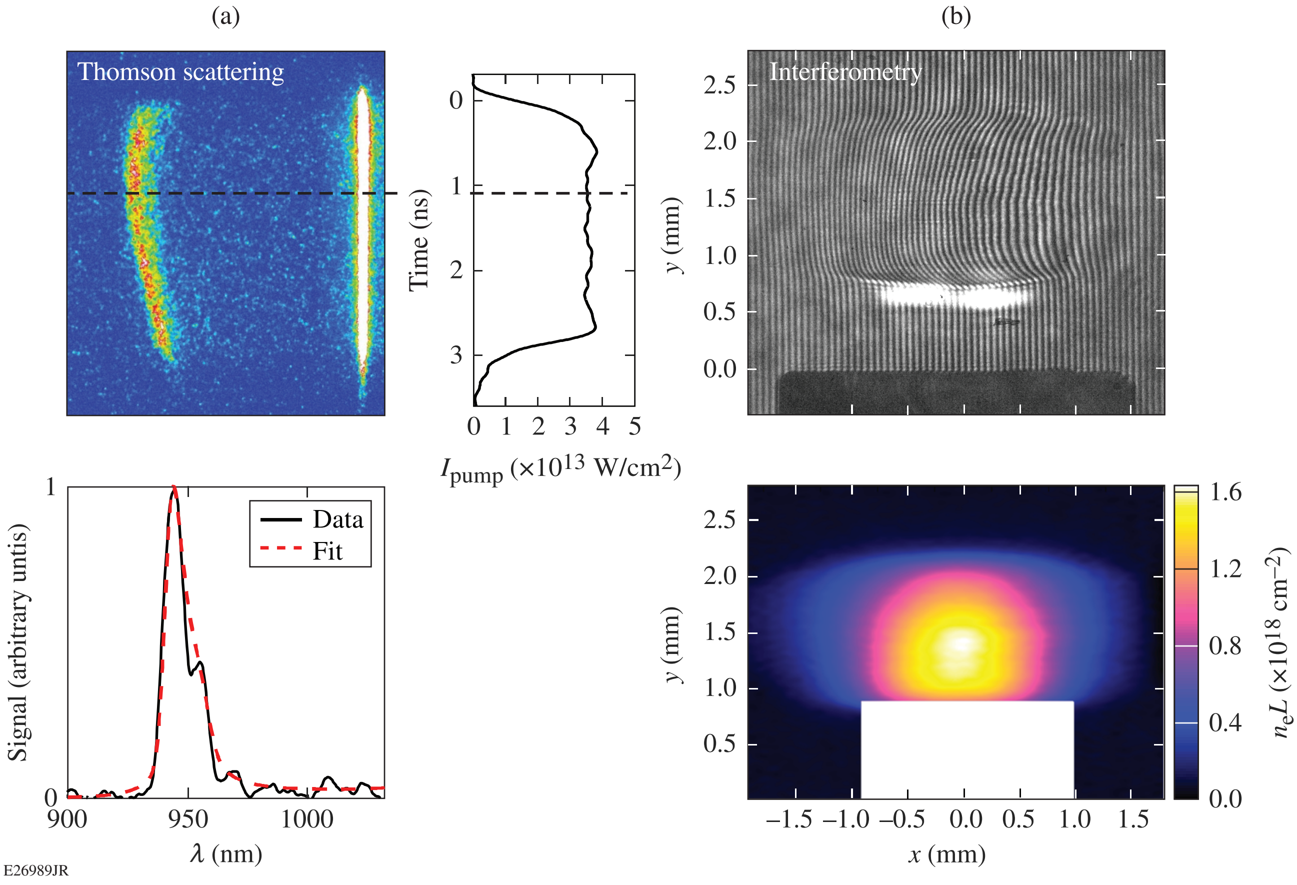

Figure 153.28
Diagnostics for density and electron temperature. (a) The blue-shifted electron feature was collected at 90° and recorded on an S1 streak camera using a 5-ns sweep. It was analyzed at the time of the probe interaction, shown as a dashed line relative to the pump pulse shape, recorded on a fast diode/oscilloscope. (b) A Nomarski interferometer used an ultrashort Ti:sapphire diagnostic beam—incident perpendicular to the channel and co-timed with the probe—to measure density gradients in the Thomson volume and along the length of the pump–probe interaction.

While this platform aimed to isolate CBET from hydrodynamic uncertainties, nevertheless a flow velocity resulted from the cylindrical plasma channel expansion following formation by the pump beam. Varying the interferometry beam timing relative to channel formation clearly showed this expansion; it is also the reason why the channels were so much larger than the pump beam's diameter at the time of the interaction [Fig. 153.28(b)]. By Doppler shifting the ion-acoustic wave by different amounts in different portions of the crossing volume, this flow effectively broadened the resonant peak. Flow velocity and ion temperature (not measured) were imported to the linear theory calculation from a 3-D simulation of the experiment using the radiation–hydrodynamic code *HYDRA*.[18]

2. Results

Experimental results for three different data sets were shown in Fig. 153.27(b). The most-extensive data set (already published in Ref. 17) used an incident probe beam with 27 mJ of energy. For that data set, several shots were repeated with the Wollaston prism in the polarimetry diagnostic rotated 45° to measure the real refractive index perturbation component in addition to the amplification. Agreement with linear theory was found to be excellent for both the real and imaginary components.

While most of the parameters used in the linear theory calculation were consistent with experimental measurements and the *HYDRA* simulation, the average ion charge state was an exception. To match the resonant peak location, the plasma was assumed to consist of 30% carbon, rather than the 20%, which might be expected when using methane gas. In Ref. 17, it was conjectured that this might have resulted from ion species separation in the expanding plasma channel. Recent efforts to confirm this experimentally, using simultaneous ion and electron feature Thomson scattering and a gas-jet mixture of hydrogen and argon, failed to observe the predicted effect. It is perhaps more likely that the discrepancy arises from a simple error in measuring the two laser wavelengths. When measured, they were found to differ from the nominal laser wavelengths; a correction was applied, but this correction shifted the experimental data away from the linear theory. Better agreement would be obtained by assuming that the correction should have been made in the opposite direction. Figure 153.27(b), however, retains the possibly incorrect wavelength axis for the data and the slightly higher carbon concentration. Note also that accounting for a factor of $\cos(\psi)$ that was missing in the calculations of Ref. 17 better reconciles the pump intensity used in the linear theory calculation here with that expected from measurements, as shown in Table 153.VII.

Here we present additional amplification data in which the incident probe energy was increased to ≈64 mJ and ≈250 mJ. These additional data sets lack error bars for simplicity, but they are comparable to those on the low-energy imaginary component data. The average incident probe intensities were $I \approx (3.4, 8.1, 32) \times 10^{11}$ W/cm^2, approximately half of which gets amplified by CBET because of the 45° probe polarization. The fact that the data points deviate from the linear theory calculation, especially on the positive wavelength shift side of the wavelength tuning curve, is a clear indication of nonlinearity.

3. Discussion

The most-straightforward explanation for nonlinearity is pump depletion, where the energy transfer significantly impacts the pump amplitude and leads to reduced gain. The maximum gain for the highest energy data, however, was $G_I = 1.27$ such that the output average probe intensity was $I = 1/2\, I_{\text{init}} \exp(1.27) \approx 5.3 \times 10^{12}$ W/cm^2, which is only ≈16% of the pump intensity. Therefore, pump depletion cannot explain the much-reduced gain.

Saturation of ion-acoustic wave amplitudes could also explain the deviation from linearity as well as the fact that it is more prominent for positive wavelength shifts. Figure 153.29(a) shows the expected average IAW amplitude, $\delta n/n = -(1/2)\, K k_b^2 c^2 \omega_{\text{pe}}^{-2} \mathbf{a}_0 \cdot \mathbf{a}_1^*$, as a function of distance interacting with the pump beam when the probe was red shifted to the point of maximum gain for each of the three incident probe energies. In the limit of negligible pump depletion, the IAW amplitude is linear with $\mathbf{a}_1$ such that the amplifying seed drives larger waves. In the case of a 27-mJ injected probe beam, the average IAW amplitude is expected to have been ≈0.004 at the beginning of the interaction region, growing to ≈0.01 by the end of the interaction region. For a 250-mJ incident probe, IAW amplitudes would be expected to span ≈0.012 to 0.032 if the linear theory remained valid. The deviation from linear theory suggests, however, that these larger amplitudes were not accessed. An additional curve is shown for the equivalent trajectory on the opposite side of the wavelength-tuning curve (maximum probe extinction). In this case, IAW amplitudes get smaller with the probe intensity; therefore, nonlinearity is expected to be much less evident.

The effect of speckles must also be taken into account. As discussed in Ref. 19, the intensity distribution present in any speckled beam results in a distribution of beat-wave amplitudes between two speckled beams. The probability function for the local intensity of a speckled laser beam is $P(u) = e^{-u}$ (Ref. 20), where $u = I/\langle I \rangle$ is the local intensity divided by the average.

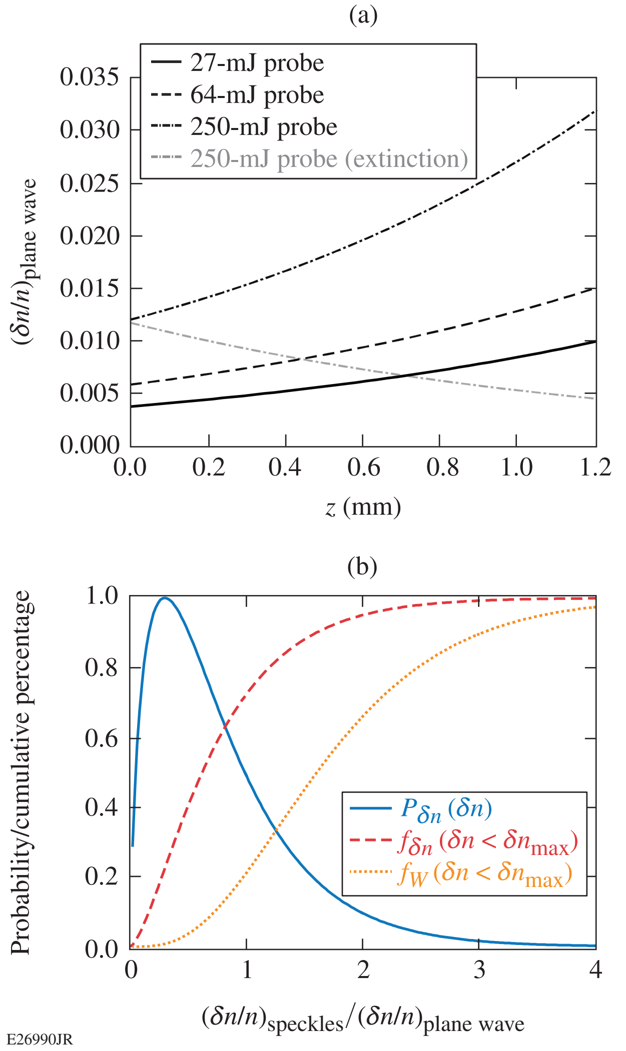

Figure 153.29
Expected ion-acoustic wave (IAW) amplitudes. (a) Average IAW amplitudes were calculated for each of the data sets shown in Fig. 153.27(b), if linear theory remained valid. They increased over the probe propagation length if the probe was amplified and decreased if the probe was extinguished. (b) The use of speckled beams creates a distribution of IAW amplitudes, and most of the energy transfer is mediated by IAW's that are larger than the expected plane-wave value; consequently, IAW saturation will impact CBET between speckled beams at lower average intensities than CBET between plane-wave beams.

The local energy exchange between two beams is proportional to the intensity product $\Delta W \propto I_0 I_1$. If correlations between the speckle patterns of the two beams can be neglected over the length of the CBET interaction region, the probability distribution for energy exchange is given by the product distribution for the random variables I_0 and I_1,

$$P_W(\Delta W) = \int_0^\infty P(u_1)\,P\left(\Delta W/u_1\right)\frac{1}{u_1}\,\mathrm{d}u_1 = 2K_0\left(2\sqrt{\Delta W}\right),$$

where $K_\nu(x)$ is the modified Bessel function of the second kind of order ν. Similarly, the density perturbation is proportional to the square root of the intensity product $\delta n \propto \sqrt{I_0 I_1}$. Since a single beam's probability distribution for the square root of intensity is $P_{\text{sr}}(u) = 2ue^{-u^2}$, that of the product is

$$P_{\delta n}(\delta n) = 4\int_0^\infty \frac{\delta n}{u}\,e^{-\left(u^2 + \delta n^2/u^2\right)}\mathrm{d}u = 4\delta n K_0(2\delta n).$$

Here, the plasma wave amplitude is effectively normalized to the amplitude that would be expected for plane waves having the same average intensity, $\delta n = (\delta n/n)_{\text{speckle}}/(\delta n/n)_{\text{plane wave}}$. The fraction of laser energy exchanged in regions where the local exchange is less than some $\Delta W_{\max}$ is

$$f_W(\Delta W_{\max}) = \frac{\langle \Delta W\rangle_{\Delta W < \Delta W_{\max}}}{\langle \Delta W\rangle}$$

$$= \frac{\int_0^{\Delta W_{\max}} \Delta W P_W(\Delta W)\mathrm{d}\Delta W}{\int_0^\infty \Delta W P_W(\Delta W)\mathrm{d}\Delta W}$$

$$= 1 - 2\Delta W_{\max} K_0\left(2\sqrt{\Delta W_{\max}}\right)$$

$$- 2\sqrt{\Delta W_{\max}}\left(1 + \Delta W_{\max}\right)K_1\left(2\sqrt{\Delta W_{\max}}\right). \quad (2)$$

The fraction of laser energy can also be written in terms of the maximum density perturbation because $\sqrt{\Delta W_{\max}} \propto \delta n_{\max}$:

$$f_W(\delta n_{\max}) = 1 - 2\delta n_{\max}^2 K_0(2\delta n_{\max})$$

$$- 2\delta n_{\max}\left(1 + \delta n_{\max}^2\right)K_1(2\delta n_{\max}). \quad (3)$$

The results of this analysis are plotted in Fig. 153.29(b). The probability distribution of the IAW amplitudes (normalized to the amplitude of the plane-wave case) is shown along with its cumulative sum. This shows that, e.g., ≈70% of the IAW's have an amplitude less than the average plane-wave case, whereas ≈30% have an amplitude larger than the plane-wave case and ≈5% of the IAW's are more than a factor of 2 larger than the plane-wave case. The cumulative fraction of energy transferred by IAW's less than a certain amplitude is also shown, making it clear that a disproportionate amount of energy transfer occurs in the relatively small number of intense interactions (e.g., >30% of the energy is tranferred by IAW's with amplitudes at least 2× larger than the expected plane-wave value). Therefore, nonlinearity will impact speckled beams earlier than plane-wave beams when IAW amplitudes are near the saturation threshold.

Examining the data shown in Fig. 153.26(b) more closely, along with the trajectories shown in Fig. 153.29(a), suggests that IAW amplitudes may be clamped at the $\delta n/n \approx 1\%$ to 2% level. The modest reduction in gain at the IAW resonance peak for the 64-mJ injected probe could be explained by saturation in IAW's driven by the highest-intensity speckles late in the interaction. Furthermore, even average-amplitude IAW's were expected to exceed such a level for the 250-mJ data; therefore, the clamp would impact that data more severely.

To confirm this analysis, CBET simulations were performed using the numerical code *VAMPIRE*.[21] *VAMPIRE* is a fully 3-D propagation model that solves the coupled-mode equations for CBET in steady state, using linear kinetic theory for the IAW response. Laser-intensity distributions in plasma are computed from the position of stochastically distributed geometrical optics rays using a modified tesselation-based estimator. The model reproduces intensity distributions of phase-plate–smoothed beams down to speckle radii of approximately twice the real speckle radius. It also accounts for laser refraction, the finite *f* number of interacting beams, inverse Bremsstrahlung absorption, and CBET per polarization component (although the real refractive index component is neglected). The negligible effect of pump depletion was confirmed by observing no significant difference between simulations that did or did not include pump depletion.

Results from simulations that clamped IAW amplitudes at $\delta n/n = 1.5\%$ are compared to the data in Fig. 153.30. Note that the wavelength axis for the data has been shifted to account for the possible errors discussed above, which facilitates a comparison of the peak gain in both data and simulations. The simulations matched all of the data quite well, with the clamp having no effect for the lowest-energy incident probe, a marginal effect for the mid-level case, and a dramatic effect on the highest-energy incident beam, especially on the positive wavelength shift side (probe amplification), as expected. The fact that such a large amount of data, with fairly different conditions in each case, was fit very well with a single clamp makes a compelling case that the clamp is a realistic way of accounting for the IAW saturation.

Previous attempts to explain IAW saturation have invoked frequency detuning because of kinetic nonlinear frequency shifts associated with trapped ions,[10,22] increased Landau damping and/or frequency detuning cause by ion heating,[23,24] nonlinear damping associated with mode coupling to higher harmonics,[25–27] and the two-ion-wave decay instability.[28–30] The possible influence of these effects will be considered in turn.

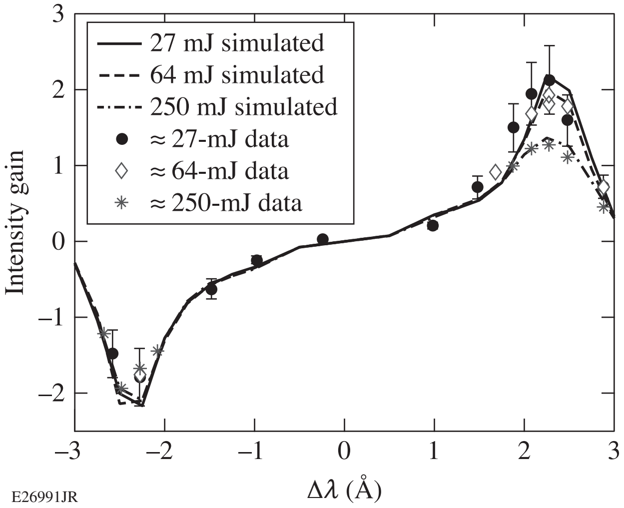

Figure 153.30
The experimental data were compared to simulations using *VAMPIRE*. Including an IAW clamp of $\delta n/n = 1.5\%$ yielded good agreement with all data sets, suggesting IAW's were saturated at that level.

Frequency detuning from a kinetic nonlinear frequency shift does not seem to be a plausible explanation for the saturation observed in this experiment. The magnitude of the expected shift for the IAW amplitudes in question is expected to be quite small, especially when including the contribution of trapped electrons as well as trapped ions.[31] The expected frequency shifts are unlikely to compete with the broad resonance observed in this experiment because of the ion Landau damping provided by hydrogen ions.[32]

Similarly, the already high ion Landau damping makes the interaction relatively insensitive to ion temperature such that ion heating should not substantially alter the gain. Also, if ion heating caused a shift in the resonance peak location, it would have resulted in higher gain at larger frequency shifts between the pump and probe, which was not observed.

The body of work on nonlinear damping associated with mode coupling is primarily concerned with understanding the interplay between various instabilities. If another instability drives a different IAW in the same volume of plasma, it could interfere with the primary wave mediating CBET. However, this two-beam configuration limits the number of plasma waves that are driven in the plasma, and to our knowledge no other plasma waves should be present. The pump remains the most energetic and intense beam in the plasma, so there is no reason additional instabilities should be driven by increasing the seed energy, unless they arise from decay of the primary IAW associated with CBET.

Historically, the low apparent threshold for ion-wave saturation observed in this experiment would have ruled out the two-ion-wave decay instability according to fluid theory, which says that the threshold should be proportional to the daughter waves' damping rates, $\delta n/n_{\mathrm{thr}} > 4\left(\nu_{\mathrm{IAW},1}\nu_{\mathrm{IAW},2}/\omega^2_{\mathrm{IAW},0}\right)^{1/2}$ (Ref. 30). It was recently noted, however, that ions trapped by the primary wave can reduce the linear Landau damping rate for both the primary wave and the daughter waves since they have similar phase velocities.[33] In that work, Chapman *et al.* found, using $2D + 2V$ Vlasov simulations, that the two-ion-wave decay threshold was exceeded for IAW amplitudes of $\delta n/n_{\mathrm{thr}} = 0.011$ for a set of parameters for which previous estimates would have suggested a threshold of $\delta n/n_{\mathrm{thr}} = 0.04$ to 0.09. The authors also discussed a similar decay instability that they referred to as the "off-axis instability," which was accessible because of the multidimensional nature of the simulation. No threshold was identified for this transverse instability. These instabilities could plausibly explain the IAW saturation that we observed in the experiment.

Earlier work by Kirkwood *et al.* also employed frequency detuning in a quasi-stationary plasma to measure CBET.[34] Although it was noted that gain stayed constant with increasing probe intensities, suggesting that IAW's remained linear up to an amplitude of ≈1%, a seemingly conflicting statement was made that the linear gain calculation was off by 20×. Recently, this work was revisited and the results appeared to be much more consistent with linear theory.[35] More-recent efforts to use CBET to generate a high fluence beam reached similar conclusions as to the linearity of low-amplitude IAW's.[36]

Polarization Effects

As outlined in Ref. 15 and demonstrated in Refs. 16 and 17, CBET is very sensitive to the polarization of the interacting beams and can, in turn, strongly modify each beam's polarization. The data for the 27-mJ probe amplification at the positive and negative ion-acoustic resonance peaks are shown in Fig. 153.31(a). When

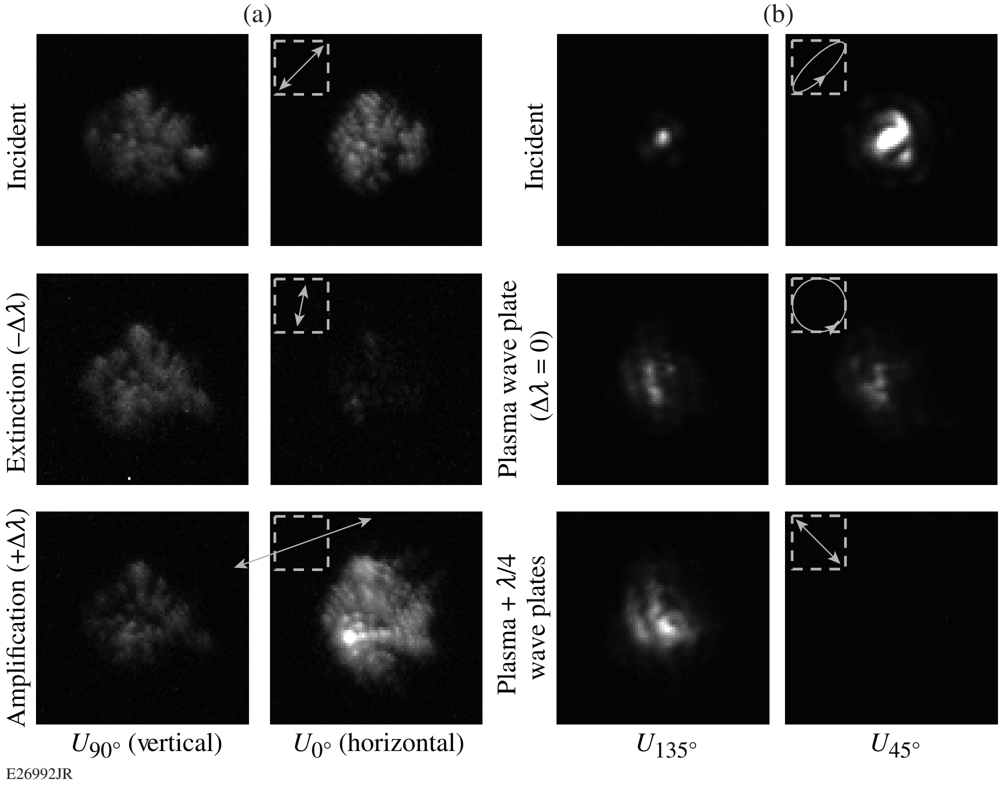

Figure 153.31
Polarization manipulation caused by CBET. (a) Resonant energy transfer at the negative (positive) peak of the ion-acoustic wave extinguished (amplified) the probe and made the probe polarization more orthogonal (parallel) to the pump polarization. (b) Nonresonant interactions were used to convert an elliptically polarized incident probe into a nearly ideal circularly polarized beam without any energy transfer, which was verified by using an additional quarter-wave plate to restore a linear polarization.

the probe is blue shifted relative to the pump, its horizontal polarization is extinguished such that the pump–plasma system acts like a polarizer that passes only the vertical polarization (middle row).[17] This effectively "rotates" the probe polarization, which becomes more orthogonal to the pump as the extinction increases. Conversely, the probe rotates into alignment with the pump when it is red shifted and amplified (bottom row).

Data from a different experiment are reproduced in Fig. 153.31(b). While the setup of that experiment was very similar, one difference was that no phase plate was used in focusing the probe (which is evident in the different focal-spot distribution). The pump and plasma parameters were also different, as well as the incident probe polarization, which was elliptical with a phase delay of ≈38° between the horizontal and vertical components. Wavelength tuning was not employed in that experiment, but the pump intensity and plasma density were adjusted to control the birefringence resulting from the nonzero real refractive-index modulation. After tuning the pump–plasma system to add a phase delay of ≈52°, the probe became nearly ideally circularly polarized (middle row). The fact that the probe was circular (rather than unpolarized, e.g.) was confirmed by repeating the shot with an additional quartz quarter-wave plate in the diagnostic to add another 90° phase delay and recover a linear polarization (bottom row).[16]

These examples illustrate how a pump–plasma system can be used to give a probe beam any arbitrary polarization through amplitude and/or phase changes. Such polarization effects can become particularly complex when considering an environment containing multiple beams in which each beam serves as both pump and probe relative to all other beams present. An example is provided in Fig. 153.32, where each subfigure has curves showing the total normalized vector potential, as well as the s and p components, for each of the three beams. In this calculation, up to three beams intersect in the same plane such that the crossing angle is 27° between Beamlines 1 and 2 as well as Beamlines 2 and 3, but 54° between Beamlines 1 and 3. Relative to the intersection plane, Beamline 1 is s polarized, Beamline 2 is p polarized, and Beamline 3 is 10° away from becoming p polarized. Beamline 1 has a wavelength of λ = 1053 nm, whereas λ = 1053.285 nm for Beamlines 2 and 3. All three beam intensities are $I = 5 \times 10^{13}$ W/cm^2, and they interact over a distance of 4 mm in a fully ionized helium plasma with $n_e = 5 \times 10^{19}$ cm^{-3}, T_e = 200 eV, and $T_i/T_e = 0.1$.

Figure 153.32(a) shows that nothing happens when only Beamlines 1 and 2 are present because their polarizations are orthogonal. Figure 153.32(b) shows a similar case in which only Beamlines 2 and 3 are present. Although their polarizations are nearly aligned, their frequencies are also the same, so there is no energy transfer. They do, however, induce ellipticity in one another as a result of the nonzero real refractive index modulation and their slightly misaligned polarizations. These first two cases describe situations in which the two beams would typically be considered "noninteracting."

Figure 153.32(c) shows that when Beamlines 1 and 3 are present, there is polarization rotation resulting from induced phase delay as well as energy transfer caused by the imaginary component of the refractive-index perturbation. Essentially, the beams transfer energy until they reach a state in which the remaining polarizations are orthogonal. The fact that Beamline 3 (1) is amplified (extinguished) is only modestly due to the fact that the polarizations are nearly orthogonal at the outset.

Now consider the case when all three beams are present [Fig. 153.32(d)]. Initially, only a small fraction of Beamline 1 is transferred to Beamline 3 as in case (c), but by inducing a phase

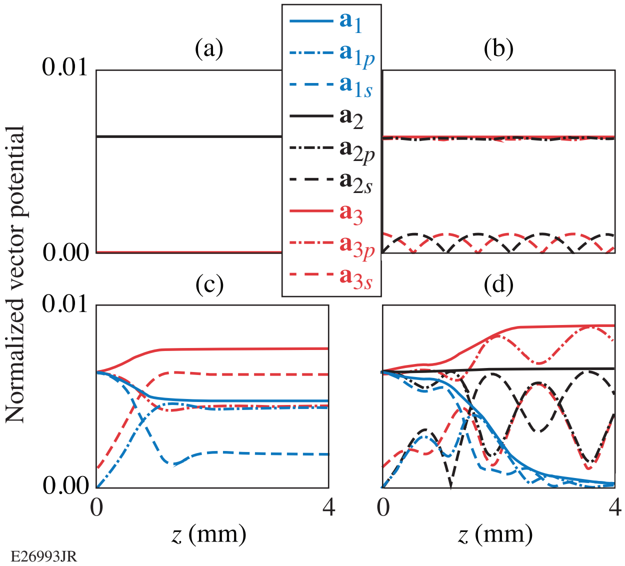

E26993JR

Figure 153.32
CBET between up to three beams for beam/plasma parameters listed in the text. (a) Beamlines 1 and 2 alone see no interaction due to their orthogonal polarizations. (b) Beamlines 2 and 3 alone induce ellipticity in one another but no energy transfer because they are off-resonant (frequency degenerate). (c) Beamlines 1 and 3 alone exchange a modest amount of energy because they have different frequencies and a small shared polarization component, but energy transfer saturates when the polarizations become orthogonal. (d) When all three beams interact, there is a much more dramatic reduction of Beamline 1 and associated amplification of Beamline 3, which results from Beamline 2 acting as a mediator that rotates the Beamline 1 polarization and thereby funnels more energy into a resonant interaction with Beamline 3.

delay in Beamline 1, Beamline 2 acts as a mediator that funnels more energy into a resonant interaction with Beamline 3. This leads to a much more dramatic extinction of Beamline 1 and associated amplification of Beamline 3; all the while the amplitude of Beamline 2 remains approximately constant. This illustrates that polarization effects can have a dramatic influence on CBET in a multibeam configuration, and that even off-resonant interactions can have a large impact on resonant energy transfer.

Conclusions

Various forms of cross-beam energy transfer occur in both direct- and indirect-drive ICF, so a proper accounting of CBET is necessary to accurately model ICF implosions. Recent pump–probe experiments in a quasi-stationary plasma using wavelength tuning to control CBET have been performed to validate the linear theory calculations that are used. These experiments have shown that linear theory appears to be valid for an isolated two-beam interaction with IAW amplitudes up to $\delta n/n \approx 1.5\%$ (which are larger than those expected in ICF experiments[23]), but IAW saturation seems to occur beyond this level. The saturation appears to be consistent with recent work using $2D + 2V$ Vlasov simulations to investigate the two-ion-wave decay instability.[33] Polarization effects of CBET were also reviewed in detail, and it was shown that polarization can have surprising consequences in a multibeam configuration.

ACKNOWLEDGMENT

This material is based upon work supported by the Department of Energy National Nuclear Security Administration under Award Number DE-NA0001944, the University of Rochester, and the New York State Energy Research and Development Authority. This work was performed under the auspices of the U.S. Department of Energy by Lawrence Livermore National Laboratory under Contract No. DE-AC52-07NA27344. Furthermore, it was supported by the LLNL-LDRD Program under Project No. 42074. In addition, we acknowledge EPSRC Grant No. EP/K504178/1 and No. EP/L000644/1. Finally, thanks to the staff of the Jupiter Laser Facility at Lawrence Livermore National Laboratory.

REFERENCES

1. C. J. Randall, J. R. Albritton, and J. J. Thomson, Phys. Fluids **24**, 1474 (1981).
2. R. S. Craxton, K. S. Anderson, T. R. Boehly, V. N. Goncharov, D. R. Harding, J. P. Knauer, R. L. McCrory, P. W. McKenty, D. D. Meyerhofer, J. F. Myatt, A. J. Schmitt, J. D. Sethian, R. W. Short, S. Skupsky, W. Theobald, W. L. Kruer, K. Tanaka, R. Betti, T. J. B. Collins, J. A. Delettrez, S. X. Hu, J. A. Marozas, A. V. Maximov, D. T. Michel, P. B. Radha, S. P. Regan, T. C. Sangster, W. Seka, A. A. Solodov, J. M. Soures, C. Stoeckl, and J. D. Zuegel, Phys. Plasmas **22**, 110501 (2015).
3. W. Seka, D. H. Edgell, J. P. Knauer, J. F. Myatt, A. V. Maximov, R. W. Short, T. C. Sangster, C. Stoeckl, R. E. Bahr, R. S. Craxton, J. A. Delettrez, V. N. Goncharov, I. V. Igumenshchev, and D. Shvarts, Phys. Plasmas **15**, 056312 (2008).
4. I. V. Igumenshchev, D. H. Edgell, V. N. Goncharov, J. A. Delettrez, A. V. Maximov, J. F. Myatt, W. Seka, A. Shvydky, S. Skupsky, and C. Stoeckl, Phys. Plasmas **17**, 122708 (2010).
5. I. V. Igumenshchev, W. Seka, D. H. Edgell, D. T. Michel, D. H. Froula, V. N. Goncharov, R. S. Craxton, L. Divol, R. Epstein, R. Follett, J. H. Kelly, T. Z. Kosc, A. V. Maximov, R. L. McCrory, D. D. Meyerhofer, P. Michel, J. F. Myatt, T. C. Sangster, A. Shvydky, S. Skupsky, and C. Stoeckl, Phys. Plasmas **19**, 056314 (2012).
6. A. K. Davis, D. Cao, D. T. Michel, M. Hohenberger, D. H. Edgell, R. Epstein, V. N. Goncharov, S. X. Hu, I. V. Igumenshchev, J. A. Marozas, A. V. Maximov, J. F. Myatt, P. B. Radha, S. P. Regan, T. C. Sangster, and D. H. Froula, Phys. Plasmas **23**, 056306 (2016).
7. D. H. Edgell, R. K. Follett, I. V. Igumenshchev, J. F. Myatt, J. G. Shaw, and D. H. Froula, Phys. Plasmas **24**, 062706 (2017).
8. J. D. Lindl, Phys. Plasmas **2**, 3933 (1995).
9. W. L. Kruer *et al*., Phys. Plasmas **3**, 382 (1996).
10. E. A. Williams, B. I. Cohen, L. Divol, M. R. Dorr, J. A. Hittinger, D. E. Hinkel, A. B. Langdon, R. K. Kirkwood, D. H. Froula, and S. H. Glenzer, Phys. Plasmas **11**, 231 (2004).
11. P. Michel *et al*., Phys. Rev. Lett. **102**, 025004 (2009).
12. S. H. Glenzer *et al*., Science **327**, 1228 (2010).
13. J. D. Moody *et al*., Nat. Phys. **8**, 344 (2012).
14. D. Turnbull, P. Michel, J. E. Ralph, L. Divol, J. S. Ross, L. F. Berzak Hopkins, A. L. Kritcher, D. E. Hinkel, and J. D. Moody, Phys. Rev. Lett. **114**, 125001 (2015).
15. P. Michel, L. Divol, D. Turnbull, and J. D Moody, Phys. Rev. Lett. **113**, 205001 (2014).
16. D. Turnbull, P. Michel, T. Chapman, E. Tubman, B. B Pollock, C. Y Chen, C. Goyon, J. S Ross, L. Divol, N. Woolsey, and J. D Moody, Phys. Rev. Lett. **116**, 205001 (2016).
17. D. Turnbull, C. Goyon, G. E. Kemp, B. B. Pollock, D. Mariscal, L. Divol, J. S. Ross, S. Patankar, J. D. Moody, and P. Michel, Phys. Rev. Lett. **118**, 015001 (2017).
18. M. M. Marinak *et al*., Phys. Plasmas **8**, 2275 (2001).
19. R. K. Follett, D. H. Edgell, D. H. Froula, V. N. Goncharov, I. V. Igumenshchev, J. G. Shaw, and J. F. Myatt, Phys. Plasma **24**, 103128 (2017).
20. H. A. Rose and D. F. DuBois, Phys. Fluids B **5**, 590 (1993).
21. A. Colaïtis, T. Chapman, D. Strozzi, L. Divol, and P. Michel, “A Tesselation-Based Model for Intensity Estimation and Laser–Plasma

Interaction Calculations in Three Dimensions," to be published in Physics of Plasmas.

22. B. I. Cohen *et al*., Phys. Plasmas **5**, 3408 (1998).

23. P. Michel *et al*., Phys. Rev. Lett. **109**, 195004 (2012).

24. P. Michel *et al*., Phys. Plasmas **20**, 056308 (2013).

25. K. Estabrook, W. L. Kruer, and M. G. Haines, Phys. Fluids B **1**, 1282 (1989).

26. W. L. Kruer *et al*., Phys. Scr. **1998**, T75 (1998).

27. C. Labaune *et al*., Phys. Rev. Lett. **82**, 3613 (1999).

28. C. Niemann, S. H. Glenzer, J. Knight, L. Divol, E. A. Williams, G. Gregori, B. I. Cohen, C. Constantin, D. H. Froula, D. S. Montgomery, and R. P. Johnson, Phys. Rev. Lett. **93**, 045004 (2004).

29. H. C. Bandulaet *et al*., Phys. Rev. Lett. **93**, 035002 (2004).

30. B. I. Cohen *et al*., Phys. Plasmas **12**, 052703 (2005).

31. R. L. Berger *et al*., Phys. Plasmas **20**, 032107 (2013).

32. E. A. Williams *et al*., Phys. Plasmas **2**, 129 (1995).

33. T. Chapman *et al*., Phys. Rev. Lett. **119**, 055002 (2017).

34. R. K. Kirkwood *et al*., Phys. Rev. Lett. **76**, 2065 (1996).

35. A. Colaïtis, S. Hüller, D. Pesme, G. Duchateau, and V. T. Tikhonchuk, Phys. Plasmas **23**, 032118 (2016).

36. R. K. Kirkwood, D. P. Turnbull, T. Chapman, S. C. Wilks, M. D. Rosen, R. A. London, L. A. Pickworth, W. H. Dunlop, J. D. Moody, D. J. Strozzi, P. A. Michel, L. Divol, O. L. Landen, B. J. MacGowan, B. M. Van Wonterghem, K. B. Fournier, and B. E. Blue, Nat. Phys. **14**, 80 (2018).

Suppressing Two-Plasmon Decay with Laser Frequency Detuning

In direct-drive inertial confinement fusion (ICF), a cryogenic capsule of deuterium–tritium fuel with a thin outer ablator material is imploded by direct laser illumination.[1,2] An efficient implosion maximizes the amount of laser energy that is converted into kinetic energy of the imploding shell while minimizing the premature heating of the cold fuel by hot-electron preheat.[3] Preheat reduces the implosion efficiency by decreasing the compressibility of the capsule. Radiation–hydrodynamic simulations suggest that converting as little as 0.1% of the incident laser energy into preheat can significantly degrade implosion performance.[4]

The dominant source of hot electrons in direct-drive ICF experiments on the OMEGA laser[5] is the two-plasmon–decay (TPD) instability.[6] Two-plasmon decay occurs when an incident light wave decays into two electron plasma waves (EPW's) at near-quarter-critical densities.[7–10] When the driven EPW's become large in amplitude, the instability undergoes nonlinear saturation, resulting in a broad spectrum of EPW's[11,12] that can stochastically accelerate electrons to energies >100 keV (Ref. 13). The fraction of incident laser energy converted into hot electrons (f_{hot}) has been observed to exceed 1% at ignition-relevant laser intensities,[14] and experiments indicate that ~25% of the hot-electron energy is coupled to the cold fuel.[15] This suggests that hot-electron preheat is close to or above tolerable levels in the highest-intensity OMEGA experiments.

TPD-driven preheat currently limits the peak laser intensity in direct-drive ICF implosions to ~10^{15} W/cm^2. A number of studies have shown that alternative ablator materials can be used to mitigate TPD,[16,17] but this approach allows for only modest increases in laser intensity and precludes the optimization of the ablator for hydrodynamic efficiency.

The main reason that TPD is a limiting instability for direct-drive ICF is that many overlapping laser beams can drive the instability cooperatively.[18] This results in hot electrons being observed even when the single-beam laser intensities are well below the instability threshold. The requirement of spatial coherence of the cooperating beams restricts them to lie on a cone in the homogeneous theory,[19,20] but the short spatial extent of the TPD interaction region in inhomogeneous plasmas allows for a cooperative interaction between laser beams with a correspondingly short coherence length.[21] The cooperative nature of the instability, however, also provides a unique path to TPD suppression by decoupling the multibeam instability.

In this article we present computer simulations that indicate that frequency detuning of the drive laser beams can suppress the TPD instability and corresponding hot-electron generation in direct-drive ICF using existing lasers. Three-dimensional simulations using realistic plasma conditions and the laser configuration for an OMEGA implosion indicate that frequency detuning of $\Delta\omega/\omega_0 \sim 0.7\%$ (1.76 nm) is sufficient to decouple a pair of laser beams, effectively doubling the intensity threshold for the onset of hot-electron generation. The simulations show that suppression of the absolute instability[9] is sufficient to eliminate TPD-driven hot-electron production, and that 0.7% frequency detuning would be more than enough to eliminate TPD-driven hot-electron production in OMEGA experiments. Further increases in the available detuning would allow the laser to be divided into more distinct frequencies, which can further increase the instability threshold and open up the ICF design space. This result is in contrast to using continuous-bandwidth lasers where the same reduction in hot electrons would require at least as much bandwidth, which is not achievable with current ICF laser systems.

It was recognized in early studies that temporal incoherence in the form of laser bandwidth could be used to suppress laser–plasma instabilities,[22,23] but the large-scale glass lasers that are currently used to conduct ICF experiments are nearly monochromatic ($\delta\omega/\omega_0 < 0.1\%$, where $\delta\omega$ is the laser bandwidth). Frequency detuning (i.e., introduction of multiple discrete frequencies) of a fraction of the laser beams has been used to control symmetry in indirect-drive ICF experiments[24] and to mitigate cross-beam energy transfer in polar-direct-drive experiments at the National Ignition Facility (NIF).[25] This technique was generally not expected to be useful for TPD suppression at the modest frequency shifts that are currently available. Early work showed that the homogeneous temporal growth rate (γ_0) could be reduced by a factor of $\gamma_0/\delta\omega$ when $\delta\omega \gg \gamma_0$ (Refs. 22, 26, and 27). The homogeneous growth rate for TPD can easily be ~1% of the laser frequency for ICF conditions, which suggests $\delta\omega/\omega_0 \gg 1\%$ is required to have a significant impact on TPD.[28,29] In an inhomogeneous plasma, however, these results are only directly applicable to instabilities that saturate convectively (i.e., undergo finite spatial amplification) because the convective gain is directly related to the linear growth rate. Two-plasmon decay becomes absolutely unstable (temporal growth at a fixed point in space) when the convective gain is relatively small ($\lesssim 2\pi$) (Ref. 30). The linear growth rate plays a reduced role in absolute instabilities because they always grow until saturated by some nonlinear mechanism.

Two-plasmon–decay simulations were performed using the *LPSE* (laser-plasma simulation environment) code.[11] The *LPSE* modules used in this study were the pseudospectral solver[31] for the extended Zakharov equations for TPD[32] and the hybrid particle evolution (HPE) module.[21] *LPSE* has had considerable success in reproducing previous experimental results, including measured plasma wave amplitudes[11] and hot-electron generation,[21] which suggests that the simulation results give a quantitative representation of what would be observed in experiments.

The 3-D *LPSE* simulations were performed in a 67.5 × 13 × 13-μm^3 region on a 1688 × 324 × 324-cell Cartesian grid. There was a linearly varying density along the x direction from $n_e/n_c = 0.19$ to 0.27, where n_e is the electron density and n_c is the critical density for the 351-nm drive beams. This gives a scale length of $L_n = 211$ μm at $n_c/4$. A plastic (CH) plasma was used with an electron (ion) temperature of T_e = 2.6 keV (T_i = 1.0 keV) and a Mach 1.2 flow antiparallel to the density gradient. These plasma conditions were determined from radiation–hydrodynamic simulations of an OMEGA implosion using the code *LILAC*.[33] Because the results are sensitive to the relative phase of the drive beams, all of the *LPSE* results correspond to the mean and standard deviation of five-run ensembles with random polarizations, phases, and speckle patterns.

Figure 153.33 shows the absolute instability thresholds from 3-D *LPSE* simulations that were designed to emulate the quarter-critical conditions in an OMEGA implosion near the time of peak hot-electron production. The overlapped laser intensities are normalized to the analytic result for the absolute threshold of a monochromatic plane wave $I_{\text{Simon}} = 233\, T_e/L_n$ in units of 10^{14} W/cm^2 (Ref. 9). A single OMEGA "hex" was simulated consisting of six laser beams incident from the corners of a hexagon, each with an angle of 23° relative to the density gradient (Fig. 153.34). The beams were simulated with phase plates and polarization smoothing, as described in Ref. 11. The simulations were performed with two or three laser frequencies, and two different methods were used to split the beams into multiple frequencies: (1) "multicolor," where each beam was split into N_ω frequencies with each frequency component containing $1/N_\omega$ of the laser energy, and (2) "tiled,"

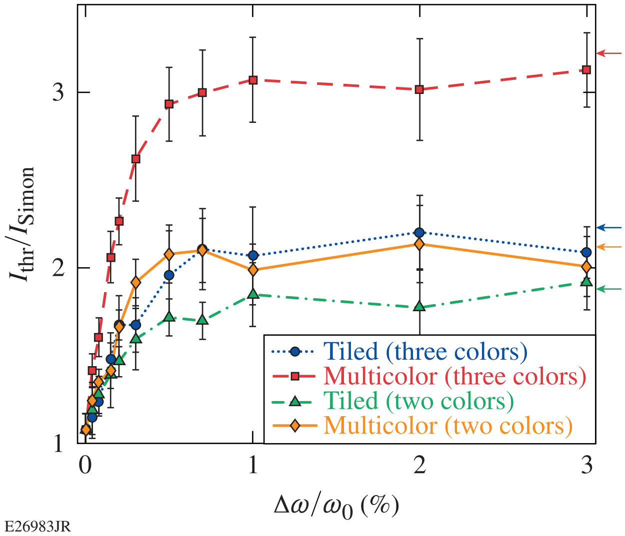

Figure 153.33
LPSE-simulated absolute two-plasmon–decay (TPD) thresholds for various types of frequency detuning. The curves correspond to three-color multicolor (red squares) and tiled (blues circles) detuning and two-color multicolor (orange diamonds) and tiled (green triangles) detuning. The arrows at the right edge indicate the expected asymptotic thresholds.

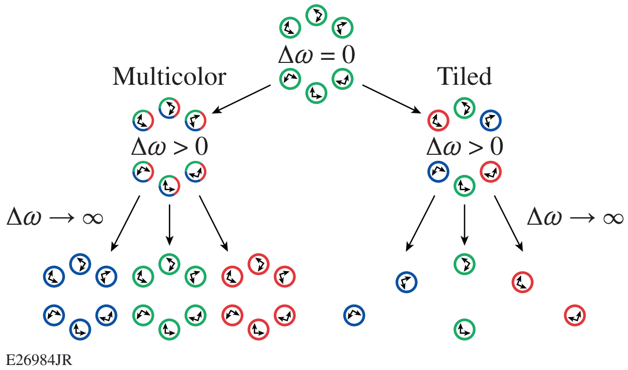

Figure 153.34
Schematic of the effect of three-color multicolor and tiled frequency detuning. The arrows correspond to one realization of random polarization with polarization smoothing. The third row corresponds to the three effective interactions occurring at different densities when the three frequencies are fully decoupled; the absolute threshold is three times the minimum threshold.

where each beam is monochromatic, but the different beams have different frequencies (alternating around the corners of the hexagon). In all cases, $\Delta\omega/\omega_0 \approx 0.7\%$ was sufficient to reach the asymptotic ($\Delta\omega \rightarrow \infty$) threshold ($\Delta\omega$ is the nearest-neighbor frequency separation).

Despite the multicolor approach being superior from the point of view of TPD suppression because of the higher instability thresholds, the tiled approach is included here because it is an easier laser architecture to implement and resembles what is currently available on large-scale laser facilities. For instance, the NIF[34] uses a tiled laser architecture that currently has $\Delta\omega/\omega_0 \approx 0.15\%$ with $\Delta\omega/\omega_0 = 0.35\%$ achievable with minor modifications. One of the OMEGA EP[35] beams has recently been upgraded to have $\Delta\omega/\omega_0 \approx 1\%$.

Figure 153.34 illustrates why the multicolor and tiled approaches to frequency detuning give different instability thresholds in the asymptotic limit of large $\Delta\omega/\omega_0$. In both cases the distinct frequencies decouple in the asymptotic limit, but in the multicolor approach, the threshold is simply N_ω times the threshold for $\Delta\omega = 0$ because the decoupling effectively results in N_ω six-beam interactions that are identical to the six-beam interaction at zero frequency detuning. When the individual beams have different frequencies, there are only $6/N_\omega$ beams in each of the N_ω groups of decoupled monochromatic beams. In this case, the effective decoupled configurations are not equivalent to the original six-beam configuration. For random polarizations, the different groups of decoupled beams will have different thresholds, and the overall threshold for the configuration to be absolutely unstable will be N_ω times the minimum threshold for the $6/N_\omega$ different groups. This qualitative picture suggests an alternative way to calculate the asymptotic thresholds in the tiled configuration: run N_ω monochromatic simulations with $6/N_\omega$ beams (random polarizations) and take N_ω times the minimum threshold as the expected asymptotic threshold. Repeating this procedure for an ensemble of five realizations of polarization and phase gives asymptotic thresholds of 2.27±0.30 for $N_\omega = 3$ and 1.84±0.12 for $N_\omega = 2$, which are in agreement with the corresponding results in Fig. 153.33 (2.09±0.15 for $N_\omega = 3$ and 1.92±0.16 for $N_\omega = 2$).

In the ICF context, the figure of merit for TPD mitigation is reducing hot-electron production. A commonly used semi-empirical metric for the onset of hot-electron production in multibeam experiments is the single-beam absolute threshold evaluated at the overlapped laser intensity. For this to be a useful metric, the following pair of conditions must be met: (1) the onset of hot-electron production corresponding to absolute instability, and (2) a multibeam absolute threshold identical to the single-beam threshold (using overlapped laser intensity). The first condition is true because the absolute threshold occurs when the convective gains are modest, so the convectively saturated waves are not large enough to generate significant hot electrons. It is not obvious that the second condition should hold for multiple beams with phase plates, polarization smoothing, and random relative polarizations, but note that in Fig. 153.33, the threshold at zero detuning is relatively close to the single-beam threshold. This behavior results from a combination of three effects: (1) the six beams act cooperatively to drive a common wave; (2) the random relative polarizations/phases of the beams tend to increase the threshold intensity; and (3) the phase plates cause the beams to have localized hot spots that effectively reduce the threshold.

Figure 153.35 shows the fraction of incident laser energy converted into hot electrons (>50 keV) in six-beam, three-color *LPSE* simulations. Two laser intensities were used: 4×10^{14} W/cm^2 and 7×10^{14} W/cm^2, which correspond to $I_{\text{thr}}/I_{\text{Simon}} = 1.63$ and 2.86, respectively. At $I = 4 \times 10^{14}$ W/cm^2, only ~0.1% frequency detuning was required to eliminate hot-electron production in the multicolor configuration, whereas ~0.3% was required in the tiled configuration. At $I = 7 \times 10^{14}$ W/cm^2, ~0.7% detuning was

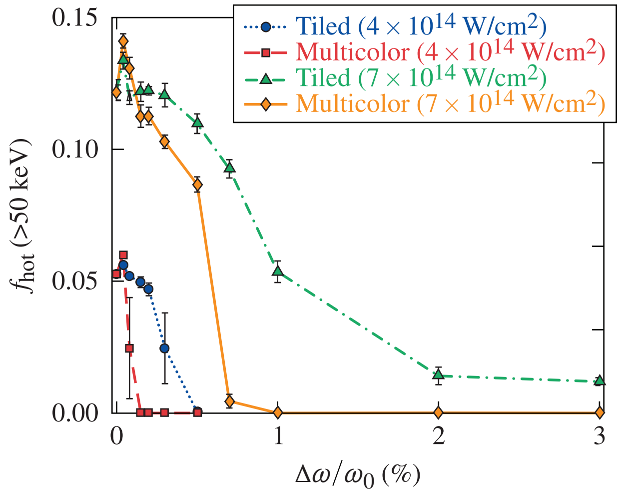

Figure 153.35
LPSE-simulated fraction of incident laser energy converted into hot electrons with energy >50 keV using OMEGA plasma conditions and three-color beams. The four curves correspond to the tiled (blue circles) and multicolor (red squares) configurations at $I = 4 \times 10^{14}$ W/cm^2 and the tiled (green triangles) and multicolor (orange diamonds) configurations at $I = 7 \times 10^{14}$ W/cm^2. The hot-electron production was taken as the average over 5 ps after the simulations reached a quasi steady state (12 ps).

required in the multicolor configuration, and no amount of detuning was sufficient to completely suppress hot-electron production in the tiled configuration because some of the frequency-matched beam pairs were still above the absolute threshold, even when the various colors were completely decoupled. This is consistent with the results shown in Fig. 153.33, where $I_{\text{thr}}/I_{\text{Simon}}$ never gets above 2.86 in the three-color tiled configuration, which is required to suppress the absolute instability at $I = 7 \times 10^{14}$ W/cm^2.

Note that the laser intensities used in Fig. 153.35 correspond to the overlapped intensity at the quarter-critical surface. The quoted laser intensity for an ICF implosion design typically corresponds to the peak laser power divided by the surface area of the undriven target, which is about 3× the intensity at $n_{\text{c}}/4$ in OMEGA implosions. The simulations at 4×10^{14} W/cm^2 correspond to the peak laser intensities that are currently available on OMEGA. The hot-electron fractions shown in Fig. 153.35 are a few times higher than what is observed in OMEGA implosions because they correspond to instantaneous rather than time-averaged hot-electron production.

To show the physical behavior in the simplest possible configuration, 2-D *LPSE* simulations were performed using normally incident plane waves. The grid and plasma conditions in the 2-D simulations were identical to the 3-D simulations along the x and y dimensions except that the EPW damping and flow were turned off. Figure 153.36 shows the absolute instability thresholds from *LPSE* simulations of two to five p-polarized, collinear plane-wave beams with electric field (enveloped at ω_0)

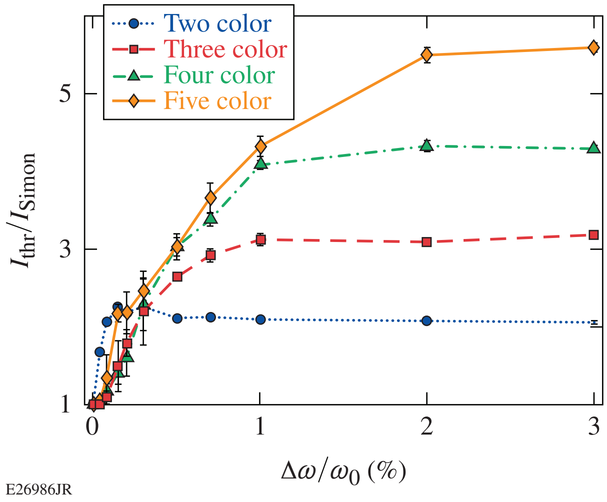

Figure 153.36
Absolute instability thresholds from 2-D *LPSE* simulations of collinear, plane-wave beams using two (blue circles), three (red squares), four (green triangles), and five (orange diamonds) colors.

$$\mathbf{E}_0 = \hat{y}\,\frac{E_0}{2}\sum_{j=1}^{N_\omega} e^{i\left(k_j x - \Delta\omega_j t + \phi_j\right)} + \text{c.c.},$$

where ϕ_j is the initial phase of the jth beam,

$$\Delta\omega_j = \left[j - \left(N_\omega + 1\right)/2\right]\Delta\omega$$

is the frequency shift,

$$k_j = \left(\omega_0/c\right)\sqrt{\left(1 + \Delta\omega_j/\omega_0\right)^2 - n_{\text{e}}/n_{\text{c}}},$$

and in cgs units $E_0 = \sqrt{8\pi I/\left[c\left(1 - n_{\text{e}}/n_{\text{c}}\right)^{1/2}\right]}$ (note that the maximum frequency separation increases with increasing N_ω because $\Delta\omega$ is defined as the frequency difference between nearest-neighbor frequencies). At zero wavelength detuning, the analytic absolute threshold (I_{Simon}) is reproduced. As $\Delta\omega \longrightarrow \infty$, the threshold goes to $N_\omega I_{\text{Simon}}$ because the absolutely unstable modes become spatially decoupled (i.e., each frequency independently drives TPD at its own quarter-critical surface).

Figure 153.37(a) shows the spatial structure of the absolutely unstable plasma modes from an *LPSE* simulation of a monochromatic plane wave. The absolutely unstable modes occur over a narrow spatial region (~2 μm wide) centered at $x \approx 12\ \mu\text{m}\left(n_{\text{e}}/n_{\text{c}} = 0.244\right)$. Figure 153.37(b) shows the spatial structure of the absolute instability for $\Delta\omega/\omega_0$ = 1%, where the absolutely unstable regions have separated spatially by ~4.1 μm. This corresponds to a 2% change in density, consistent with the expectation that the resonant density should vary as the square of the resonant frequency. Note that although the modes have separated spatially, the wavelength of the transverse beat between the unstable modes is shorter in the two-color case. Amplitude modulation in the pump beam causes the most-unstable transverse wave number to be larger (shorter wavelength) in the two-color case because of its square root dependence on the laser intensity.[9]

An unintuitive aspect of the results shown in Fig. 153.36 is that the instability threshold increases most rapidly in the two-color case at small $\Delta\omega$. Our expectation was that increasing the number of colors would increase the decoupling rate because the effective amount of temporal incoherence is an increasing function of N_ω. To verify that this is not an artifact of the time-enveloped pseudospectral solver used in *LPSE*, an independent test was performed by solving Eqs. (1) and (2) from Simon *et al.*,[9] which are not time enveloped, using finite differencing.

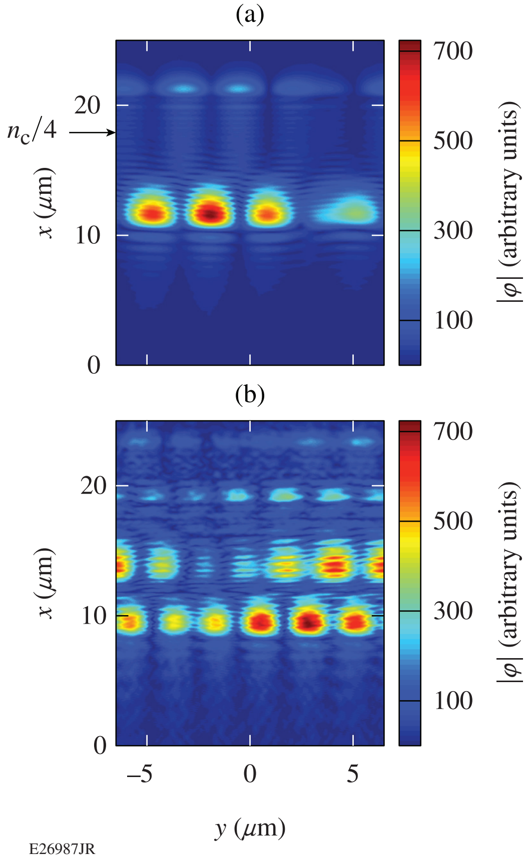

Figure 153.37
Color maps of the electrostatic potential from 2-D *LPSE* simulations late in time ($t = 10$ ps) when the field structure is dominated by the absolutely unstable modes. (a) Zero frequency detuning and (b) 1% frequency detuning (two color). Only a small portion of the simulation region is shown corresponding to $n_e/n_c = 0.23$ to 0.26.

The calculations were performed on a subscale grid, but the same qualitative behavior was observed. The large variation in threshold over the ensemble of initial phases for $N_\omega > 2$ suggests that amplitude modulation has a significant impact on the thresholds. When speckled beams are used, the threshold always increases with increasing N_ω, so this effect was not present in the 3-D calculations, all of which had speckled beams.

In summary, we have shown that hot-electron mitigation can potentially be achieved using the modest amount of laser frequency detuning that is available on existing laser facilities ($\Delta\omega/\omega_0 \sim 0.7\%$). Three-dimensional *LPSE* simulations using realistic direct-drive ICF conditions show that decoupling of the multibeam instability significantly increases the absolute instability threshold, and that suppression of the absolute instability effectively eliminates TPD-driven hot-electron generation. The validity of these results is supported by the fact that *LPSE* simulations have reproduced both wave-amplitude and hot-electron measurements from previous experiments. This method of TPD mitigation can be scaled to higher laser intensities by increasing the available frequency detuning, which can open up the design space for future ICF implosions.

ACKNOWLEDGMENT

This material is based upon work supported by the Department of Energy National Nuclear Security Administration under Award No. DE-NA0001944, the University of Rochester, and the New York State Energy Research and Development Authority. The support of the DOE does not constitute an endorsement by the DOE of the views expressed in this article.

REFERENCES

1. S. Atzeni and J. Meyer-ter-Vehn, *The Physics of Inertial Fusion: Beam Plasma Interaction, Hydrodynamics, Hot Dense Matter*, 1st ed., International Series of Monographs on Physics, Vol. 125 (Oxford University Press, Oxford, 2004).
2. R. S. Craxton, K. S. Anderson, T. R. Boehly, V. N. Goncharov, D. R. Harding, J. P. Knauer, R. L. McCrory, P. W. McKenty, D. D. Meyerhofer, J. F. Myatt, A. J. Schmitt, J. D. Sethian, R. W. Short, S. Skupsky, W. Theobald, W. L. Kruer, K. Tanaka, R. Betti, T. J. B. Collins, J. A. Delettrez, S. X. Hu, J. A. Marozas, A. V. Maximov, D. T. Michel, P. B. Radha, S. P. Regan, T. C. Sangster, W. Seka, A. A. Solodov, J. M. Soures, C. Stoeckl, and J. D. Zuegel, Phys. Plasmas **22**, 110501 (2015).
3. V. N. Goncharov, T. C. Sangster, R. Betti, T. R. Boehly, M. J. Bonino, T. J. B. Collins, R. S. Craxton, J. A. Delettrez, D. H. Edgell, R. Epstein, R. K. Follet, C. J. Forrest, D. H. Froula, V. Yu. Glebov, D. R. Harding, R. J. Henchen, S. X. Hu, I. V. Igumenshchev, R. Janezic, J. H. Kelly, T. J. Kessler, T. Z. Kosc, S. J. Loucks, J. A. Marozas, F. J. Marshall, A. V. Maximov, R. L. McCrory, P. W. McKenty, D. D. Meyerhofer, D. T. Michel, J. F. Myatt, R. Nora, P. B. Radha, S. P. Regan, W. Seka, W. T. Shmayda, R. W. Short, A. Shvydky, S. Skupsky, C. Stoeckl, B. Yaakobi, J. A. Frenje, M. Gatu-Johnson, R. D. Petrasso, and D. T. Casey, Phys. Plasmas **21**, 056315 (2014).
4. R. L. McCrory, D. D. Meyerhofer, R. Betti, R. S. Craxton, J. A. Delettrez, D. H. Edgell, V. Yu. Glebov, V. N. Goncharov, D. R. Harding, D. W. Jacobs-Perkins, J. P. Knauer, F. J. Marshall, P. W. McKenty, P. B. Radha, S. P. Regan, T. C. Sangster, W. Seka, R. W. Short, S. Skupsky, V. A. Smalyuk, J. M. Soures, C. Stoeckl, B. Yaakobi, D. Shvarts, J. A. Frenje, C. K. Li, R. D. Petrasso, and F. H. Séguin, Phys. Plasmas **15**, 055503 (2008).
5. T. R. Boehly, R. S. Craxton, T. H. Hinterman, J. H. Kelly, T. J. Kessler, S. A. Kumpan, S. A. Letzring, R. L. McCrory, S. F. B. Morse, W. Seka, S. Skupsky, J. M. Soures, and C. P. Verdon, Rev. Sci. Instrum. **66**, 508 (1995).
6. B. Yaakobi, C. Stoeckl, T. Boehly, D. D. Meyerhofer, and W. Seka, Phys. Plasmas **7**, 3714 (2000).
7. E. A. Jackson, Phys. Rev. **153**, 235 (1967).
8. C. S. Liu and M. N. Rosenbluth, Phys. Fluids **19**, 967 (1976).

9. A. Simon, R. W. Short, E. A. Williams, and T. Dewandre, Phys. Fluids **26**, 3107 (1983).
10. J. F. Myatt, J. Zhang, R. W. Short, A. V. Maximov, W. Seka, D. H. Froula, D. H. Edgell, D. T. Michel, I. V. Igumenshchev, D. E. Hinkel, P. Michel, and J. D. Moody, Phys. Plasmas **21**, 055501 (2014).
11. R. K. Follett, D. H. Edgell, R. J. Henchen, S. X. Hu, J. Katz, D. T. Michel, J. F. Myatt, J. Shaw, and D. H. Froula, Phys. Rev. E **91**, 031104(R) (2015).
12. W. Seka, D. H. Edgell, J. F. Myatt, A. V. Maximov, R. W. Short, V. N. Goncharov, and H. A. Baldis, Phys. Plasmas **16**, 052701 (2009).
13. R. Yan, C. Ren, J. Li, A. V. Maximov, W. B. Mori, Z.-M. Sheng, and F. S. Tsung, Phys. Rev. Lett. **108**, 175002 (2012).
14. D. H. Froula, I. V. Igumenshchev, D. T. Michel, D. H. Edgell, R. Follett, V. Yu. Glebov, V. N. Goncharov, J. Kwiatkowski, F. J. Marshall, P. B. Radha, W. Seka, C. Sorce, S. Stagnitto, C. Stoeckl, and T. C. Sangster, Phys. Rev. Lett. **108**, 125003 (2012).
15. B. Yaakobi, A. A. Solodov, J. F. Myatt, J. A. Delettrez, C. Stoeckl, and D. H. Froula, Phys. Plasmas **20**, 092706 (2013).
16. R. K. Follett, J. A. Delettrez, D. H. Edgell, V. N. Goncharov, R. J. Henchen, J. Katz, D. T. Michel, J. F. Myatt, J. Shaw, A. A. Solodov, C. Stoeckl, B. Yaakobi, and D. H. Froula, Phys. Rev. Lett. **116**, 155002 (2016).
17. J. F. Myatt, H. X. Vu, D. F. DuBois, D. A. Russell, J. Zhang, R. W. Short, and A. V. Maximov, Phys. Plasmas **20**, 052705 (2013).
18. C. Stoeckl, R. E. Bahr, B. Yaakobi, W. Seka, S. P. Regan, R. S. Craxton, J. A. Delettrez, R. W. Short, J. Myatt, A. V. Maximov, and H. Baldis, Phys. Rev. Lett. **90**, 235002 (2003).
19. D. F. DuBois, B. Bezzerides, and H. A. Rose, Phys. Fluids B **4**, 241 (1992).
20. D. T. Michel, A. V. Maximov, R. W. Short, S. X. Hu, J. F. Myatt, W. Seka, A. A. Solodov, B. Yaakobi, and D. H. Froula, Phys. Rev. Lett. **109**, 155007 (2012).
21. R. K. Follett, J. F. Myatt, J. G. Shaw, D. T. Michel, A. A. Solodov, D. H. Edgell, B. Yaakobi, and D. H. Froula, Phys. Plasmas **24**, 102134 (2017).
22. J. J. Thomson and J. I. Karush, Phys. Fluids **17**, 1608 (1974).
23. S. P. Obenschain *et al*., Phys. Rev. Lett. **56**, 2807 (1986).
24. P. Michel *et al*., Phys. Rev. Lett. **102**, 025004 (2009).
25. J. A. Marozas, M. Hohenberger, M. J. Rosenberg, D. Turnbull, T. J. B. Collins, P. B. Radha, P. W. McKenty, J. D. Zuegel, F. J. Marshall, S. P. Regan, T. C. Sangster, W. Seka, E. M. Campbell, V. N. Goncharov, M. W. Bowers, J.-M. G. DiNicola, G. Erbert, B. J. MacGowan, L. J. Pelz, and S. T. Yang, "First Observation of Cross-Beam Energy Transfer Mitigation for Direct-Drive Inertial Confinement Fusion Implosions Using Wavelength Detuning at the National Ignition Facility," to be published in Physical Review Letters.
26. G. Laval, R. Pellat, and D. Pesme, Phys. Rev. Lett. **36**, 192 (1976).
27. G. Laval *et al*., Phys. Fluids **20**, 2049 (1977).
28. D. Eimerl and A. J. Schmitt, Plasma Phys. Control. Fusion **58**, 115006 (2016).
29. Y. Zhao *et al*., Phys. Plasmas **24**, 112102 (2017).
30. J. Zhang, J. F. Myatt, R. W. Short, A. V. Maximov, H. X. Vu, D. F. DuBois, and D. A. Russell, Phys. Rev. Lett. **113**, 105001 (2014).
31. B. Fornberg, *A Practical Guide to Pseudospectral Methods*, Cambridge Monographs on Applied and Computational Mathematics, Vol. 1 (Cambridge University Press, Cambridge, England, 1998).
32. D. F. DuBois, D. A. Russell, and H. A. Rose, Phys. Rev. Lett. **74**, 3983 (1995).
33. J. Delettrez, R. Epstein, M. C. Richardson, P. A. Jaanimagi, and B. L. Henke, Phys. Rev. A **36**, 3926 (1987).
34. E. I. Moses *et al*., Phys. Plasmas **16**, 041006 (2009).
35. D. D. Meyerhofer, J. Bromage, C. Dorrer, J. H. Kelly, B. E. Kruschwitz, S. J. Loucks, R. L. McCrory, S. F. B. Morse, J. F. Myatt, P. M. Nilson, J. Qiao, T. C. Sangster, C. Stoeckl, L. J. Waxer, and J. D. Zuegel, J. Phys.: Conf. Ser. **244**, 032010 (2010).

Partitioning of Tritium Between Surface and Bulk of 316 Stainless Steel at Room Temperature

Introduction

The interaction of tritium with the native oxides on the surface of stainless steel is the first step toward adsorption and absorption of tritium into the bulk stainless-steel lattice. Understanding this fundamental interaction is necessary for the development of surfaces that minimize tritium absorption and tritium permeation through piping materials in nuclear reactors. Much work has been done to measure the distribution of tritium within stainless-steel samples[1–7] and to test the influence of different surface modifications on the absorption and permeation of tritium through stainless steel.[8–15] Several conclusions can already be drawn from this body of work. Firstly, the surface comprising <15 nm and near surface comprising <0.1-μm layers of tritium-loaded stainless-steel samples contain relatively large fractions of the total tritium inventory.[4] These large surface concentrations are likely caused by tritium dissolved within the ubiquitous adsorbed water layers on stainless-steel surfaces.[16–19] Secondly, the relatively large surface concentrations are strongly influenced by the condition of the metal surface.[19] Finally, modifying the metal surface can significantly alter the permeation[8,9,12,14] and absorption[13,15] of tritium into the substrate metal, an effect likely caused by a local equilibrium established between the tritium concentrations in the adsorbed water layers and the bulk metal lattice.[20]

In this article we present new data about the tritium partition between the adsorbed water layers and the bulk metal lattice. This distribution was measured using two different techniques: a low-temperature pulsed plasma[20] and an aqueous $ZnCl_2$ method adapted from Tanaka *et al.*[21] Both methods remove surface-adsorbed tritium. Thermal desorption was also used to measure tritium dissolved in the bulk metal lattice. The pulsed-plasma and $ZnCl_2$ methods allow for the removal of the adsorbed water layers without etching into the substrate metal lattice. The pulsed-plasma method accomplishes this by bombarding the surface with energetic ions. The $ZnCl_2$ method removes the adsorbed water layers by binding the $ZnCl_2$ complex to the oxygen atoms in the hydroxyl layer. This hydroxyl layer is directly bound to the underlying native metal oxide that forms naturally on exposure to ambient air. By binding the $ZnCl_2$ complex to the surface, the multilayer structure of adsorbed water is expected to be liberated into solution, along with any tritium contained therein. Both surface removal techniques allow for the measurement of tritium adsorbed solely within the adsorbed water layers and at a finer resolution than has been reported to date.

Experimental Setups and Procedures

Samples of 5.1 × 1.9 × 0.3-cm^3 dimensions were cut from a common plate of 316 stainless steel. The total geometric surface area of each sample was 23.5 cm^2. A surface layer of ~0.86-mm depth was machined away to eliminate any surface inclusions produced in the manufacturing process and to expose the base metal lattice. The machining process produces surface striations along the machining path's axis, which adds to the overall surface roughness as discussed elsewhere.[15]

Two surface treatments were used to probe the relationship between surface finish and tritium uptake compared to unmodified surfaces. Samples that did not receive any pretreatments served as benchmarks and were labeled "as received." Ten as-received samples were baked for 2 h in dry helium at 200°C in a dry box to remove physisorbed water from the surface. These samples were labeled "as-received (baked)." Another subset of as-received samples was mechanically polished using 3 μm of MetaDi Mono Suspension diamond paste with a low-nap cloth wheel, followed by a final polish with 0.3 μm of α-alumina provided by a commercial vendor. These samples were labeled as "polished." The surface roughness of the samples was measured with a Zygo NEXview interferometer. The average surface roughness for an as-received sample was 0.27±0.06 μm. Polished samples showed an average surface roughness of 0.02±0.01 μm.

All samples were placed in an ultrasonic bath and subjected to three washes: first with acetone to degrease the surfaces, then with isopropyl alcohol, and finally with de-ionized water to remove any chemical residue. The samples were then transferred to a glove box and stored under dry helium at a dew point of –65°C. After drying in the glove box, the samples were loaded with tritium by exposure to a 1-atm mixture of DT gas with an isotopic ratio comprising 70% tritium and 30% deuterium. The tritium partial pressure was 0.54 atm. The samples were soaked in the DT gas mixture for 24 h at room temperature. Under these exposure conditions the diffusivity of tritium through stainless steel is 3.76×10^{-16} m^2/s at room temperature[20] and the tritium concentration within the bulk is not expected to be at equilibrium. After this loading, each sample was placed in an individual pod of a storage rack and sealed under dry helium to provide leak-tight storage. The storage racks were placed in a transfer box filled with a dry nitrogen atmosphere in order to minimize air exposure during the transfer from the storage rack to the experimental setup. All samples were stored in the racks until retrieved for an experiment.

The samples were subjected to one of three treatments: thermal desorption, plasma irradiation, or $ZnCl_2$ washes. In the first treatment, a sample was subjected to temperature-programmed thermal desorption (TPD) to release and measure the total quantity of tritium retained by the metal sample. Tritium release was measured by scintillation counting of the activity collected with bubblers using a Perkin Elmer Tri-Carb 2910 TR liquid scintillation counter. In the second treatment, a sample was exposed to a room-temperature Tonks–Langmuir pulsed, radio-frequency–driven plasma to release and measure the quantity of tritium bound on and in the near surface. Tritium release was measured with an in-line ionization chamber. The pulse duration was 2 s followed by a 20-min dwell between each pulse. After the pulsed-plasma treatment, the sample was placed in the thermal desorption setup to measure the residual tritium in the bulk of the metal. Both of these techniques are described in detail elsewhere;[20,22] however, some improvements have been recently installed. The carrier gas used in the TPD procedure has been upgraded to ultrahigh-purity argon, and a load-lock system is used to transfer samples from storage into the pulsed-plasma chamber to minimize exposing samples to air during the transfer.

In the third treatment, samples were washed in an aqueous $ZnCl_2$ solution to remove adsorbed tritium following a method adapted from Tanaka *et al.*[21] In this case, a sample was removed from storage under argon and soaked in a beaker containing 25 mL of 4-M ammonium chloride, 12.5 mL of 0.4-M $ZnCl_2$, and 12.5 mL of de-ionized water with the pH adjusted to 7 using concentrated ammonium hydroxide. The solution was stirred for 5 min. Afterward, the sample was removed, dried with filter paper, and placed in the thermal desorption setup to measure the residual tritium in the bulk of the metal. The activity of the tritium removed by the $ZnCl_2$ mixture and by the drying filter paper was measured using liquid scintillation counting to give the total quantity of surface tritium removed in the wash.

Results and Discussion

To determine the tritium removal efficiencies of the pulsed-plasma and $ZnCl_2$ methods, a series of six samples were treated with each method. Following the pulsed-plasma or the $ZnCl_2$ treatment, each sample was heated to 700°C in the thermal desorption facility in order to measure the residual tritium in the sample bulk. Surface activities collected from the two sample sets are shown in Figs. 153.38–153.40. The first set of measurements focused on determining the total tritium inventory and its fractionation between surface and bulk. Samples were subjected to either thermal desorption or the $ZnCl_2$ treatment followed by thermal desorption. In the second set of measurements, the efficacy of removing surface tritium by pulsed plasma or by $ZnCl_2$ washes was compared. Samples were washed in the $ZnCl_2$ solution or exposed to the pulsed plasma and then heated in the thermal desorption facility. Figures 153.38–153.40 compare the quantities of tritium removed from the surface and from the bulk for the as-received, as-received (baked), and the polished cases.

The data collected using the first series of samples are shown in Figs. 153.38 and 153.39. These data were collected

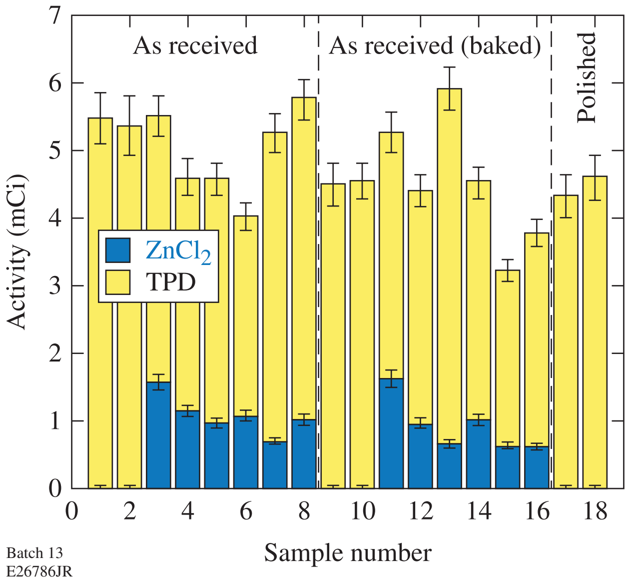

Figure 153.38
The total tritium inventory for as-received, as-received (baked), and polished stainless-steel samples. Tritium fractionation between the surface and bulk for as-received and as-received (baked) samples was determined using the $ZnCl_2$ treatment method. TPD: temperature-programmed desorption.

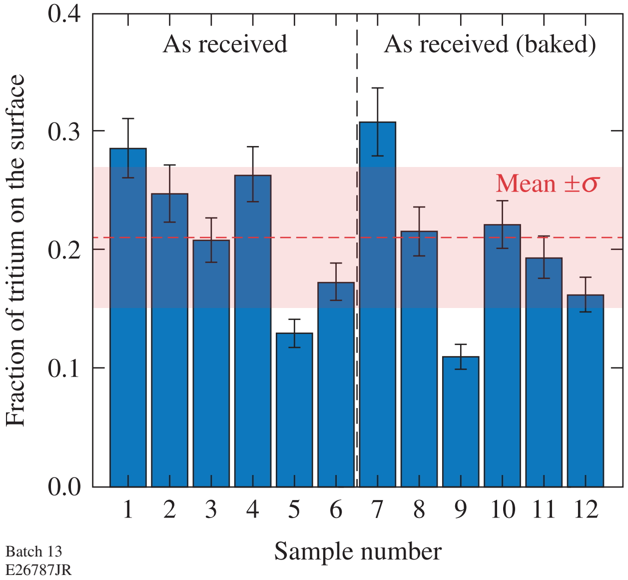

Figure 153.39
The relative fraction of the total tritium inventory residing on the surface of as-received and as-received (baked) stainless-steel samples. The horizontal dashed line provides the mean fraction without differentiating between the two treatments. The shaded band illustrates one standard deviation about the mean.

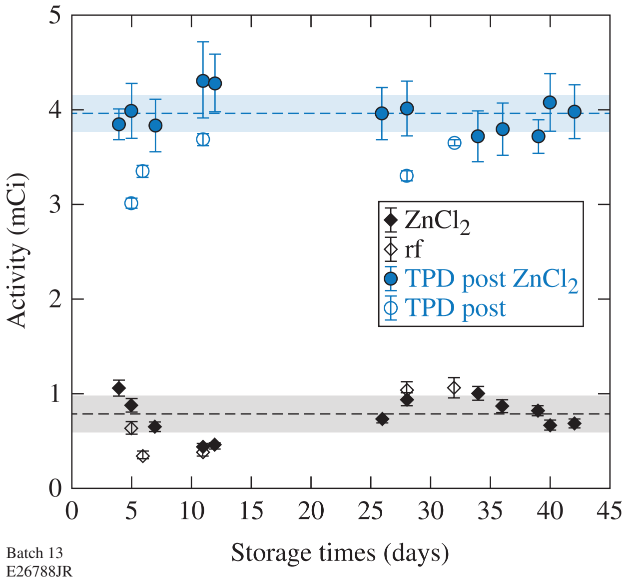

Figure 153.40
Change in the surface and bulk activities in stainless steel over 42 days of storage. Surface activity was measured using $ZnCl_2$ or pulsed plasma. Bulk activity was measured using thermal desorption. Samples subjected to pulsed plasma + thermal desorption are shown as open symbols. Samples subjected to $ZnCl_2$ + thermal desorption are shown as solid symbols. The mean surface activity is 0.8±0.2 mCi; the mean bulk activity is 4.0±0.2 mCi. The shaded bands illustrate one standard deviation about the mean. rf: radio frequency.

using a set of as-received samples, a set of as-received (baked) samples, and a set of mechanically polished samples. In this series, each sample was subjected to either thermal desorption alone or the combined procedure of a $ZnCl_2$ treatment followed by thermal desorption. The data in each plot are grouped by sample pretreatment, with the as-received sample on the left followed by the as-received (baked) samples in the center panel followed by the mechanically polished samples on the right. Figure 153.38 shows the total tritium inventory deduced for each sample. For cases where the $ZnCl_2$ surface treatment was applied, Fig. 153.38 also provides as estimate of the surface-to-bulk fractionation.

Comparing the data from samples subjected to thermal desorption only, both mechanically polished and baked samples contain similar quantities of tritium, of the order of 4.5 mCi; however, both sample sets have absorbed ~18% less tritium than the untreated as-received samples. The similarity between the total tritium inventories in mechanically polished and as-received (baked) samples suggests that surface roughness alone does not determine the total quantity of absorbed tritium, even though, after polishing, the roughness decreased tenfold. The results of the combined $ZnCl_2$ and thermal-desorption methods do not show a clear trend with sample baking.

Figure 153.39 shows the fraction of the total tritium inventory removed from the as-received and as-received (baked) samples using the $ZnCl_2$ treatment method. These fractions were calculated using the absolute activities provided in Fig. 153.38. Each fraction was calculated by dividing the measured quantity removed by the $ZnCl_2$ solution by sum of the quantities removed by the $ZnCl_2$ solution and the subsequent thermal desorption. The mean fraction of tritium on the surface and one standard deviation about the mean are also shown in Fig. 153.39.

The data in Fig. 153.39 show that the $ZnCl_2$ solution is capable of removing 21±6% of the total tritium inventory. This fraction of surface tritium removed is similar to that observed by acid etching.[4] However, given the fact that $ZnCl_2$ undercuts hydroxyls from the stainless-steel surfaces and releases all surface-bound water,[21] the present results suggest that the tritium removed by the $ZnCl_2$ solution resided solely in the adsorbed water layers. Approximately 21% of the total tritium inventory is retained on the surface of stainless steel.

The tritium occupancy in the water adsorbed on the metal surface can be estimated from first-principles calculations as follows: Water bonded to hydroxyls above the metal oxide forms a water "ice" layer.[16] The lattice parameter for that ice is 0.448 nm (Ref. 23). Assuming that the water layers above the metal oxide comprise a single hydroxyl layer, one ice layer, and zero to two adsorbed water layers, depending on the ambient relative humidity conditions,[24] then the areal density of protons present on the metal surface will range from 1.77×10^{15} to 3.76×10^{15} protons/cm^2. The surface area of the samples used in this experiment was 23.5 cm^2. Adjusting the area by using a roughness factor of 2.4 for smooth 300 series stainless steel,[25] the total number of protons on the sample surface and consequently the number of sites available for tritons to replace protons will range from 1.0 to 2.1×10^{17} sites. On average, 1.0±0.3 mCi or equivalently 2.08×10^{16} tritons were collected from the water layers adsorbed on the stainless-steel samples listed in Fig. 153.38. The triton surface occupancy dependence on the number of adsorbed water layers is provided in Table 153.VIII and is seen to range from 11% to 25% of the available sites, depending on the actual relative humidity of the environment. Only the hydroxyl and ice layers are expected to be present on the samples used in this study since the experimental procedure minimized air exposure during the loading and storage cycles.

Table 153.VIII: Dependence of tritium occupancy in surface water layers on the number of adsorbed water layers.

Number of adsorbed water layers	0	1	2
Number of available sites for tritons (10^{16})	8.4	14.1	19.7
Tritium occupancy in the surface layers (%)	25	15	11

The potential change in the distribution between surface-bound tritium and tritium residing in bulk steel was monitored over 42 days using a second series of samples. During this 42-day interval, the samples were kept under argon at room temperature. These measurements used only as-received samples that were subjected first to either $ZnCl_2$ or the pulsed-plasma treatments, followed by thermal desorption to determine the residual tritium. Figure 153.40 shows the dependence of the partition of tritium between the surface and bulk on time. The dashed lines in the figure are the mean surface and bulk activities: 0.8±0.2 mCi and 4.0±0.2 mCi, respectively. The shaded bands represent one standard deviation width centered about their respective mean.

The quantities of tritium removed by pulsed-plasma and $ZnCl_2$ washes are similar within experimental error. The pulsed-plasma method removes adsorbed tritium by low-energy argon-ion bombardment of the surface with a negligible contribution of tritium from the underlying substrate metal.[20] The $ZnCl_2$ method removes the hydroxyl layer bonded to the metal oxide layer and liberates all water layers between the hydroxyl layer and the uppermost surface by replacing the hydroxyl layer with a zinc complex. Concurrence between these two independent surface-stripping methods reinforces the assumption that the released tritium originated from adsorbed surface water and hydroxyls. The adsorbed water layers contain 16±4% of the total tritium inventory present in these samples. Measurements from the set of samples discussed in Fig. 153.39 showed that the adsorbed water layer contained 21±6%. The measurements from both data sets are equal within the experimental errors.

While the pulsed-plasma and $ZnCl_2$ methods extracted similar quantities of presumably surface-adsorbed tritium, the subsequent thermal desorption measurements performed on samples exposed to the pulsed plasma showed systematically less residual tritium presumably removed from bulk of the samples. The consistently lower tritium quantities obtained from thermal desorption are likely due to unaccounted losses occurring during the transfer of the samples from the plasma chamber to the thermal desorption oven. These low-yield samples were exposed to laboratory air for longer periods than after the $ZnCl_2$ treatment. For this reason, the means calculated in Fig. 153.40 do not include the pulsed-plasma radio-frequency (rf) data.

Figure 153.40 also shows that there is no measurable redistribution of tritium between the surface and bulk over the 42-day storage period. While it is reasonable to assume that Fickian diffusion is taking place within the metal bulk, it is clear that a significant number of surface-bound tritons are not entering the metal lattice, even though the tritium concentration on the surface is significantly larger than that in the bulk of the metal. It is evident, however, that the rate of tritium migration from the surface into the metal lattice at room temperature is very slow and does not depend on lattice diffusivity of tritium in bulk stainless steel. Acid etching is needed to determine the concentration profiles in the bulk and the influence of storage time on these profiles.

The total amount of tritium collected from the bulk of 316 stainless steel suggests that tritium retention at defect sites within the metal lattice dominate lattice solubility. For the loading conditions presented here and using solubility and diffusivity frequency factors and activation energies for tritium in 316 stainless steel compiled for higher temperatures[20] and extrapolated to room temperature, the samples are expected to contain ~0.5 mCi after a 24-h room-temperature exposure to tritium if the semi-infinite diffusion equation applies. However, the data shown in Figs. 153.38 and 153.40 demonstrate that 3 to 4 mCi are present. Defect sites, grain boundaries, vacancies, etc., increase the effective solubility of the metal about eightfold above that predicted by measurements at the higher temperatures.

Conclusions

The partition of tritium between the near surface and the bulk for 316 stainless-steel samples has been measured after exposure to tritium gas at room temperature. Pulsed-plasma exposures and a $ZnCl_2$ wash surface treatment were used to remove tritium present in the water layers of the surface. Thermal desorption provided a good measure of the residual tritium in the bulk metal lattice. Several conclusions were made based on the data:

- The $ZnCl_2$ wash treatment and pulsed-plasma exposures provide independent techniques to release and measure the quantity of tritium within the adsorbed water layers. Both methods extract similar amounts of tritium from the adsorbed surface water layers.

- The quantity of surface-adsorbed tritium accounts for 17% to 20% of the total inventory absorbed by a stainless-steel sample after a 24-h exposure to DT gas at room temperature. This result agrees with published data[4] obtained by acid etching.

- Redistribution of tritium between the surface and the bulk of stainless steel, if it occurs, is very slow. Tritium does not appear to migrate into the metal bulk at a rate defined by lattice diffusivity.

ACKNOWLEDGMENT

This material is based upon work supported by the Department of Energy National Nuclear Security Administration under Award Number DE-NA0001944, the University of Rochester, and the New York State Energy Research and Development Authority.

REFERENCES

1. A. Perevezentsev *et al.*, Fusion Sci. Technol. **41**, 746 (2002).
2. Y. Torikai *et al.*, J. Nucl. Mater. **329–333**, 1624 (2004).
3. Y. Torikai *et al.*, Fusion Sci. Technol. **48**, 177 (2005).
4. R.-D. Penzhorn *et al.*, J. Nucl. Mater. **353**, 66 (2006).
5. Y. Torikai *et al.*, J. Nucl. Mater. **363–365**, 462 (2007).
6. S. Naoe *et al.*, Fusion Sci. Technol. **54**, 515 (2008).
7. R.-D. Penzhorn *et al.*, Fusion Sci. Technol. **64**, 45 (2013).
8. P. Weinhold *et al.*, J. Nucl. Mater. **93–94**, 866 (1980).
9. W. T. Shmayda, F. Waelbroeck, J. Winter, P. Wienhold, T. Banno, and N. P. Kherani, Fusion Technol. **8**, 2285 (1985).
10. T. Hirabyashi, M. Saeki, and E. Tachikawa, J. Nucl. Mater. **127**, 187 (1985).
11. N. M. Masaki, T. Hirabayashi, and M. Saeki, Fusion Technol. **15**, 1337 (1989).
12. K. Isobe *et al.*, Fusion Sci. Technol. **54**, 553 (2008).
13. Y. Ozeki *et al.*, Fusion Sci. Technol. **60**, 1499 (2011).
14. Q. Li *et al.*, Int. J. Hydrog. Energy **40**, 6459 (2015).
15. C. Fagan, M. Sharpe, W. T. Shmayda, and W. U. Schröder, Fusion Sci. Technol. **71**, 275 (2017).
16. P. A. Thiel and T. E. Madey, Surf. Sci. Rep. **7**, 211 (1987).
17. T. Ohmi *et al.*, Rev. Sci. Instrum. **64**, 2683 (1993).
18. T. Shiraishi, S. Odoi, and M. Nishikawa, J. Nucl. Sci. Technol. **34**, 687 (1997).
19. M. Nishikawa *et al.*, J. Nucl. Mater. **227**, 99 (2000).
20. M. Sharpe, W. T. Shmayda, and W. U. Schröder, Fusion Sci. Technol. **70**, 97 (2016).
21. Y. Tanaka *et al.*, Mater. Trans. **49**, 805 (2008).
22. W. T. Shmayda, M. Sharpe, A. M. Boyce, R. Shea, B. Petroski, and W. U. Schröder, Fusion Sci. Technol. **68**, 766 (2015).
23. K. Röttger *et al.*, Acta. Cryst. **B68**, 91 (2012).
24. R. Schwartz, Metrologia **31**, 117 (1994).
25. M. Troy and J. P. Wightman, J. Vac. Sci. Technol. **8**, 515 (1971).

Experimental Signatures of Laser Wakefield Acceleration Assisted by Direct Laser Acceleration

Introduction

As the field of laser wakefield acceleration (LWFA)[1] matures, emphasis is shifting toward utilizing LWFA as a source of electron beams and x rays for certain applications. There is an increasing emphasis on producing electron beams from LWFA's that can meet the stringent beam requirements (narrow divergence, small emittance, and narrow energy spread) necessary for use in staged plasma accelerators[2] and free electron lasers. Simultaneously, betatron x rays from LWFA are being utilized for applications,[3–7] which places an emphasis on optimizing LWFA to produce these x rays. Even though these applications require optimization of different electron-beam properties, all applications benefit from a more-complete understanding of the dynamics of electron energy gain in LWFA and how those dynamics affect properties such as electron-beam energy, divergence, source size, shape, and energy spread.

For the range of plasma densities (mid-10^{18} to a few 10^{19} cm^{-3}) and laser pulse durations (35- to 45-fs FWHM) that are typically used in many current LWFA experiments in the forced or quasi-blowout regimes, the laser pulse length is of the order of the wake's wavelength; therefore it may occupy the entire first bucket of the wake. In such experiments, the wakefield structure has a desirable transverse and longitudinal field structure for generating a self-injected electron bunch, but it also has the necessary conditions for direct laser acceleration (DLA)[8,9] if there is an overlap between the accelerating electrons and the transverse electric field of the laser pulse.[10–16] It is therefore important to understand the role that not only the longitudinal electric field of the wake but also the other fields—namely, the transverse fields of the ion column and of the laser itself—play in determining the ultimate energy gained by the electrons. In this article we show, through experiments, the direct, observable signatures in the produced electron beams that indicate that DLA makes a significant contribution to the electrons' energy in LWFA's operated in such a configuration. Three-dimensional (3-D) particle-in-cell (PIC) simulations are used to elucidate the energy dynamics that lead to this contribution.

Background

In the matched, self-guided[17] blowout regime of LWFA,[18] an ultrashort, intense laser pulse propagates through either an underdense plasma or a neutral gas. In the latter case, the leading edge of the laser pulse ionizes the neutral gas, and the pondermotive force of the laser then expels the plasma electrons out and around the main body of the pulse. On the femtosecond time scale of the laser, the more-massive ions remain relatively immobile, so an ion column forms behind the drive laser. The expelled plasma electrons are drawn back to the laser axis by the Coulomb force of the ion column, where they overshoot and oscillate about the axis and thereby set up a wake structure. The charge separation generated by this wake structure produces a longitudinal electric field that is capable of accelerating electrons trapped in the wake at gradients >1 GeV/cm. Those electrons that are injected off-axis will undergo betatron oscillations in response to the linear transverse focusing force of the ions.[19,20]

Electrons can become trapped in a LWFA by a variety of methods,[21–31] but in the experiments and simulations presented here, the ionization injection[32–34] technique is used. In this technique, the plasma is produced by the laser ionization of a neutral gas mixture comprised of a gas with a low ionization potential (commonly He or H_2) doped with a gas with high ionization potential (commonly N_2 or Ar). The lower-intensity front edge of the laser pulse ionizes the outer (typically L) shell electrons of the dopant gas along with all the electrons in the gas with a low ionization potential. Because the inner (typically K) shell electrons of the higher-Z atoms have a much higher ionization potential, they are ionized only near the peak of the laser pulse within a fully formed wake and are subsequently trapped without slipping all the way to the back of the wake. Compared to self-trapping, this method of ionization injection permits trapping in a LWFA at reduced plasma densities and laser powers.

In a LWFA operating in the forced or quasi-blowout regime, the ion column acts as a very strong wiggler. Trapped electrons that are being accelerated by the wake undergo betatron oscillations in response to the transverse electric field of the ion column. Therefore, if a LWFA is configured such that some of the trapped electrons undergo betatron oscillations in the plane of polarization of the laser's electric field, the transverse field of the drive laser can give the electrons additional transverse momentum. This transverse momentum can then be converted to longitudinal momentum via the $\mathbf{v} \times \mathbf{B}$ force. In this way, the DLA mechanism[8,9] can accelerate electrons by this coupling of the transverse field of the laser through the betatron motion of the electrons. As a result, those electrons can potentially be accelerated by the DLA mechanisms in addition to the LWFA mechanism in a LWFA where the drive laser overlaps the trapped electrons.[10–16]

It has been noted that DLA is the inverse of the ion channel laser mechanism.[35] DLA in LWFA is also similar to inverse free electron laser (IFEL) acceleration,[36,37] except that the static magnetic undulator used in an IFEL is replaced by the transverse electric field of the ions in DLA and the resonance condition need not be strictly obeyed as in the IFEL.[11,13,14] In principle, the resonance condition for DLA is similar to that for an IFEL;[38] i.e., in an ideal situation, the laser pulse overtakes the electrons by one wavelength per betatron oscillation once the electrons come into resonance with the fundamental ($N = 1$) harmonic, where the electrons are bunched on a laser-wavelength scale.[8,39–42] Unlike in an IFEL, however, sustained resonance for DLA is more difficult to design because in the latter case, the normalized undulator strength $K \gg 1$ and the energy and betatron frequency of the electrons as well as the laser properties are continuously and rapidly changing.[11,13,14]

The condition for energy gain from the DLA mechanism is typically expressed using the 1-D resonance condition for a single electron:[8,9]

$$N\omega_\beta = \left(1 - \frac{v_{\|}}{v_\phi}\right)\omega_0, \tag{1}$$

where N is an integer indicating the harmonic of the betatron frequency,

$$\omega_\beta = \frac{\omega_\mathrm{p}}{\sqrt{2\gamma}}, \tag{2}$$

$v_{\|}$ is the velocity of the electron in the longitudinal direction, and v_ϕ and ω_0 are the phase velocity and frequency, respectively, of the electromagnetic wave (i.e., laser). Essentially, this resonance condition means that in order for an electron to gain energy from DLA, a harmonic of the betatron frequency $N\omega_\beta$ must equal the Doppler-shifted laser frequency $\left(1 - v_{\|}/v_\phi\right)\omega_0$ witnessed by the electron.[8,9,11,13,14] It is well known that in LWFA's, especially those not in the ideal blowout regime,[18] the properties of the drive laser, including ω_0 and v_ϕ, evolve throughout the acceleration distance. Furthermore, as electrons are accelerated in a LWFA, their longitudinal momentum, and therefore $v_{\|}$, increases and their betatron frequency is expected to fall as $\gamma^{-1/2}$ as seen in Eq. (2). Despite these evolving quantities, electrons that are being accelerated in a LWFA are able to gain significant energy from DLA because the quantities evolve together such that a quasi resonance is set up and the electrons are in a phase where they gain energy from the DLA mechanism for more than one-half of each betatron cycle.[11,13,14]

To determine if a LWFA is operating in a regime where DLA is expected to contribute to the energy gain of the electrons, the LWFA can be characterized using the ratio of the laser pulse length τ_laser relative to the nonlinear plasma wavelength Λ_wake. This ratio can be represented by the dimensionless pulse-length parameter[13,14]

$$T_\mathrm{p} = \frac{c\tau_\mathrm{laser}}{\Lambda_\mathrm{wake}} = \frac{\omega_\mathrm{p}\tau_\mathrm{laser}}{\left(2\pi a_0^{1/2}\right)}. \tag{3}$$

If the laser pulse length $c\tau_\mathrm{laser}$ is equal to the a_0-dependent length of the first bucket[18] $\Lambda_\mathrm{wake} \simeq \sqrt{a_0}\left(2\pi/k_\mathrm{p}\right)$, then $T_\mathrm{p} = 1$. Here, $k_\mathrm{p} = \omega_\mathrm{p}/c$ and a_0 is the normalized vector potential

$$a_0 = \frac{eE_0}{mc\omega_0} \simeq 8.6 \times 10^{-10}\sqrt{I_0\left(\mathrm{W/cm^2}\right)}\,\lambda(\mu\mathrm{m}),$$

where I_0 is the laser intensity and λ is the wavelength of the laser. In the case where T_p is 0.5 or less, the laser does not overlap the trapped electrons in the LWFA while they are being accelerated; those electrons gain energy purely from the longitudinal wakefield.[10,13,14] When T_p reaches 0.6 or more, the laser pulse will overlap the trapped electrons, and DLA can play a role in the acceleration of those electrons.[10,13,14] A $T_\mathrm{p} > 1$ indicates a significant overlap between the transverse laser field and the trapped electrons.[13,14]

Experimental Methods and Results

In this section, we show definitive experimental evidence of the presence of DLA in nonlinear LWFA's where the laser pulse overlaps the trapped electrons. We first demonstrate that the electron beams are indeed interacting with the drive laser when there is an overlap between the laser and trapped electrons, as might be expected in a DLA-assisted LWFA experiment. We then show that the transverse structure of the dispersed electron beams exhibits characteristic features that are indicative of DLA as an additional acceleration mechanism.

The experiments presented here were conducted at UCLA using an 815-nm Ti:sapphire laser with a fixed pulse length τ_{laser} of 45±5-fs FWHM of intensity and a spot size w_0 of 6.7 μm. The laser was run with powers P up to 10 TW, which correspond to an a_0 up to 2.6. An *f*/6 off-axis parabola (OAP) system focused the main laser pulse at the entrance of a variable-length (0.1- to 2-mm) gas cell[43,44] as shown in Fig. 153.41. The gas cell was filled with a 95% He/5% N_2 neutral gas mixture using a pulsed solenoid valve. The gas mixture was used so that ionization injection[32] could be used to inject the charge early into the wake and increase the amount of trapped charge. The plasma density was measured on every shot using a Michelson interferometer and was varied by changing the gas pressure.[43,44] The produced electron beams were dispersed in energy with a 0.92-T dipole magnet onto a plastic scintillator or a LANEX screen and recorded using a PI-MAX intensified charge-coupled–device (CCD) camera. This electron spectrometer could be rotated by 90° so that the electron beam could be dispersed parallel to or orthogonal to the linear laser polarization.[13,14]

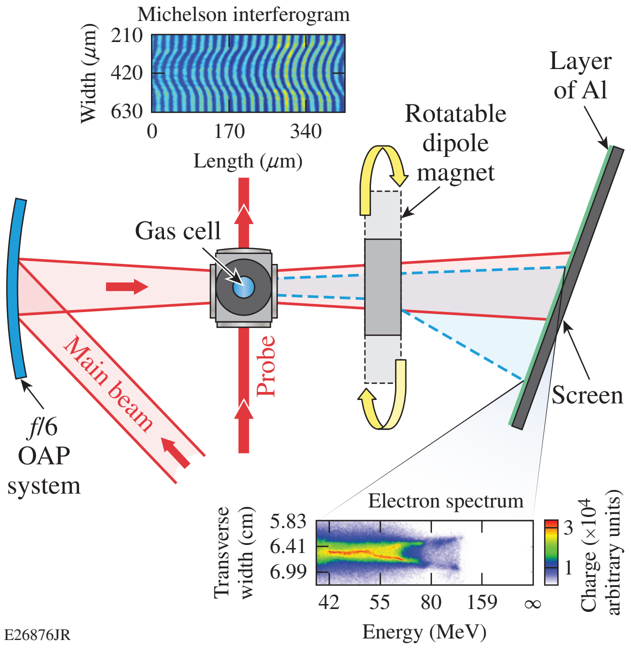

Figure 153.41
Experimental setup. The red-shaded area shows the main laser pulse being focused by the *f*/6 off-axis parabola (OAP) system at the entrance of the gas cell. The laser is linearly polarized in the plane of the page. The thick red line shows the probe for the Michelson interferometer. A typical interferogram is shown. The electrons are dispersed by the 0.92-T dipole magnet onto a scintillator or a LANEX and imaged by a PI-MAX 3 camera. The dipole magnet and screen could be rotated by 90° so that the electron beams could be dispersed parallel or orthogonal to the laser polarization. The dipole magnet typically was located 3.2 cm downstream from the gas cell, and the distance from the end of the magnet to the screen was 7.0 cm. A typical measured electron spectrum is shown.

Because the energy gain from DLA relies on the coupling between the transverse laser field and the betatron motion of the electrons, the first observable signature of an interaction between the laser and the trapped electrons in a LWFA is that the undispersed electron beam should be elliptical in the direction of the laser polarization.[45] The white ellipses in Fig. 153.42(a) are fits to the 50% contour of the undispersed electron beams from ten consecutive shots where the laser had horizontal, linear polarization and a vacuum a_0 of ~1.5. The

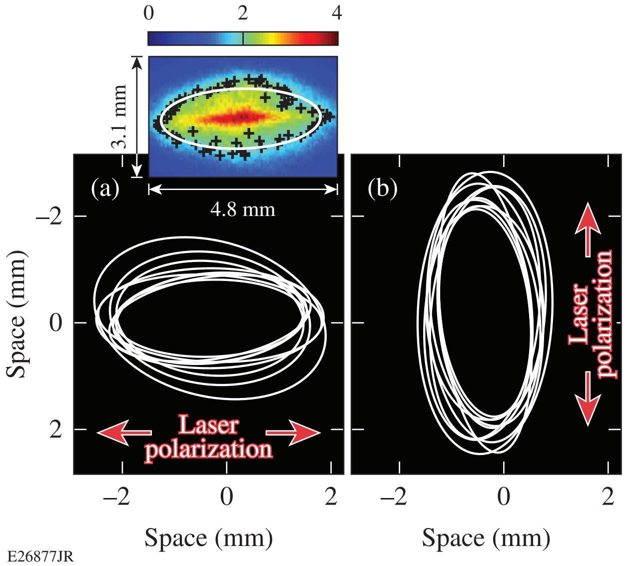

Figure 153.42
[(a),(b)] Fits (white ellipses) to the 50% contour of undispersed electron beams from a series of nine and ten, respectively, consecutive laser shots when using horizontal and vertical, respectively, linear laser polarization. (Inset) Typical undispersed electron beam from data shown in (a) with 50% contour points marked by the black crosses and the fit to that point marked by the white ellipse.

plasma density was ~1.7×10^{19} cm^{-3}, which yields a T_p value of ~1.3, and the gas cell length was 900 μm. The fits show a strong ellipticity in the direction of the laser polarization with an average measured half-width-at-half-maximum (HWHM) divergence of 12.2 mrad. In contrast, the average measured HWHM divergence in the perpendicular direction was 5.6 mrad. The direction of the linear polarization of the drive laser was then rotated 90° using a thin (1-mm) quartz half-wave plate for high-laser-energy applications. The ellipticity of the undispersed electron beams rotated with the laser polarization, as shown in Fig. 153.42(b), which indicates that the trapped electrons' transverse momentum is being enhanced in the polarization plane. With the vertical laser polarization, the average measured HWHM divergence in the direction of the laser polarization was 13.0 mrad, and the average measured HWHM divergence in the perpendicular direction was 6.5 mrad. Therefore, under the laser-plasma parameters described above, the measured divergence of undispersed electron beams emanating from the LWFA shows ellipticity that is correlated to the polarization of the laser pulse. This correlation demonstrates that the electrons are indeed interacting with the drive laser. Although DLA is expected to preferentially increase the divergence of the electron beam in the plane of the laser polarization, the observed ellipticity in the divergence of the undispersed electron beams in Fig. 153.42 in itself is not definitive proof that DLA is present in the LWFA.[13] Rather, because the energy gain from DLA relies on the coupling between the transverse laser field and the betatron motion of the electrons, a signature of this transverse coupling must be present in the energy gain of the electrons to demonstrate the presence of DLA in LWFA.

Because DLA is an additional energy gain mechanism on top of the energy gained from the wakefield, if it is present in the system, the highest-energy electrons should also have the largest divergence. Figure 153.43 shows two examples of the experimental electron spectra when the electrons were dispersed in the (a) same and (b) orthogonal plane of the laser polarization for similar experimental parameters. When dispersed in the direction of the laser polarization, the measured electron-beam spectra exhibited a narrower divergence than when it was dispersed orthogonal to the direction of the laser polarization. An example of the former is shown in Fig. 153.43(a), where the electron beam has an average measured HWHM divergence of 4.3 mrad for electron energies >40 MeV. The continuous energy spread is characteristic of ionization injection.[32,34] When the electron beams were dispersed perpendicular to the laser polarization, however, they had a much larger divergence and additionally split at the highest electron energies, resulting in a forked structure. This behavior of the dispersed electron beam is shown in Fig. 153.43(b), where the average measured divergence increased to 11.8 mrad and the forked structure is clearly visible above 90 MeV. The divergence was calculated using the HWHM for electron energies below 90 MeV and the fork centroid for energies above 90 MeV, which is where the fork structure begins. Such a clear fork structure, partial fork structures, or modulations have been observed in experimental electron spectra for plasma densities between 0.9 and 1.6×10^{19} cm^{-3} (T_p = 0.8 to 1.4) as shown in Fig. 153.44. The transverse shape of the spectrum in Fig. 153.43(b) clearly transitions from a center-peaked distribution to the forked structure. In the center-peaked distribution, the electrons gain the majority of their energy from LWFA and can originate from the first and subsequent buckets, in which the laser does not overlap the electrons. The electrons in the forked region of the spectrum originate in the first bucket of the wake and gain a majority of their energy via DLA, as will be shown in the next section.

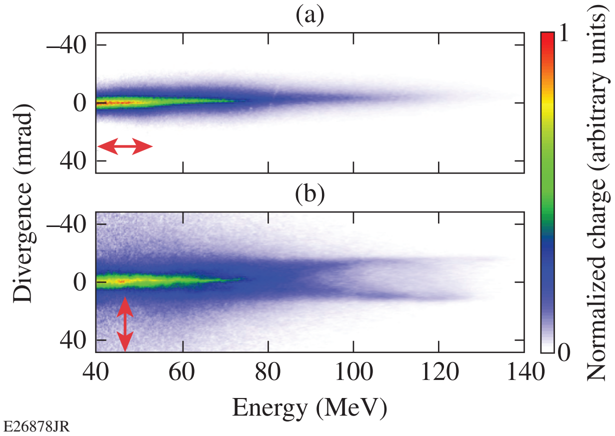

Figure 153.43
[(a),(b)] Experimental electron spectra dispersed parallel and perpendicular, respectively, to the laser polarization (red arrows). The experimental parameters for the shot shown in (a) and (b) are gas cell length = 800 and 900 μm, $n_e = 1.7 \times 10^{19}$ and 1.4×10^{19} cm^{-3}, a_0 = 2.0 and 1.9, and T_p = 1.1 and 1.1, respectively.

Simulation Methods and Results

To interpret the features observed in experiment, a series of 3-D simulations using the PIC code *OSIRIS* 3.0 (Ref. 46) were conducted. These simulations modeled the above experimental parameters and employed particle tracking to elucidate the roles of LWFA and DLA to the energy gain of the electrons in this experimental regime. The spectral features indicating if DLA is present in a LWFA are best illustrated by comparing a

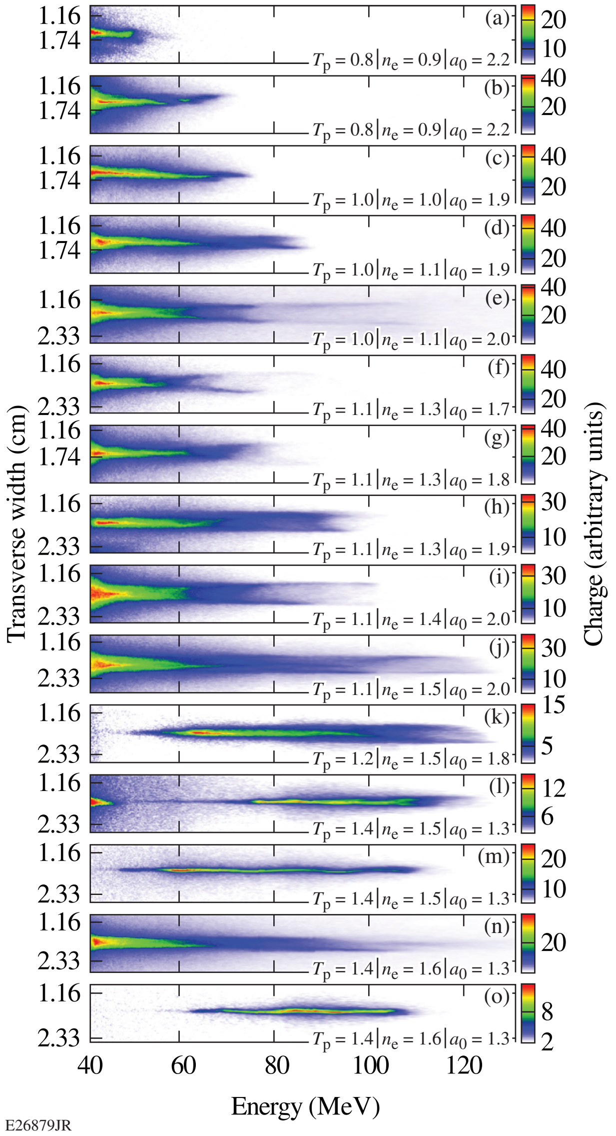

Figure 153.44
A series of electron spectra with fork features or modulated spectra taken on a single shot day. Data are sorted by ascending T_p values. The gas cell length was 900 μm. At the highest densities of 1.5 to 1.6 × 10^{19} cm^{-3}, even though $T_p > 1$, the fork structure disappears as a_0 is reduced to 1.3, thereby switching off ionization injection.

simulation where T_p is 0.4 (no overlap between the laser and the trapped electrons) and a case where T_p is 0.8 (drive laser is filling nearly the entire first period of the wake and overlapping the trapped electrons). DLA is expected in the $T_p = 0.8$ case.[10,13,14] Both simulations were run with identical parameters except for the laser pulse lengths. The laser ionized an initially neutral gas comprised of 99.9% He and 0.1% N_2 to produce a plasma density of 8 × 10^{18} cm^{-3}. The Ammosov–Delone–Krainov[47] ionization model was used. The resulting plasma consisted of a 1-mm-long plateau region with 100-μm-long linear density up- and down-ramps. The linearly polarized drive laser had an a_0 of 2.1 and was focused to a spot size of 6.7 μm halfway up the density up-ramp. For the $T_p = 0.4$ case, the pulse length was 25 fs; for the $T_p = 0.8$ case, the pulse length was 45 fs. For both simulations, the grid was 1940 × 320 × 320 with 2 × 2 × 2 particles per cell and $k_0\Delta z = 0.209$ and $k_p\Delta x,\Delta y = 0.090$. The resulting normalized time step was 0.01403.

Each simulation was run once to completion; then the 20 highest-energy electrons and >500 random electrons were tagged. The simulations were then rerun while tracking the tagged particles to determine their position, momentum, and the fields that they sampled at each time step of the simulation. With that information, the relative contributions to the total energy gain of each electron resulting from the transverse electric field and the longitudinal electric field can be calculated. The relative contribution $W_{||}$ caused by the longitudinal electric field $\mathbf{E}_{||}$ was calculated using

$$W_{||} = -e\int_0^t \mathbf{E}_{||} \cdot \mathbf{v}_{||}\mathrm{d}t'. \tag{4}$$

The dominant longitudinal electric field is the wakefield; therefore, this value will be called the "LWFA contribution" to the final electron energy. Similarly, the relative contribution $W_\perp$ caused by the transverse electric field $\mathbf{E}_\perp$ was calculated using

$$W_\perp = -e\int_0^t \mathbf{E}_\perp \cdot \mathbf{v}_\perp \mathrm{d}t', \tag{5}$$

where $\mathbf{v}_\perp$ is the transverse velocity of the electron. The dominant transverse electric field is the transverse laser field, so this value will be called the "DLA contribution" to the final electron energy.

In the $T_p = 0.4$ case, LWFA is expected to be the only acceleration mechanism. Figure 153.45(a) shows that, indeed, DLA plays a negligible role in the energy gained by the electrons when there is no overlap between the laser and the trapped electrons. Of the 550 randomly selected electrons, the maximum DLA contribution as calculated using Eq. (5) is 1.5 MeV, and DLA accounts for no more than 1.5% of the final energy of any of the randomly tagged electrons. In the $T_p = 0.8$ case, the drive laser now overlaps the trapped electrons and some contribution from DLA is expected in addition to LWFA. Figure 153.45(b) shows that although the maximum electron energy is reduced, DLA plays a significant role in the energy gained by the electrons. For the 1080 randomly selected electrons, the maximum DLA contribution to the final electron energy is up to 50 MeV, and up to ~50% of the electrons' total energy can be attributed to DLA, which shows that the DLA mechanism can provide comparable energy to the LWFA mechanism.

If DLA contributes significantly to the energy gain of the electrons produced from a LWFA, those electrons should have increased transverse momentum in the direction of the laser polarization. This increased transverse momentum should show up as an ellipticity of the produced electron beam in the direction of the laser polarization. Figure 153.46 compares the projected divergence for (a) the $T_p = 0.4$ and (b) the $T_p = 0.8$

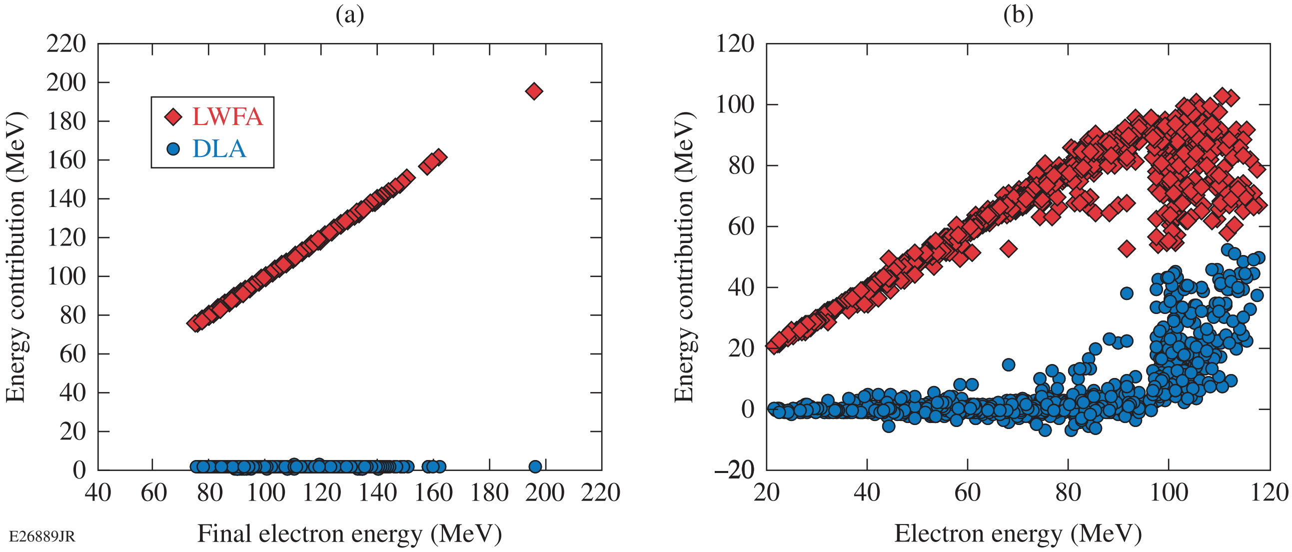

Figure 153.45
Plots of the DLA contribution $W_\perp$ (blue circles) and the LWFA contribution $W_\parallel$ (red diamonds) to the final energy of each electron versus its final energy for (a) the 550 random electrons in the $T_p = 0.4$ case and (b) the 1080 random electrons in the $T_p = 0.8$ case.

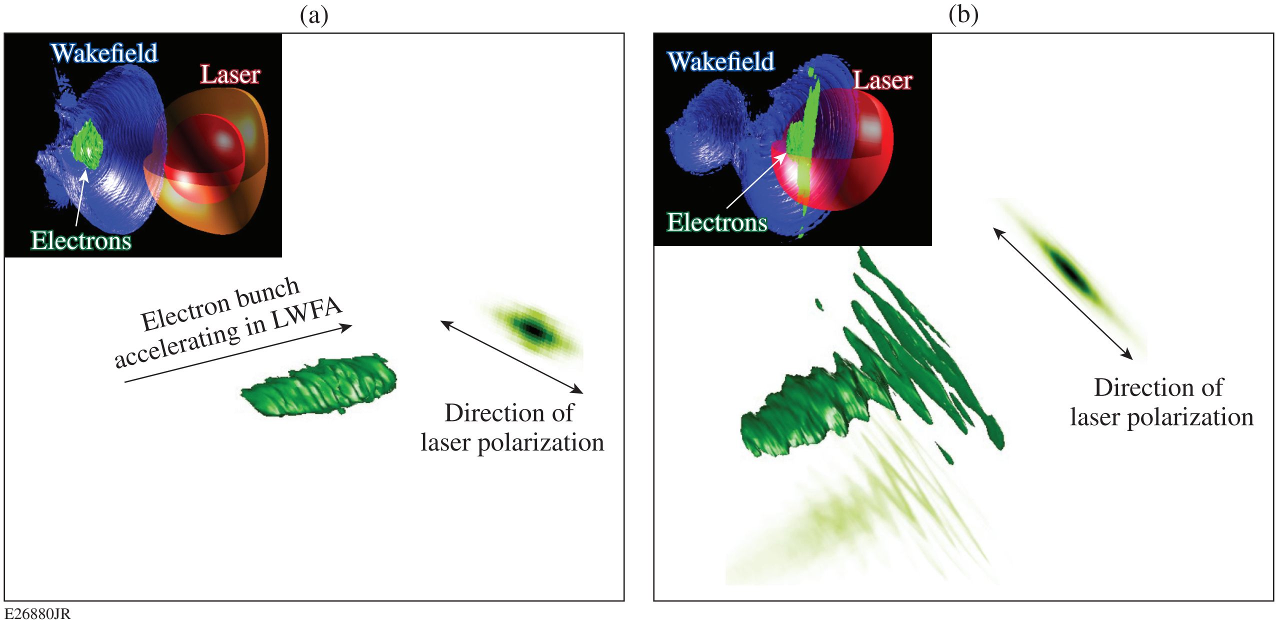

Figure 153.46
Contour plots of electron bunch (green) propagating in a 3-D *OSIRIS* simulation (left) and projection of that electron bunch onto a screen (right) for (a) the $T_p = 0.4$ simulation and (b) a $T_p = 0.8$ simulation. Insets show snapshots of the electron bunch as it is accelerated in the LWFA. Note that the laser overlaps the trapped electrons in the $T_p = 0.8$ case.

cases. In the $T_p = 0.4$ case, the inner-shell nitrogen electrons were ionized within the laser pulse and then escaped the laser to become trapped in the back of the wake, which causes the initial transverse momentum that they gain from the laser[13] to become apparent. In this case, the projection of the accelerated electrons on a screen [Fig. 153.46(a)] shows an elliptical beam with an rms divergence of 8.6 mrad along the major axis, which is in close agreement with estimations of the maximum transverse momentum an electron acquires from the tunnel ionization process.[13] In the case of $T_p = 0.8$, the ionized electrons remain within the laser field and gain energy from both LWFA and DLA. These electrons also show an elliptical beam when projected onto a screen [Fig. 153.46(b)]. Its rms divergence along the major axis is 24.8 mrad, which is nearly 3× as large as in the $T_p = 0.4$ case, where LWFA is the only acceleration mechanism. Although both simulations produce an elliptical beam, the observation of increased divergence in the $T_p = 0.8$ case is qualitatively consistent with expectations if DLA is present as an additional acceleration mechanism.

If LWFA is the only acceleration mechanism, the divergence of the produced electron beam should be relatively constant as a function of energy regardless of the direction of the dispersion of the electron beam. Figure 153.47(a) shows the electrons dispersed in the direction of the laser polarization for the $T_p = 0.4$ case. The resulting electron spectrum has a narrow divergence that is peaked on axis. When the electrons are dispersed orthogonal to the laser polarization [Fig. 153.47(b)], the divergence remains relatively narrow and is still peaked on axis. Such narrow divergence is consistent with LWFA being the only acceleration mechanism. To further illustrate this point, in Fig. 153.47(c), the 550 randomly tagged electrons color coded by their energy gain from DLA are plotted on a contour plot of Fig. 153.47(b). This figure shows that the maximum DLA contribution is only 1.5 MeV and that there is no correlation between the amount of energy contributed by DLA and the divergence of the electron beam.

DLA arises because of an increase in the transverse momentum of the electron caused by work done by the transverse laser field. Because DLA is an additional energy gain mechanism on top of the energy gained from the wakefield, if it is present in the system, the highest-energy electrons should also have the largest divergence. Nonetheless, as Fig. 153.47(d) shows, even in the

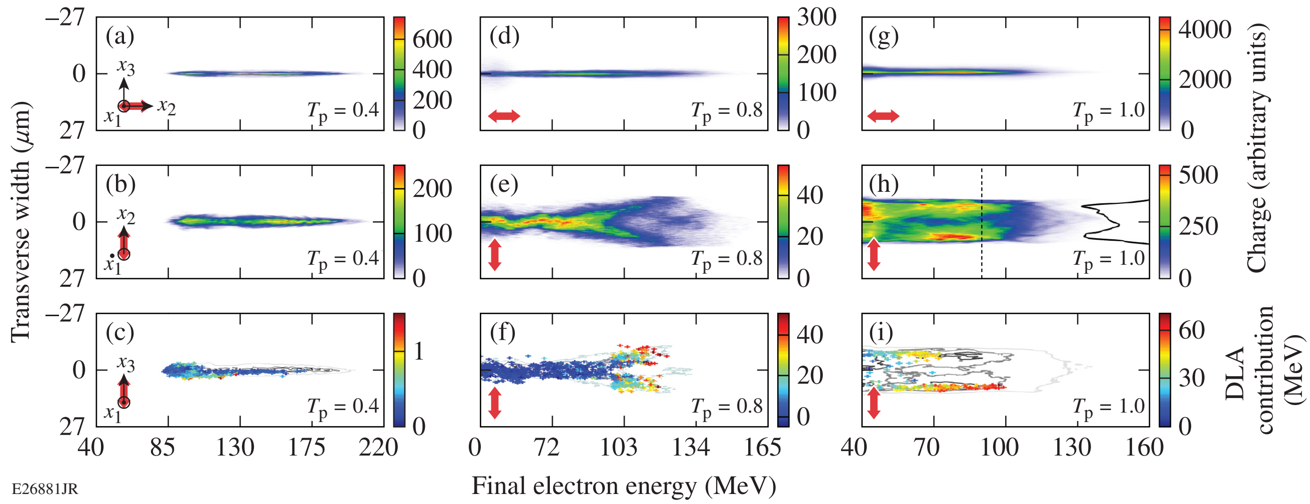

Figure 153.47
Simulated electron spectrum dispersed (a) parallel and (b) orthogonal to the linear laser polarization (red arrows) for the $T_p = 0.4$ simulation. (c) Contour plot of (b) showing the 8% (light gray line), 40% (dark gray line), and 60% (black line) contours. The colored points represent the 550 randomly tagged electrons with energies over 40 MeV and are color coded by their DLA contribution. Simulated electron spectrum dispersed (d) parallel and (e) orthogonal to the linear laser polarization for the $T_p = 0.8$ simulation. (f) Contour plot of (e) showing the 18% (light gray line), 44% (dark gray line), and 74% (black line) contours. The colored points represent the 1080 randomly tagged electrons with energies over 40 MeV and are color coded by their DLA contribution. Simulated electron spectrum dispersed (g) parallel and (h) orthogonal to the linear laser polarization from the $T_p = 1.0$ simulation. The black curve shows the lineout of the forked structure at 90 MeV, which is marked by the vertical dashed black line. Parameters for this simulation were $a_0 = 2.03$, $\tau_{\text{laser}} = 45$ fs, $\lambda_0 = 815$ nm, $w_0 = 6.7\ \mu$m, $n_e = 1.43 \times 10^{19}$ cm^{-3}, plasma length = 430 μm with 100-μm up-ramps and 150-μm down-ramps. The grid was 1814 × 320 × 320 with 2 × 2 × 2 particles per cell and $k_0\Delta z = 0.209$ and $k_p\Delta x,\Delta y = 0.120$. The resulting normalized time step was 0.01877. (i) Contour plot of (h) showing the 4% (light gray line), 35% (dark gray line), and 61% (black line) contours. The colored points represent the 550 randomly tagged electrons with energies over 40 MeV and are color coded by their DLA contribution.

$T_p = 0.8$ case where DLA is expected to contribute to the energy gain, if the electrons are dispersed in the direction of the laser polarization, the spectrum still features a narrow divergence that is peaked on axis. If the electron beam is dispersed in the same direction as the laser polarization, any structure associated with the enhanced oscillation of the electrons in the direction of the laser polarization cannot be discerned. When the electron beam is dispersed orthogonal to the direction of the laser polarization, however, Fig. 153.47(e) shows that the divergence increases with the total energy of the electrons and, at an energy of ~95 MeV, the spectrum splits into a forked structure. In Fig. 153.47(f), the randomly tagged electrons with energies of 40 MeV and above are superimposed on a contour plot of the data shown in Fig. 153.47(e). These electrons are color coded by their DLA contribution to the final energies. Figure 153.47(e) shows that for final electron energies below ~95 MeV, where the transverse shape of the electron spectrum is peaked on axis, the DLA contribution to the final electron energies is small (15 MeV or less). Rather, the center-peaked charge at lower energies, which was also seen in the experimental data in Fig. 153.43(b), is predominately accelerated by the wake. Beginning at final electron energies of ~95 MeV, the DLA contribution to the electron energy increases, and the electron spectrum splits into a forked structure similar to the one seen in the experimental data [Fig. 153.43(b)]. The electrons that fall within the fork structure have the highest DLA contributions; as a result, the change in divergence with energy is a clear, observable signature that DLA is playing a role in the LWFA.

The degree of forking seen in the electron spectrum depends on the degree of overlap between the drive laser and the trapped electrons. The electron spectrum in Fig. 153.47(h) was produced from a 3-D *OSIRIS* simulation that had the same physical parameters as the $T_p = 0.8$ simulation, except that a_0 was 2.03, n_e was 1.43×10^{19} cm^{-3}, and the constant-density region of the plasma was 430 μm long. These parameters were chosen to model the experimental data shown in Fig. 153.43. Comparing the middle row of spectra in Fig. 153.47 shows that as the degree of overlap (i.e., T_p) is increased from $T_p = 0.5$ to $T_p = 1.0$, the extent of the forking increases and the forking descends deeper into the lower-energy portion of the electron spectrum. The increase in forking with T_p is caused by an increase in the DLA contribution relative to the LWFA contribution. As shown in Fig. 153.45, for the $T_p = 0.8$ case, the dominant energy contribution for the randomly selected electrons is from LWFA. Up until final electron energies of ~95 MeV, it is essentially the only mechanism contributing to the energy gain of the electrons; indeed, there is no forking of the electron spectrum [Fig. 153.47(e)] below these energies. The fork structure arises when DLA begins to make a sizeable contribution. At energies of ~95 MeV, DLA begins to contribute to the final energy gained by the electrons; it is at that energy that the spectrum begins to fork [Figs. 153.47(e) and 153.47(f)]. In comparison to the $T_p = 0.8$ case, for the 550 randomly selected electrons from the $T_p = 1.0$ case, even the lowest electron energies have significant energy contributions from DLA, and both DLA and LWFA are strongly contributing to the energy gain of the electrons, as seen in Fig. 153.48. The best linear fits through those contributions show that the curves intersect at 25 MeV. Below this energy, the final energy of the electrons is primarily dominated by LWFA, and above this energy, DLA becomes the dominant contribution; this is correlated with the strong forking observed in Figs. 153.47(h) and 153.47(i) (Refs. 13 and 14).

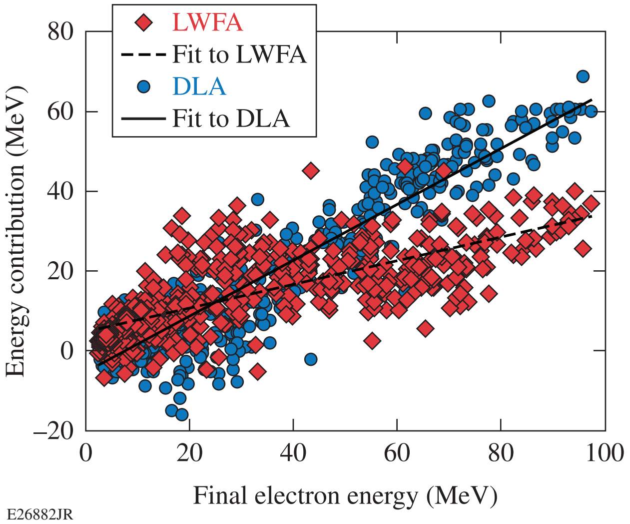

Figure 153.48
Plot of the DLA contribution $W_\perp$ (blue circles) and the LWFA contribution $W_\parallel$ (red diamonds) to the final energy of each of the 550 random electrons versus their final energies for the $T_p = 1$ simulation. The solid curve shows the best linear fit $E_{\mathrm{DLA}} = 0.70\ E_{\mathrm{final}} - 5.36$ (MeV) with an R^2 fit of 0.88 for the DLA contribution; the dashed curve shows the best linear fit $E_{\mathrm{LWFA}} = 0.30\ E_{\mathrm{final}} + 4.77$ (MeV) with an R^2 fit of 0.57 for the LWFA contribution.

The origin of the forked structure becomes evident when the transverse structure of the electron beam is examined. When DLA is present in a LWFA, the higher-energy electrons owe a significant portion of their energy to DLA. The head of the electron beam overlaps a high-intensity portion of the laser pulse and is strongly modulated at half of the laser wavelength,[48] and the charge is bunched at the extrema of the betatron oscillations as shown in Fig. 153.49(a). This bunching causes the charge at the front portion of the electron beam to exit the plasma with some transverse separation, which leads to the fork structure seen in

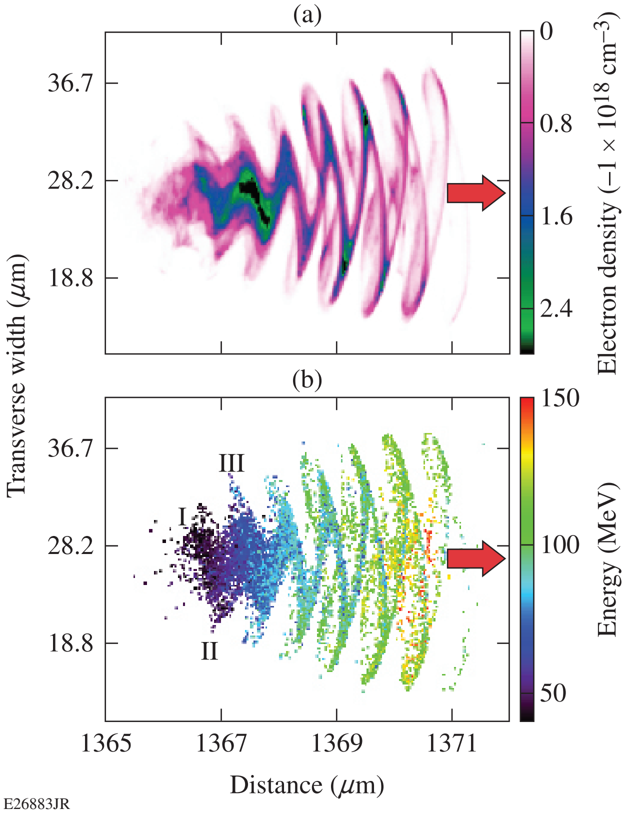

Figure 153.49
(a) Transverse density profile of electron beam after propagating 100 μm in vacuum from the T_p = 0.8 simulation used to generate Figs. 153.47(e) and 153.47(f). (b) Transverse profile of the same electron beam as in (a) showing a sampling of 0.04% of the total electrons in the simulation color coded by their final energy. The red arrows in both (a) and (b) mark the direction of the electron-beam propagation.

the middle and bottom rows of Fig. 153.47. The laser intensity falls from the head of the electron beam to its tail; consequently, the modulation at half of a laser wavelength becomes less pronounced and the charge is no longer bunched at the extrema of the betatron oscillations. At the tail of the electron beam, the energy contribution of DLA to the overall charge of the electrons is small, and there is only a small transverse modulation of the accelerated charge. Although this transverse modulation is small at the tail of the beam, it leads to the serpentine structure in the dispersed electron beam in the $T_p = 0.8$ case [Fig. 153.47(e)] for the lower electron energies (40 MeV to ~95 MeV).

In Fig. 153.49(b), the transverse structure of the electron beam is shown using a sampling of the electrons from the T_p = 0.8 simulation color coded by their final energy. Figure 153.49(b) shows that there is a general correlation between the position of the electrons in the beam and their final energies. The higher-energy electrons are predominantly found at the head of the electron beam, and the lower-energy electrons are predominantly found at the tail. For the lower-energy electrons, each half oscillation in the transverse structure contains electrons in different bins of final energies. For example, the charge slightly above the laser axis at the point marked “I” has final energies of ~40 MeV, the charge at “II” has ~50 MeV, the charge at “III” has ~70 MeV and so on. These steps in the final energy associated with a given transverse position mean that the different-energy electrons will exit the plasma with slightly different transverse positions and divergences, which produces the serpentine structure when the electron beam is dispersed orthogonal to the direction of the laser polarization as seen in the center-peaked electron feature for energies from 40 MeV to ~95 MeV in Fig. 153.47(e). This serpentine structure is absent when the electron beam is dispersed in the direction of the laser polarization, as seen in Fig. 153.47(d).

In addition to the serpentine structure in the dispersed spectrum for electron energies below ~95 MeV, Figs. 153.47(e) and 153.47(f) have a second small forked structure in the interior of the large fork at an energy of approximately 125 MeV. As already discussed, the main fork structure in Fig. 153.47 arises because the electrons are bunched at the extrema of their betatron oscillation and exit the plasma with a transverse separation but a small divergence. The secondary fork in Fig. 153.47 also arises because of the betatron motion of the electrons; however, this fork is formed differently. The electrons that form this fork are also executing large-radii betatron oscillations; however, they are phased one quarter of a betatron period from those that form the main fork. Therefore, unlike the electrons that form the main fork, which exit the plasma with a large transverse separation but small divergence, these electrons exit the plasma with a small transverse separation but with a large divergence. Because the electron-beam spectrum from the simulation is calculated 100 μm after the exit of the plasma, these electrons are captured as they cross the betatron axis due to their large divergence. Such electrons would not be captured in the experiment, however, because their divergence is so large that they would be lost during the transport to the detector.

Conclusions

In this article, the DLA of electrons in a LWFA operating in the forced or quasi-blowout regimes has been investigated through experiment and simulation. We have demonstrated that when there is a significant overlap between the trapped electrons and the laser ($T_p \sim 1$) in a LWFA cavity, the resulting electrons can gain energy from both the LWFA and the DLA mechanisms. In the experimental work, we investigated the properties of the electron beams produced in a LWFA with ionization injection by dispersing those beams in the direction perpendicular to the laser polarization. We found that these electron beams show certain features (ellipticity in the plane of the laser polarization and an energy spectrum that splits into a fork at higher energies when the beam is dispersed orthogonal to the laser polarization direction) that are characteristic of DLA. These characteristic spectral features were reproduced in *OSIRIS* simulations, where particle tracking was used to demonstrate that such spectral features are signatures of the presence of DLA in LWFA.

Supporting simulations modeled the experimental parameters and employed particle tracking to interpret these signatures and elucidate the roles of LWFA and DLA to the energy gain of the electrons in this experimental regime. The contribution of DLA to the energy gained by the electrons was calculated in simulations. Its magnitude was found to be of the order of the LWFA contribution and actually exceeded the LWFA contribution to the highest-energy electrons in some cases. It was also shown that in the LWFA's studied here, both DLA and LWFA can participate in accelerating the bulk of the electrons in the produced electron beam. The presence of DLA in a LWFA can lead to enhanced betatron oscillation amplitudes and increased divergence in the direction of the laser polarization.

The presence of DLA in LWFA provides insight into possible reasons why the overall quality (i.e., emittance, divergence, energy spread) of the electron beams produced from LWFA experiments is not always competitive with that from conventional radio-frequency accelerators. The energy gain from DLA relies on the coupling between the transverse laser field and the betatron motion of the electrons, which causes the transverse momentum of the electrons to be larger than in a LWFA-only case. This increased transverse momentum can lead to an increase in the divergence of the electron beam in the direction of the laser polarization. Additionally, because the energy gain due to DLA varies depending on the magnitude of the transverse laser field sampled by the electron as well as whether or not that electron is able to gain energy from DLA for extended acceleration distances, DLA can contribute to energy spread in LWFA systems such as those studied here. Understanding that DLA can play a role in LWFA systems may provide a path for such experiments to improve the emittance, divergence, and energy spread of their LWFA-produced electron beams if that is a major goal of such experiments.

In the future, the DLA process in LWFA could be optimized further. One potential path would be to tailor the laser profile to enhance the DLA. For example, the drive laser could be chirped so that the quasi resonance required for energy gain from DLA is better maintained.[8,9,11,13,14] The two-laser DLA scheme presented by Zhang *et al.*[15,16] could be tested experimentally to see if it permits better control of the DLA process in LWFA. The effect of ion motion on DLA in a LWFA could be explored through further simulations. Additionally, the gas mix used for ionization injection could be better tailored to trap a charge farther forward in the wake. Although such electrons would gain less energy from LWFA, they would overlap with a larger laser amplitude and, therefore, should gain more energy from DLA. DLA could also be explored in LWFA experiments that employ other injection schemes.[6,49] Finally, it would be very interesting to investigate whether DLA could be introduced in a beam-driven plasma wakefield accelerator (PWFA) cavity using an intense laser pulse that trails the particle bunch that drives the wake.

DLA also leads to an increase in the amplitude of the betatron oscillations of the electrons. The critical energy of the betatron x-ray spectrum emitted by electrons in a LWFA scales as $\gamma^2 r_0$, where r_0 is the amplitude of the betatron oscillation, and its radiated power scales as $\gamma^2 r_0^2$. The increase in r_0 resulting from DLA would increase the critical energy and the radiated power. Furthermore, the number of emitted photons scales as $\gamma^{1/2} r_0$ and should, therefore, increase with the enhanced r_0 from DLA. Therefore, DLA shows much promise as a path to enhancing the betatron radiation generated from LWFA's. In fact, the role of DLA in betatron x-ray production could have been inferred indirectly from the MeV photon emission observed in the forward direction in prior LWFA experiments.[50] The renewed interest in the betatron radiation from LWFA's operating in the self-modulated LWFA regime further motivates additional investigation into the role that DLA plays in betatron radiation.[6,51,52]

DLA can also be present in LWFA driven by circularly polarized lasers. Additional simulations (not included here) have shown that the presence of two transverse electric-field components can lead to continuous energy gain from the DLA mechanism and a correlated increase in the betatron oscillation radius. Furthermore, the degree of polarization of the betatron x rays produced from circularly polarized DLA-assisted LWFA may be tied to DLA's contribution to the electrons.[53]

Finally, DLA could also be exploited to microbunch electron beams on femtosecond to attosecond time scales.[48] When DLA is present in a LWFA, the electrons tend to bunch at the extrema of their large-radii betatron oscillations.[13,14] This bunching is spaced at half of the laser wavelength,[8,13,14,48] which can yield electron bunches with temporal durations ~1 fs for a LWFA driven by a Ti:sapphire laser. It may be possible to diagnose this bunching from the (coherent) optical transition radiation that these bunched beams may emit as they exit the plasma/vacuum boundary.

ACKNOWLEDGEMENT

This material is based upon work supported by the Department of Energy National Nuclear Security Administration under Award Number DE-NA0001944, the Department of Energy and National Science Foundation under grant DE-SC0017950, the University of Rochester, and the New York State Energy Research and Development Authority.

The work done at UCLA was supported by U.S. DOE grant DE-SC0010064 and National Science Foundation grant 1734315. N. L. acknowledges that this work was performed under the auspices of the U.S. Department of Energy by Lawrence Livermore National Laboratory under the contract DE-07NA27344, Lawrence Livermore National Security, LLC. J. L. acknowledges use of *OSIRIS* through the *OSIRIS* Consortium at UCLA and IST.

REFERENCES

1. T. Tajima and J. M. Dawson, Phys. Rev. Lett. **43**, 267 (1979).
2. W. Leemans and E. Esarey, Phys. Today **62**, 44 (2009).
3. J. M. Cole *et al*., Sci. Rep. **5**, 13,244 (2015).
4. S. Kneip *et al*., Appl. Phys. Lett. **99**, 093701 (2011).
5. F. Albert in *Frontiers in Optics 2015*, OSA Technical Digest (online) (Optical Society of America, San Jose, CA, 2015), Paper FTh4A.1.
6. N. Lemos *et al*., Plasma Phys. Control. Fusion **58**, 034018 (2016).
7. F. Albert *et al*., Plasma Phys. Control Fusion **56**, 084015 (2014) and references therein.
8. A. Pukhov, Z. M. Sheng, and J. Meyer-ter-Vehn, Phys. Plasmas **6**, 2847 (1999).
9. A. Pukhov, Rep. Prog. Phys. **66**, 47 (2003).
10. J. L. Shaw, F. S. Tsung, N. Vafaei-Najafabadi, K. A. Marsh, N. Lemos, W. B. Mori, and C. Joshi, Plasma Phys. Control. Fusion **56**, 084006 (2014).
11. J. L. Shaw, N. Vafaei-Najafabadi, K. A. Marsh, N. Lemos, F. S. Tsung, W. B. Mori, and C. Joshi, AIP Conf. Proc. **1777**, 040014 (2016).
12. J. L. Shaw, N. Lemos, K. A. Marsh, F. S. Tsung, W. B. Mori, and C. Joshi, Plasma Phys. Control. Fusion **58**, 034008 (2016).
13. J. L. Shaw, "Direct Laser Acceleration in Laser Wakefield Accelerators," Ph.D. thesis, University of California, Los Angeles, 2016.
14. J. L. Shaw, N. Lemos, L. D. Amorim, N. Vafaei-Najafabadi, K. A. Marsh, F. S. Tsung, W. B. Mori, and C. Joshi, Phys. Rev. Lett. **118**, 064801 (2017).
15. X. Zhang, V. N. Khudik, and G. Shvets, Phys. Rev. Lett. **114**, 184801 (2015).
16. X. Zhang *et al*., Plasma Phys. Control. Fusion **58**, 034011 (2016).
17. J. E. Ralph *et al*., Phys. Rev. Lett. **102**, 175003 (2009).
18. W. Lu *et al*., Phys. Rev. ST Accel. Beams **10**, 061301 (2007).
19. S. Wang *et al*., Phys. Rev. Lett. **88**, 135004 (2002).
20. A. Rousse *et al*., Phys. Rev. Lett. **93**, 135005 (2004).
21. J. Faure *et al*., Nature **444**, 737 (2006).
22. D. Umstadter, J. K. Kim, and E. Dodd, Phys. Rev. Lett. **76**, 2073 (1996).
23. E. Esarey *et al*., Phys. Rev. Lett. **79**, 2682 (1997).
24. G. Fubiani *et al*., Phys. Rev. E **70**, 016402 (2004).
25. H. Kotaki *et al*., Phys. Plasmas **11**, 3296 (2004).
26. J. Faure *et al*., C. R. Phys. **10**, 148 (2009).
27. S. Bulanov *et al*., Phys. Rev. E **58**, R5257 (1998).
28. H. Suk *et al*., Phys. Rev. Lett. **86**, 1011 (2001).
29. T. Y. Chien *et al*., Phys. Rev. Lett. **94**, 115003 (2005).
30. C. G. R. Geddes *et al*., Phys. Rev. Lett. **100**, 215004 (2008).
31. K. Schmid *et al*., Phys. Rev. Spec. Top., Accel. Beams **13**, 091301 (2010).
32. A. Pak *et al*., Phys. Rev. Lett. **104**, 025003 (2010).
33. E. Oz *et al*., Phys. Rev. Lett. **98**, 084801 (2007).
34. C. McGuffey *et al*., Phys. Rev. Lett. **104**, 025004 (2010).
35. D. H. Whittum, A. M. Sessler, and J. M. Dawson, Phys. Rev. Lett. **64**, 2511 (1990).
36. R. B. Palmer, J. Appl. Phys. **43**, 3014 (1972).
37. E. D. Courant, C. Pellegrini, and W. Zakowicz, Phys. Rev. A **32**, 2813 (1985).
38. P. Musumeci *et al*., Phys. Rev. Lett. **94**, 154801 (2005).
39. K. Németh *et al*., Phys. Rev. Lett. **100**, 095002 (2008).
40. M. J. H. Luttikhof *et al*., Phys. Rev. Lett. **105**, 124801 (2010).
41. I. Nam *et al*., Phys. Plasmas **18**, 043107 (2011).

42. S. Ya. Tochitsky, O. B. Williams, P. Musumeci, C. Sung, D. J. Haberberger, A. M. Cook, J. B. Rosenzweig, and C. Joshi, Phys. Rev. ST Accel. Beams **12**, 050703 (2009).

43. J. L. Shaw, N. Vafaei-Najafabadi, K. A. Marsh, and C. Joshi, AIP Conf. Proc. **1507**, 315 (2012).

44. J. L. Shaw, "Characterization of Sub-Millimeter-Scale Gas Cells as Possible Injectors for Staged Laser Wakefield Acceleration," M.S. thesis, University of California, Los Angeles, 2013.

45. S. P. D. Mangles *et al*., Phys. Rev. Lett. **96**, 215001 (2006).

46. R. A. Fonseca *et al*., in *Computational Science – ICCS 2002*, edited by P. M. A. Sloot *et al*., Lecture Notes in Computer Science, Vol. 2331 (Springer, Berlin, 2002), pp. 342–351.

47. M. V. Ammosov, N. B. Delone, and V. P. Krainov, Sov. Phys.-JETP **64**, 1191 (1986).

48. N. Lemos, J. L. Shaw, K. A. Marsh, and C. Joshi, AIP Conf. Proc. **1777**, 040009 (2016).

49. S. Kneip, S. R. Nagel, C. Bellei, N. Bourgeois, A. E. Dangor, A. Gopal, R. Heathcote, S. P. D. Mangles, J. R. Marquès, A. Maksimchuk, P. M. Nilson, K. T. Phuoc, S. Reed, M. Tzoufras, F. S. Tsung, L. Willingale, W. B. Mori, A. Rousse, K. Krushelnick, and Z. Najmudin, Phys. Rev. Lett. **100**, 105006 (2008).

50. S. Cipiccia *et al*., Nat. Phys. **7**, 867 (2011).

51. F. Albert, N. Lemos, J. L. Shaw, B. B. Pollock, C. Goyon, W. Schumaker, A. M. Saunders, K. A. Marsh, A. Pak, J. E. Ralph, J. L. Martins, L. D. Amorim, R. W. Falcone, S. H. Glenzer, J. D. Moody, and C. Joshi, Phys. Rev. Lett. **118**, 134801 (2017).

52. N. Lemos, J. L. Shaw, F. Albert, P. King, A. Milder, K. A. Marsh, A. Pak, and C. Joshi, "Hyper-Spectral Directional X-Ray Source," to be submitted to Physical Review Letters.

53. J. Vieira, J. Martins, and U. Sinha, "Plasma Based Helical Undulator for Controlled Emission of Circularly and Elliptically Polarised Betatron Radiation," to be submitted to Plasma Physics.

Publications and Conference Presentations

Publications

Y. Akbas, G. R. Savich, A. Jukna, T. Plecenik, P. Ďurina, A. Plecenik, G. W. Wicks, and R. Sobolewski, "Low-Temperature Performance of Semiconducting Asymmetric Nanochannel Diodes," J. Phys.: Conf. Ser. **906**, 012001 (2017).

P. Angland, D. Haberberger, S. T. Ivancic, and D. H. Froula, "Angular Filter Refractometry Analysis Using Simulated Annealing," Rev. Sci. Instrum. **88**, 103510 (2017).

A. Bose, R. Betti, D. Shvarts, and K. M. Woo, "The Physics of Long- and Intermediate-Wavelength Asymmetries of the Hot Spot: Compression Hydrodynamics and Energetics," Phys. Plasmas **24**, 102704 (2017).

L. Calderín, V. V. Karasiev, and S. B. Trickey, "Kubo–Greenwood Electrical Conductivity Formulation and Implementation for Projector Augmented Wave Datasets," Comp. Phys. Commun. **221**, 118 (2017).

G. Chen, R. Shrestha, A. Amori, Z. Staniszewski, A. Jukna, A. Korliov, C. Richter, M. El Fray, T. Krauss, and R. Sobolewski, "Terahertz Time-Domain Spectroscopy Characterization of Carbon Nanostructures Embedded in Polymer," J. Phys.: Conf. Ser. **906**, 012002 (2017).

C. Dorrer, A. Consentino, R. Cuffney, I. A. Begishev, E. M. Hill, and J. Bromage, "Spectrally Tunable, Temporally Shaped Parametric Front End to Seed High-Energy Nd:glass Laser Systems," Opt. Express **25**, 26,802 (2017).

F. Fereidouni, Z. T. Harmany, M. Tian, A. Todd, J. A. Kintner, J. D. McPherson, A. D. Borowsky, J. Bishop, M. Lechpammer, S. G. Demos, and R. Levenson, "Microscopy with Ultraviolet Surface Excitation for Rapid Slide-Free Histology," Nat. Biomed. Eng. **1**, 957 (2017).

R. K. Follett, D. H. Edgell, D. H. Froula, V. N. Goncharov, I. V. Igumenshchev, J. G. Shaw, and J. F. Myatt, "Full-Wave and Ray-Based Modeling of Cross-Beam Energy Transfer Between Laser Beams with Distributed Phase Plates and Polarization Smoothing," Phys. Plasmas **24**, 103128 (2017).

R. K. Follett, J. F. Myatt, J. G. Shaw, D. T. Michel, A. A. Solodov, D. H. Edgell, B. Yaakobi, and D. H. Froula, "Simulations and Measurements of Hot-Electron Generation Driven by the Multibeam Two-Plasmon–Decay Instability," Phys. Plasmas **24**, 102134 (2017).

T. A. Germer, K. A. Sharma, T. G. Brown, and J. B. Oliver, "Polarized Optical Scattering by Inhomogeneities and Surface Roughness in an Anisotropic Thin Film," J. Opt. Soc. Am. A **34**, 1974 (2017).

S. X. Hu, L. A. Collins, J. P. Colgan, V. N. Goncharov, and D. P. Kilcrease, "Optical Properties of Highly Compressed Polystyrene: An *Ab Initio* Study," Phys. Rev. B **96**, 144203 (2017).

V. V. Ivanov, K. J. Swanson, G. S. Sarkisov, A. V. Maximov, P. P. Wiewior, A. L. Astanovitskiy, V. Nalajala, O. Chalyy, O. Dmitriev, and N. L. Wong, "Observation of Impact of Eddy Current on Laser Targets in a Strong Fast Rising Magnetic Field," Phys. Plasmas **24**, 112707 (2017).

A. Jukna, J. Gradauskas, A. Sužiedelis, A. Maneikis, K. Šliužienė, and R. Sobolewski, "Investigation of the *I*–*V* Characteristics Asymmetry in Semiconducting Y–Ba–Cu–O Diodes," Micro Nano Lett. **12**, 838 (2017).

A. Kar and I. Franco, "Quantifying Fermionic Decoherence in Many-Body Systems," J. Chem. Phys. **146**, 214107 (2017).

A. Lazicki, R. A. London, F. Coppari, D. Erskine, H. D. Whitley, K. J. Caspersen, D. E. Fratanduono, M. A. Morales, P. M. Celliers, J. H. Eggert, M. Millot, D. C. Swift, G. W. Collins, S. O. Kucheyev, J. I. Castor, and J. Nilsen, "Shock Equation of State of ^{6}LiH to 1.1 TPa," Phys. Rev. B **96**, 134101 (2017).

E. Llor Aisa, X. Ribeyre, G. Duchateau, T. Nguyen-Bui, V. T. Tikhonchuk, A. Colaïtis, R. Betti, A. Bose, and W. Theobald, "The Role of Hot Electrons in the Dynamics of a Laser-Driven Strong Converging Shock," Phys. Plasmas **24**, 112711 (2017).

B. W. Plansinis, W. R. Donaldson, and G. P. Agrawal, "Single-Pulse Interference Caused by Temporal Reflection at Moving Refractive-Index Boundaries," J. Opt. Soc. Am. B **34**, 2274 (2017).

D. N. Polsin, D. E. Fratanduono, J. R. Rygg, A. Lazicki, R. F. Smith, J. H. Eggert, M. C. Gregor, B. H. Henderson, J. A. Delettrez, R. G. Kraus, P. M. Celliers, F. Coppari, D. C. Swift, C. A. McCoy, C. T. Seagle, J.-P. Davis, S. J. Burns, G. W. Collins, and T. R. Boehly, "Measurement of Body-Centered-Cubic Aluminum at 475 GPa," Phys. Rev. Lett. **119**, 175702 (2017).

D. B. Schaeffer, W. Fox, D. Haberberger, G. Fiksel, A. Bhattacharjee, D. H. Barnak, S. X. Hu, K. Germaschewski, and R. K. Follett, "High-Mach Number, Laser-Driven Magnetized Collisionless Shocks," Phys. Plasmas **24**, 122702 (2017).

J. Serafini, S. B. Trivedi, D. Kochanowska, M. Witkowska-Baran, A. Mycielski, M. Guziewicz, R. Kruszka, W. Słysz, and R. Sobolewski, "Characterization of (Cd,Mn)Te and (Cd,Mg)Te Single Crystals in the THz Frequency Range Using Integrated Photoconductive and Electro-Optics Effects," J. Phys.: Conf. Ser. **906**, 012016 (2017).

W. L. Shang, R. Betti, S. X. Hu, K. Woo, L. Hao, C. Ren, A. R. Christopherson, A. Bose, and W. Theobald, "Electron Shock Ignition of Inertial Fusion Targets," Phys. Rev. Lett. **119**, 195001 (2017).

W. Theobald, A. Bose, R. Yan, R. Betti, M. Lafon, D. Mangino, A. R. Christopherson, C. Stoeckl, W. Seka, W. Shang, D. T. Michel, C. Ren, R. C. Nora, A. Casner, J. Peebles, F. N. Beg, X. Ribeyre, E. Llor Aisa, A. Colaïtis, V. Tikhonchuk, and M. S. Wei, "Enhanced Hot-Electron Production and Strong-Shock Generation in Hydrogen-Rich Ablators for Shock Ignition," Phys. Plasmas **24**, 120702 (2017).

G. J. Williams, H. Chen, J. E. Field, O. L. Landen, and D. J. Strozzi, "Positron Radiography of Ignition-Relevant ICF Capsules," Phys. Plasmas **24**, 122704 (2017).

M. Zaghoo and I. F. Silvera, "Conductivity and Dissociation in Liquid Metallic Hydrogen and Implications for Planetary Interiors," Proc. Natl. Acad. Sci. USA **45**, 11,873 (2017).

A. B. Zylstra, J. A. Frenje, M. Gatu Johnson, G. M. Hale, C. R. Brune A. Bacher, D. T. Casey, C. K. Li, D. McNabb, M. Paris, R. D. Petrasso, T. C. Sangster, D. B. Sayre, and F. H. Séguin, "Proton Spectra from ^{3}He + T and ^{3}He + ^{3}He Fusion at Low Center-of-Mass Energy, with Potential Implications for Solar Fusion Cross Sections," Phys. Rev. Lett **119**, 222701 (2017).

Forthcoming Publications

B. P. Chock, D. R. Harding, and T. B. Jones, "Using Digital Microfluidics to Dispense, Combine, and Transport Low-Surface-Energy Fluids," to be published in Fusion Science and Technology.

K. Falk, M. Holec, C. J. Fontes, C. L. Fryer, C. W. Greeff, H. M. Johns, D. S. Montgomery, D. W. Schmidt, and M. Šmíd, "Measurement of Preheat Due to Nonlocal Electron Transport in Warm, Dense Matter," to be published in Physical Review Letters.

P. Fiala, Y. Li, and C. Dorrer, "Investigation of Focusing and Correcting Aberrations with Binary Amplitude and Polarization Modulation," to be published in Applied Optics.

J. A. Fooks, L. C. Carlson, P. Fitzsimmons, E. Giraldez, D. N. Kaczala, M. Wei, N. Alexander, M. P. Farrell, J. Betcher, A. Harvey-Thompson, and T. Nagayama, "Evolution of Magnetized Liner Inertial Fusion (MagLIF) Targets," to be published in Fusion Science and Technology.

D. H. Froula, D. Turnbull, T. J. Kessler, D. Haberberger, S.-W. Bahk, I. A. Begishev, R. Boni, S. Bucht, A. Davies, J. Katz, and J. L. Shaw, "Spatiotemporal Control of Laser Intensity," to be published in Nature Photonics.

M. Gatu Johnson, D. T. Casey, M. Hohenberger, A. B. Zylstra, A. Bacher, C. R. Brune, R. M. Bionta, R. S. Craxton, C. L. Ellison, M. Farrell, J. A. Frenje, W. Garbett, E. M. Garcia, G. P. Grim, E. Hartouni, R. Hatarik, H. W. Herrmann, M. Hohensee, D. M. Holunga, M. Hoppe, M. Jackson, N. Kabadi, S. F. Khan, J. D. Kilkenny, T. R. Kohut, B. Lahmann, H. P. Le, C. K. Li, L. Masse, P. W. McKenty, D. P. McNabb, A. Nikroo, T. G. Parham, C. E. Parker, R. D. Petrasso, J. Pino, B. Remington,

N. G. Rice, H. G. Rinderknecht, M. J. Rosenberg, J. Sanchez, D. B. Sayre, M. E. Schoff, C. M. Shuldberg, F. H. Séguin, H. Sio, Z. B. Walters, and H. D. Whitley, "Optimization of a High-Yield, Low-Areal-Density Fusion Product Source at the National Ignition Facility with Applications in Nucleosynthesis Experiments," to be published in Physical Review Letters.

D. R. Harding, J. Ulreich, M. D. Wittman, R. Chapman, C. Taylor, R. Taylor, N. P. Redden, J. C. Lambropoulos, R. Q. Gram, M. J. Bonino, and D. W. Turner, "Requirements and Capabilities for Fielding Cryogenic DT-Containing Fill-Tube Targets for Direct-Drive Experiments on OMEGA," to be published in Fusion Science and Technology.

S. X. Hu, "Electron–Electron Correlation in Two-Photon Double-Ionization of He-Like Ions," submitted to be published in Physical Review A.

K. R. P. Kafka, S. Papernov, and S. G. Demos, "Enhanced Laser Conditioning of Magnetorheologically Finished Silica Using Temporally Shaped Nanosecond Pulses," to be published in Optics Letters.

V. V. Karasiev, J. W. Dufty, and S. B. Trickey, "Nonempirical Semilocal Free-Energy Density Functional for Matter Under Extreme Conditions," to be published in Physical Review Letters.

R. K. Kirkwood, D. P. Turnbull, T. Chapman, S. C. Wilks, M. D. Rosen, R. A. London, L. A. Pickworth, W. H. Dunlop, J. D. Moody, D. J. Strozzi, P. A. Michel, L. Divol, O. L. Landen, B. J. MacGowan, B. M. Van Wonterghem, K. B. Fournier, and B. E. Blue, "Plasma-Based Beam Combiner for Very High Fluence and Energy," to be published in Nature Physics.

E. V. Ludeña, E. X. Salazar, M. H. Cornejo, D. E. Arroyo, and V. V. Karasiev, "The Liu–Parr Power Series Expansion of the Pauli Kinetic Energy Functional with the Incorporation of the Shell-Inducing Traits: Atoms," to be published in the International Journal of Quantum Chemistry.

J. A. Marozas, M. Hohenberger, M. J. Rosenberg, D. Turnbull, T. J. B. Collins, P. B. Radha, P. W. McKenty, J. D. Zuegel, F. J. Marshall, S. P. Regan, T. C. Sangster, W. Seka, E. M. Campbell, V. N. Goncharov, M. W. Bowers, J.-M. G. DiNicola, G. Erbert, B. J. MacGowan, L. J. Pelz, and S. T. Yang, "First Observation of Cross-Beam Energy Transfer Mitigation for Direct-Drive Inertial Confinement Fusion Implosions Using Wavelength Detuning at the National Ignition Facility," to be published in Physical Review Letters.

M. Millot, S. Hamel, J. R. Rygg, P. M. Celliers, G. W. Collins, F. Coppari, D. E. Fratanduono, R. Jeanloz, D. C. Swift, and J. H. Eggert, "Experimental Evidence for Superionic Water Ice Using Shock Compression," to be published in Nature Physics.

S. A. Muller, D. N. Kaczala, H. M. Abu-Shawareb, E. L. Alfonso, L. C. Carlson, M. Mauldin, P. Fitzsimmons, D. Lamb, P. Tzeferacos, L. Chen, G. Gregori, A. Rigby, A. Bott, T. G. White, D. Froula, and J. Katz, "Evolution of the Design and Fabrication of Astrophysics Targets for Turbulent Dynamo (TDYNO) Experiments on OMEGA," to be published in Fusion Science and Technology.

B. W. Plansinis, W. R. Donaldson, and G. P. Agrawal, "Cross-Phase-Modulation-Induced Temporal Reflection and Waveguiding of Optical Pulses," to be published in the Journal of the Optical Society of America B.

S. P. Regan, V. N. Goncharov, T. C. Sangster, E. M. Campbell, R. Betti, K. S. Anderson, T. Bernat, A. Bose, T. R. Boehly, M. J. Bonino, D. Cao, R. Chapman, T. J. B. Collins, R. S. Craxton, A. K. Davis, J. A. Delettrez, D. H. Edgell, R. Epstein, M. Farrell, C. J. Forrest, J. A. Frenje, D. H. Froula, M. Gatu Johnson, C. Gibson, V. Yu. Glebov, A. Greenwood, D. R. Harding, M. Hohenberger, S. X. Hu, H. Huang, J. Hund, I. V. Igumenshchev, D. W. Jacobs-Perkins, R. T. Janezic, M. Karasik, R. L. Keck, J. H. Kelly, T. J. Kessler, J. P. Knauer, T. Z. Kosc, S. J. Loucks, J. A. Marozas, F. J. Marshall, R. L. McCrory, P. W. McKenty, D. D. Meyerhofer, D. T. Michel, J. F. Myatt, S. P. Obenschain, R. D. Petrasso, N. Petta, P. B. Radha, M. J. Mosenberg, A. J. Schmitt, M. J. Schmitt, M. Schoff, W. Seka, W. T. Shmayda, M. J. Shoup III, A. Shvydky, A. A. Solodov, C. Stoeckl, W. Sweet, C. Taylor, R. Taylor, W. Theobald, J. Ulreich, M. D. Wittman, K. M. Woo, and J. D. Zuegel, "The National Direct-Drive Program: OMEGA to the National Ignition Facility," to be published in Fusion Science and Technology.

H. G. Rinderknecht, H.-S. Park, J. S. Ross, P. A. Amendt, D. P. Higginson, S. C. Wilks, D. Haberberger, J. Katz, D. H. Froula, N. M. Hoffman, G. Kagan, B. D. Keenan, and E. L. Vold, "Highly Resolved Measurements of a Developing Strong Collisional Plasma Shock," to be published in Physics of Plasmas.

M. J. Rosenberg, A. A. Solodov, J. F. Myatt, W. Seka, P. Michel, M. Hohenberger, R. W. Short, R. Epstein, S. P. Regan, E. M. Campbell, T. Chapman, C. S. Goyon, J. E. Ralph, M. A. Barrios, J. D. Moody, and J. W. Bates, "Origins and Scaling of Hot-Electron Preheat in Ignition-Scale Direct-Drive Inertial

Confinement Fusion Experiments," to be published in Physical Review Letters.

J. L. Shaw, N. Lemos, K. A. Marsh, D. H. Froula, and C. Joshi, "Experimental Signatures of Direct-Laser-Acceleration-Assisted Laser Wakefield Acceleration," to be published in Plasma Physics and Controlled Fusion.

D. Turnbull, S. Bucht, A. Davies, D. Haberberger, T. J. Kessler, J. L. Shaw, and D. H. Froula, "Raman Amplification with a Flying Focus," to be published in Physical Review Letters.

P. Tzeferacos, A. Rigby, A. Bott, A. R. Bell, R. Bingham, A. Casner, F. Cattaneo, E. M. Churazov, J. Emig, F. Fiuza, C. B. Forest, J. Foster, C. Graziani, J. Katz, M. Koenig, C.-K. Li, J. Meinecke, R. Petrasso, H.-S. Park, B. A. Remington, J. S. Ross, D. Ryu, D. Ryutov, T. G. White, B. Reville, F. Miniati, A. A. Schekochihin, D. Q. Lamb, D. H. Froula, and G. Gregori, "Laboratory Evidence of Dynamo Amplification of Magnetic Fields in a Turbulent Plasma," to be published in Nature Communications.

M. P. Valdivia, D. Stutman, C. Stoeckl, C. Mileham, I. A. Begishev, J. Bromage, and S. P. Regan, "Talbot–Lau X-Ray Deflectometry Phase-Retrieval Methods for Electron Density Diagnostics in High-Energy Density Experiments," to be published in Applied Optics.

M. D. Wittman, M. J. Bonino, D. H. Edgell, C. Fella, D. R. Harding, and J. Sanchez, "Effect of Tritium-Induced Damage on Plastic Targets from High-Density DT Permeation," to be published in Fusion Science and Technology.

H. Zhang, R. Betti, V. Gopalaswamy, R. Yan, and H. Aluie, "Nonlinear Excitation of the Ablative Rayleigh–Taylor Instability for All Wave Numbers," to be published in Physical Review E.

Conference Presentations

C. Z. R. Huang, R. W. Wood, and S. G. Demos, "Microscopy with Ultraviolet Surface Excitation for Enhancing K–12 and Undergraduate Education in Life Science," presented at the 2017 Biomedical Engineering Society Annual Meeting, Phoenix, AZ, 11–14 October 2017.

The following presentations were made at the 59th Annual Meeting of the APS Division of Plasma Physics, Milwaukee, WI, 23–27 October 2017:

K. S. Anderson, P. W. McKenty, A. Shvydky, T. J. B. Collins, C. J. Forrest, J. P. Knauer, P. B. Radha, F. J. Marshall, A. Sefkow, and M. M. Marinak, "Three-Dimensional Modeling of Low-Mode Asymmetries in OMEGA Cryogenic Implosions."

R. Betti, V. Gopalaswamy, J. P. Knauer, A. R. Christopherson, D. Patel, K. M. Woo, A. Bose, K. S. Anderson, T. J. B. Collins, S. X. Hu, D. T. Michel, C. J. Forrest, R. Shah, P. B. Radha, V. N. Goncharov, V. Yu. Glebov, A. V. Maximov, C. Stoeckl, F. J. Marshall, M. J. Bonino, D. R. Harding, R. T. Janezic, J. H. Kelly, S. Sampat, T. C. Sangster, S. P. Regan, E. M. Campbell, M. Gatu Johnson, J. A. Frenje, C. K. Li, and R. D. Petrasso, "The 1-D Cryogenic Implosion Campaign on OMEGA" (invited).

T. R. Boehly, C. A. McCoy, D. E. Fratanduono, P. Celliers, M. C. Gregor, D. N. Polsin, Y. Ding, S. X. Hu, J. R. Rygg, and G. W. Collins, "Measurements of Sound Velocity and Grüneisen Parameter in CH Shocked to 800 GPa."

A. Bose, R. Betti, and K. M. Woo, D. Shvarts, D. S. Clark, S. W. Haan, A. L. Kritcher, O. L. Landen, J. Lindl, J. H. Nuckolls, and M. D. Rosen, "The Physics of Low- and Mid-Mode Asymmetries of the Hot Spot."

D. Cao, T. R. Boehly, P. B. Radha, D. N. Polsin, A. K. Davis, S. P. Regan, and V. N. Goncharov, "Dependence of Shock Timing on Coronal Parameters for OMEGA Direct-Drive Implosions."

A. R. Christopherson, and R. Betti, "Definition of Ignition in Inertial Confinement Fusion."

T. J. B. Collins, J. A. Marozas, D. Cao, J. A. Delettrez, P. W. McKenty, P. B. Radha, S. Skupsky, and G. Moses, "Advances in Modeling Direct-Drive Ignition-Scale Designs for the National Ignition Facility."

L. Crandall, J. R. Rygg, G. W. Collins, T. R. Boehly, A. Jenei, D. E. Fratanduono, M. C. Gregor, M. Millot, J. H. Eggert, and D. Spaulding, “Equation-of-State Measurements of Precompressed CO_2.”

R. S. Craxton, E. M. Garcia, L. T. Browning, S. Le Pape, H.-S. Park, C. K. Li, and A. B. Zylstra, “Saturn Designs for Small Proton-Backlighter Targets at the National Ignition Facility.”

J. R. Davies, D. H. Barnak, R. Betti, V. Yu. Glebov, J. P. Knauer, J. L. Peebles, K. J. Peterson, and D. B. Sinars, “Fuel Areal-Density Measurements in Laser-Driven MagLIF from Secondary Neutrons.”

A. K. Davis, D. T. Michel, A. B. Sefkow, Y. H. Ding, R. Epstein, S. X. Hu, J. P. Knauer, and D. H. Froula, “Conduction-Zone Measurements Using X-Ray Self-Emission Images.”

J. A. Delettrez, R. K. Follett, C. Stoeckl, W. Seka, and J. P. Matte, “Understanding Hard X-Ray Emission in Direct-Drive Implosions.”

Y. H. Ding, and S. X. Hu, “Density-Functional-Theory–Based Equation-of-State Table of Beryllium for Inertial Confinement Fusion Applications.”

D. H. Edgell, R. K. Follett, J. Katz, J. F. Myatt, J. G. Shaw, D. Turnbull, and D. H. Froula, “Polarization Rotation from Cross-Beam Energy Transfer During Direct-Drive OMEGA Implosions.”

R. Epstein, C. Stoeckl, V. N. Goncharov, P. W. McKenty, S. P. Regan, and P. B. Radha, “Simulation and Analysis of Time-Gated Monochromatic Radiographs of Cryogenic Implosions on OMEGA.”

R. K. Follett, D. H. Edgell, D. H. Froula, V. N. Goncharov, I. V. Igumenshchev, J. G. Shaw, J F Myatt, J. W. Bates, K. Obenschain, and J. Weaver, “Wave-Based Cross-Beam Energy Transfer Simulations with Laser Speckle and Polarization Smoothing.”

C. J. Forrest, K. S. Anderson, V. Yu. Glebov, V. N. Goncharov, J. P. Knauer, O. M. Mannion, P. B. Radha, S. P. Regan, T. C. Sangster, and C. Stoeckl, “Low-Mode Variations of the Cold-Fuel Distribution in Cryogenic DT Implosions on OMEGA.”

D. H. Froula, D. Turnbull, A. Davies, T. J. Kessler, D. Haberberger, S.-W. Bahk, I. A. Begishev, R. Boni, S. Bucht, J. Katz, J. Palastro, and J. L. Shaw, “Flying Focus: Spatiotemporal Control of Longitudinal Intensity.”

V. Yu. Glebov, C. J. Forrest, J. P. Knauer, O. M. Mannion, S. P. Regan, T. C. Sangster, C. Stoeckl, and M. Gatu Johnson, “Upgraded Neutron Time-of-Flight Detectors for DT Implosions on OMEGA.”

V. N Goncharov, “A Model for the Growth of Localized Shell Features in Inertial Confinement Fusion Implosions.”

X. Gong, D. N. Polsin, J. R. Rygg, T. R. Boehly, L. Crandall, B. J. Henderson, S. X. Hu, M. Huff, R. Saha, G. W. Collins, R. Smith, J. H. Eggert, A. E. Lazicki, and M. McMahon, “Sodium X-Ray Diffraction in the High-Pressure Regime.”

V. Gopalaswamy, R. Betti, J. P. Knauer, A. R. Christopherson, D. Patel, K. M. Woo, W. Shang, A. Bose, K. S. Anderson, T. J. B. Collins, V. N. Goncharov, P. B. Radha, V. Yu. Glebov, A. V. Maximov, C. Stoeckl, F. J. Marshall, E. M. Campbell, and S. P. Regan, “A Statistical Approach to Implosion Design on the OMEGA Laser.”

D. Haberberger, A. Davies, S. Bucht, J. Katz, J. L. Shaw, D. Turnbull, I. A. Begishev, S.-W. Bahk, J. Bromage, J. D. Zuegel, D. H. Froula, J. D. Sadler, P. A. Norreys, R. Trines, and R. Bingham, “Picosecond Thermal Dynamics in an Underdense Plasma Measured with Thomson Scattering.”

A. Hansen, D. Haberberger, J. L. Shaw, and D. H. Froula, “OMEGA Supersonic Gas-Jet Target System Characterization.”

R. J. Henchen, V. N. Goncharov, D. Cao, J. Katz, D. H. Froula, W. Rozmus, and M. Sherlock, “Heat-Flux Measurements in Laser-Produced Plasmas Using Thomson Scattering from Electron Plasma Waves.”

B. Henderson, T. R. Boehly, S. X. Hu, D. N. Polsin, J. R. Rygg, G. W. Collins, M. C. Gregor, D. E. Fratanduono, R. Kraus, J. H. Eggert, and P. M. Celliers, “Hugoniot Measurements of Silicon Shock Compressed to 21 Mbar.”

S. X. Hu, T. R. Boehly, Y. H. Ding, P. B. Radha, V. N. Goncharov, J. R. Rygg, G. W. Collins, S. P. Regan, E. M. Campbell, L. A. Collins, and J. D. Kress, “High-Energy-

Density–Physics Studies for Inertial Confinement Fusion Applications" (invited).

I. V. Igumenshchev, E. M. Campbell, V. N. Goncharov, S. P. Regan, A. Shvydky, and A. J. Schmitt, "Three-Dimensional Hydrodynamic Simulations of the Effects of Laser Imprint in OMEGA Implosions."

S. T. Ivancic, C. R. Stillman, P. M. Nilson, C. Mileham, A. A. Solodov, and D. H. Froula, "Blast-Wave Generation and Propagation in Rapidly Heated Laser-Irradiated Targets."

A. Kar, T. R. Boehly, P. B. Radha, D. Cao, D. H. Edgell, S. X. Hu, A. Shvydky, V. N. Goncharov, and S. P. Regan, "X-Ray Radiography of Laser-Driven Shocks for Inertial Confinement Fusion."

V. V. Karasiev, S. X. Hu, S. Trickey, and J. Dufty, "Development of Fast and Reliable Free-Energy Density Functional Methods for Simulations of Dense Plasmas from Cold- to Hot-Temperature Regimes."

J. P. Knauer, R. Betti, V. Gopalaswamy, M. J. Bonino, E. M. Campbell, T. J. B. Collins, C. J. Forrest, V. Yu. Glebov, V. N. Goncharov, D. R. Harding, O. M. Mannion, J. A. Marozas, F. J. Marshall, P. W. McKenty, D. T. Michel, P. B. Radha, S. P. Regan, T. C. Sangster, C. Stoeckl, M. Gatu Johnson, and J. A. Frenje, "Experimental Results from the High-Adiabat Cryogenic Implosion Campaign on OMEGA."

O. M. Mannion, K S. Anderson, C. J. Forrest, V. Yu. Glebov, C. Stoeckl, V. N. Goncharov, J. P. Knauer, P. B. Radha, S. P. Regan, T. C. Sangster, and M. Gatu Johnson, "Indications of Bulk Fluid Motion in Direct-Drive Implosions."

J. A. Marozas, M. Hohenberger, M. J. Rosenberg, D. Turnbull, T. J. B. Collins, P. B. Radha, P. W. McKenty, J. D. Zuegel, F. J. Marshall, S. P. Regan, T. C. Sangster, W. Seka, E. M. Campbell, V. N. Goncharov, M. W. Bowers, J.-M. G. DiNicola, G. Erbert, B. J. MacGowan, L. J. Pelz, J. D. Moody, and S. T. Yang, "Wavelength Detuning Cross-Beam Energy Transfer Mitigation Scheme for Direct-Drive: Modeling and Evidence from National Ignition Facility Implosions" (invited).

A. V. Maximov, J. G. Shaw, R. K. Follett, R. W. Short, J. Palastro, and J. F. Myatt, "Modeling of Stimulated Raman Scattering in Direct-Drive Inertial Confinement Fusion Plasmas for National Ignition Facility Conditions."

P. W. McKenty, T. J. B. Collins, J. A. Marozas, R. S. Craxton, E. M. Garcia, D. Cao, D. Keller, A. Shvydky, K. Molvig, and M. J. Schmitt, "Evaluation of the *Revolver* Ignition Design at the National Ignition Facility Using Polar-Direct-Drive Illumination."

D. T. Michel, I. V. Igumenshchev, A. K. Davis, D. H. Edgell, D. H. Froula, D. W. Jacobs-Perkins, V. N. Goncharov, S. P. Regan, R. Shah, A. Shvydky, and E. M. Campbell, "Subpercent Scale Control of 3-D Modes 1, 2, and 3 of Targets Imploded in the Direct-Drive Configuration on OMEGA."

A. L. Milder, and D. H. Froula, "Measuring Non-Maxwellian Distribution Functions Using Expanded Thomson Scattering."

S. C. Miller, J. P. Knauer, C. J. Forrest, P. B. Radha, V. N. Goncharov, O. M. Mannion, T. J. B. Collins, J. A. Marozas, and K. S. Anderson, "Finite Atwood Number Effects on Deceleration-Phase Instability in Room-Temperature Direct-Drive Implosions."

Z. L. Mohamed, O. M. Mannion, C. J. Forrest, J. P. Knauer, K. S. Anderson, and P. B. Radha, "Effects of Hot-Spot Geometry on Backscattering and Down-Scattering Neutron Spectra."

D. Patel, R. Betti, K. M. Woo, D. T. Michel, R. C. Shah, F. J. Marshall, V. Gopalaswamy, A. Bose, D. Cao, J. P. Knauer, C. Stoeckl, and S. P. Regan, "Signatures of an Intermediate-Mode Asymmetry in OMEGA Implosions."

J. L. Peebles, J. R. Davies, D. H. Barnak, R. Betti, V. Yu. Glebov, J. P. Knauer, K. J. Peterson, and D. B. Sinars, "Enhancing Neutron Yield in Cylindrical Implosions with an Applied Magnetic Field."

D. N. Polsin, D. E. Fratanduono, J. R. Rygg, A. Lazicki, R. F. Smith, J. H. Eggert, M. C. Gregor, B. J. Henderson, X. Gong, J. A. Delettrez, R. G. Kraus, P. M. Celliers, F. Coppari, D. C. Swift, C. A. McCoy, C. T. Seagle, J.-P. Davis, S. J. Burns, G. W. Collins, T. R. Boehly, "X-Ray Diffraction of Ramp-Compressed Aluminum to 547 GPa" (invited).

P. B. Radha, R. Betti, E. M. Campbell, D. Cao, T. J. B. Collins, C. J. Forrest, V. Yu. Glebov, V. N. Goncharov, S. X. Hu, J. P. Knauer, J. A. Marozas, F. J. Marshall, S. P. Regan, T. C. Sangster, A. Shvydky, C. Stoeckl, M. Gatu Johnson, J. A. Frenje, and R. D. Petrasso, "The Effect of Laser Imprint on OMEGA Cryogenic Implosions."

S. P. Regan, D. Cao, V. N. Goncharov, K. S. Anderson, R. Betti, M. J. Bonino, E. M. Campbell, T. J. B. Collins, R. Epstein, C. J. Forrest, V. Yu. Glebov, D. R. Harding, S. X. Hu, I. V. Igumenshchev, J. A. Marozas, F. J. Marshall, P. W. McKenty, D. T. Michel, P. B. Radha, T. C. Sangster, C. Stoeckl, M. Gatu Johnson, J. A. Frenje, R. D. Petrasso, R. W. Luo, A. Tambazidis, M. E. Schoff, and M. Farrell, "Direct-Drive DT Cryogenic Implosion Performance with a Fill Tube."

J. J. Ruby, J. R. Rygg, G. W. Collins, B. Bachmann, T. Doeppner, Y. Ping, J. Gaffney, A. Lazicki, A. L. Kritcher, D. Swift, J. Nilsen, O. L. Landen, R. Hatarik, N. Masters, S. R. Nagel, P. A. Sterne, T. Pardini, S. Khan, P. M. Celliers, P. K. Patel, D. O. Gericke, and R. W. Falcone, "Analytic Analysis of Convergent Shocks to Multi-Gigabar Conditions."

J. L. Shaw, D. H. Froula, N. Lemos, W. B. Mori, C. Joshi, L. D. Amorim, and N. Vafaei-Najafabadi, "Direct Laser Acceleration in Wakefield Accelerators Driven with Circularly Polarized Lasers."

R. W. Short, A. V. Maximov, and W. Seka, "Absolute Stimulated Raman Sidescattering in Direct-Drive Irradiation Geometries."

A. Shvydky, P. B. Radha, M. J. Rosenberg, K. S. Anderson, V. N. Goncharov, J. A. Marozas, F. J. Marshall, P. W. McKenty, S. P. Regan, T. C. Sangster, M. Hohenberger, J. M. Di Nicola, J. M. Koning, M. M. Marinak, L. Masse, and M. Karasik, "Three-Dimensional Simulations of Flat-Foil Laser-Imprint Experiments at the National Ignition Facility."

A. A. Solodov, M. J. Rosenberg, J. F. Myatt, W. Seka, R. Epstein, R. W. Short, S. P. Regan, D. H. Froula, P. B. Radha, V. N. Goncharov, J. W. Bates, A. J. Schmitt, P. Michel, M. Hohenberger, T. Chapman, and J. D. Moody, "Laser–Plasma Interaction Experiments at Direct-Drive Ignition-Relevant Plasma Conditions at the National Ignition Facility."

C. R. Stillman, P. M. Nilson, S. T. Ivancic, C. Mileham, D. H. Froula, and I. E. Golokin, "Picosecond Time-Resolved Temperature and Density Measurements with K-Shell Spectroscopy."

C. Stoeckl, R. Epstein, R. Betti, C. J. Forrest, V. Yu. Glebov, V. N. Goncharov, V. Gopalaswamy, D. R. Harding, I. V. Igumenshchev, D. W. Jacobs-Perkins, R. Janezic, J. H. Kelly, D. T. Michel, F. J. Marshall, S. F. B. Morse, S. P. Regan, P. B. Radha, T. C. Sangster, M. J. Shoup III, W. T. Shmayda, C. Sorce, W. Theobald, J. Ulreich, J. Zhang, M. Gatu Johnson, J. A. Frenje, R. D. Petrasso, M. Farrell, A. Greenwood, M. Schoff, and W. Sweet, "Comparison of the Performance of Polystyrene and Glow-Discharge Polymer Ablators Used in Cryogenic Implosions."

W. Theobald, C. Sorce, R. Epstein, R. L. Keck, C. Kellogg, T. J. Kessler, J. Kwiatkowski, F. J. Marshall, S. P. Regan, W. Seka, R. Shah, A. Shvydky, C. Stoeckl, and L. J. Waxer, "Inferred UV Fluence Focal-Spot Profiles from Soft X-Ray Pinhole-Camera Measurements on OMEGA."

K. M. Woo, R. Betti, A. Bose, D. Patel, and V. Gopalaswamy, "Three-Dimensional Studies of the Effect of Residual Kinetic Energy on Yield Degradation."

M. Zaghoo, and I. F. Silvera, "Dynamic Conductivity and Partial Ionization in Metallic Hydrogen."

H. Zhang, R. Betti, V. Gopalaswamy, R. Yan, and H. Aluie, "Nonlinear Excitation of the Linearly Stable Ablative Rayleigh–Taylor Instability for All Wave Numbers."

R. Betti, V. Gopalaswamy, J. P. Knauer, A. Bose, K. S. Anderson, T. J. B. Collins, S. X. Hu, D. T. Michel, C. J. Forrest, R. Shah, P. B. Radha, V. N. Goncharov, V. Yu. Glebov, A. V. Maximov, C. Stoeckl, F. J. Marshall, M. J. Bonino, D. R. Harding, R. T. Janezic, J. H. Kelly, S. Sampat, T. C. Sangster, S. P. Regan, E. M. Campbell, M. Gatu Johnson, J. A. Frenje, C. K. Li, and R. Petrasso, "Tripling the Fusion Yield of OMEGA Direct-Drive Implosions Through Data-Driven Statistical Modeling," presented at the Cornell Engineering Seminar, Ithaca, NY, 30 November 2017.

The following presentations were made at the Materials Research Society Fall Meeting, Boston, MA, 26 November–1 December 2017:

D. R. Harding, B. P. Chock, and T. B. Jones, "Digital Microfluidic Methods for Forming Droplets of Low-Surface-Energy Fluids, Combining Them into Emulsions, and Transforming Them into Polymer Shells."

N. D. Viza, and D. R. Harding, "Microfluidic Devices for Producing Millimeter-Size Droplets, Emulsions, and Polystyrene Shells for Inertial Fusion Confinement Experiments."

Y. Zhao, and W. R. Donaldson, “Systematic Study on the Photo-reseponse in $Al_xGa_{1-x}N$ UV Photodetectors.”

The following presentations were made at the 38th Annual Meeting and Symposium Fusion Power Associates, Pathways and Progress Toward Fusion Power, Washington, DC, 6–7 December 2017:

R. Betti, V. Gopalaswamy, J. P. Knauer, A. R. Christopherson, D. Patel, K. M. Woo, A. Bose, K. S. Anderson, T. J. B. Collins, S. X. Hu, D. T. Michel, C. J. Forrest, R. Shah, P. B. Radha, V. N. Goncharov, V. Yu. Glebov, A. V. Maximov, C. Stoeckl, F. J. Marshall, M. J. Bonino, D. R. Harding, R. T. Janezic, J. H. Kelly, S. Sampat, T. C. Sangster, S. P. Regan, E. M. Campbell, M. Gatu Johnson, J. A. Frenje, C. K. Li, and R. Petrasso, “Achieving Record Fusion Yields in Direct-Drive Laser-Fusion Experiments Using Statistical Mapping.”

G. W. Collins, “High-Energy-Density Microphysics: Progress and Plans.”

V. N. Goncharov, “Progress Toward Demonstration of Ignition Hydroequivalence on OMEGA.”

R. Betti, V. Gopalaswamy, J. Knauer, A. Bose, K. S. Anderson, T. J. B. Collins, S. X. Hu, D. T. Michel, C. J. Forrest, R. Shah, P. B. Radha, V. N. Goncharov, V. Yu. Glebov, A. V. Maximov, C. Stoeckl, F. J. Marshall, M. J. Bonino, D. R. Harding, R. T. Janezic, J. H. Kelly, S. Sampat, T. C. Sangster, S. P. Regan, E. M. Campbell, M. Gatu Johnson, J. A. Frenje, C. K. Li, and R. Petrasso, “Tripling the Fusion Yield of OMEGA Direct-Drive Implosions Through Data-Driven Statistical Modeling,” presented at the Physics Colloquium at the Shanghai Institute of Laser Plasma, Shanghai, China, 7 December 2017.

UNIVERSITY *of* ROCHESTER